Supporting Information for

A computational study to assess the pathogenicity of missense variants on respiratory Complex I

Laura Rigobello, Francesca Lugli,* Leonardo Caporali, Alessio Bartocci, Jacopo Fadanni, Francesco Zerbetto, Luisa Iommarini, Valerio Carelli, Anna Maria Ghelli, Francesco Musiani*

* Francesca Lugli and Francesco Musiani
Email: francesca.lugli6@unibo.it and francesco.musiani@unibo.it.

This PDF file includes:

Table S1. List of human and ovine CI subunits.

Homo sapiens		*Ovis aries*	
Subunit	**Abbreviation**	**Subunit**	**Abbreviation**
NADH dehydrogenase [ubiquinone] flavoprotein 1, mitochondrial	NDUFV1	NADH dehydrogenase [ubiquinone] flavoprotein 1, mitochondrial	51 kDa
NADH dehydrogenase [ubiquinone] flavoprotein 2, mitochondrial	NDUFV2	Mitochondrial complex I, 24 kDa subunit	24 kDa
NADH-ubiquinone oxidoreductase 75 kDa subunit	NDUFS1	NADH:ubiquinone oxidoreductase core subunit S1	75 kDa
NADH dehydrogenase [ubiquinone] iron-sulfur protein 2, mitochondrial	NDUFS2	Mitochondrial complex I, 49 kDa subunit	49 kDa
NADH dehydrogenase [ubiquinone] iron-sulfur protein 3, mitochondrial	NDUFS3	NADH:ubiquinone oxidoreductase core subunit S3	30 kDa
NADH dehydrogenase [ubiquinone] iron-sulfur protein 7, mitochondrial	NDUFS7	Mitochondrial complex I, PSST subunit	PSST
NADH dehydrogenase [ubiquinone] iron-sulfur protein 8, mitochondrial	NDUFS8	Mitochondrial complex I, TYKY subunit	TYKY
NADH dehydrogenase [ubiquinone] flavoprotein 3, mitochondrial	NDUFV3	Mitochondrial complex I, 10 kDa subunit	10 kDa
NADH dehydrogenase [ubiquinone] iron-sulfur protein 6, mitochondrial	NDUFS6	Mitochondrial complex I, 13 kDa subunit	13 kDa
NADH dehydrogenase [ubiquinone] iron-sulfur protein 4, mitochondrial	NDUFS4	NADH dehydrogenase [ubiquinone] iron-sulfur protein 4, mitochondrial	NDUFS4
NADH dehydrogenase [ubiquinone] 1 alpha subcomplex subunit 9, mitochondrial	NDUFA9	NADH:ubiquinone oxidoreductase subunit A9	NDUFA9
NADH dehydrogenase [ubiquinone] 1 alpha subcomplex subunit 2	NDUFA2	NADH dehydrogenase [ubiquinone] 1 alpha subcomplex subunit 2	NDUFA2
NADH dehydrogenase [ubiquinone] 1 alpha subcomplex subunit 5	NDUFA5	Mitochondrial complex I, B13 subunit	NDUFA5
NADH dehydrogenase [ubiquinone] 1 alpha subcomplex subunit 6	NDUFA6	NADH:ubiquinone oxidoreductase subunit A6	NDUFA6
NADH dehydrogenase [ubiquinone] 1 alpha subcomplex subunit 7	NDUFA7	Mitochondrial complex I, B14.5a subunit	NDUFA7
NADH dehydrogenase [ubiquinone] 1 alpha subcomplex subunit 12	NDUFA12	NADH dehydrogenase [ubiquinone] 1 alpha subcomplex subunit 12	NDUFA12
NADH-ubiquinone oxidoreductase chain 3	ND3	NADH-ubiquinone oxidoreductase chain 3	ND3
NADH-ubiquinone oxidoreductase chain 1	ND1	NADH-ubiquinone oxidoreductase chain 1	ND1
NADH-ubiquinone oxidoreductase chain 6	ND6	NADH-ubiquinone oxidoreductase chain 6	ND6
NADH-ubiquinone oxidoreductase chain 4L	ND4L	NADH-ubiquinone oxidoreductase chain 4L	ND4L
NADH-ubiquinone oxidoreductase chain 5	ND5	NADH-ubiquinone oxidoreductase chain 5	ND5
NADH-ubiquinone oxidoreductase chain 4	ND4	NADH-ubiquinone oxidoreductase chain 4	ND4
NADH-ubiquinone oxidoreductase chain 2	ND2	NADH-ubiquinone oxidoreductase chain 2	ND2
NADH dehydrogenase [ubiquinone] 1 alpha subcomplex subunit 11	NDUFA11	Mitochondrial complex I, B14.7 subunit	NDUFA11
NADH dehydrogenase [ubiquinone] 1 beta subcomplex subunit 5, mitochondrial	NDUFB5	NADH:ubiquinone oxidoreductase subunit B5	NDUFB5
Acyl carrier protein, mitochondrial	NDUFAB1	Acyl carrier protein	NDUFAB1
NADH dehydrogenase [ubiquinone] 1 alpha subcomplex subunit 8	NDUFA8	NADH dehydrogenase [ubiquinone] 1 alpha subcomplex subunit 8	NDUFA8
NADH dehydrogenase [ubiquinone] 1 beta subcomplex subunit 10	NDUFB10	Mitochondrial complex I, PDSW subunit	PDSW
NADH dehydrogenase [ubiquinone] 1 alpha subcomplex subunit 10, mitochondrial	NDUFA10	NADH dehydrogenase [ubiquinone] 1 alpha subcomplex subunit 10, mitochondrial	NDUFA10
NADH dehydrogenase [ubiquinone] iron-sulfur protein 5	NDUFS5	NADH:ubiquinone oxidoreductase subunit S5	NDUFS5

NADH dehydrogenase [ubiquinone] 1 alpha subcomplex subunit 3	NDUFA3	NADH:ubiquinone oxidoreductase subunit A3	NDUFA3
NADH dehydrogenase [ubiquinone] 1 beta subcomplex subunit 3	NDUFB3	NADH:ubiquinone oxidoreductase subunit B3	NDUFB3
NADH dehydrogenase [ubiquinone] 1 subunit C2	NDUFC2	NADH dehydrogenase [ubiquinone] 1 subunit C2	NDUFC2
NADH dehydrogenase [ubiquinone] 1 beta subcomplex subunit 4	NDUFB4	NADH:ubiquinone oxidoreductase subunit B4	NDUFB4
NADH dehydrogenase [ubiquinone] 1 alpha subcomplex subunit 13	NDUFA13	Mitochondrial complex I, B16.6 subunit	NDUFA13
NADH dehydrogenase [ubiquinone] 1 beta subcomplex subunit 6	NDUFB6	Mitochondrial complex I, B17 subunit	NDUFB6
NADH dehydrogenase [ubiquinone] 1 beta subcomplex subunit 7	NDUFB7	NADH:ubiquinone oxidoreductase subunit B7	NDUFB7
NADH dehydrogenase [ubiquinone] 1 beta subcomplex subunit 9	NDUFB9	NADH:ubiquinone oxidoreductase subunit B9	NDUFB9
NADH dehydrogenase [ubiquinone] 1 beta subcomplex subunit 2, mitochondrial	NDUFB2	NADH:ubiquinone oxidoreductase subunit B2	NDUFB2
NADH dehydrogenase [ubiquinone] 1 beta subcomplex subunit 8, mitochondrial	NDUFB8	NADH dehydrogenase [ubiquinone] 1 beta subcomplex subunit 8, mitochondrial	NDUFB8
NADH dehydrogenase [ubiquinone] 1 beta subcomplex subunit 11, mitochondrial	NDUFB11	Mitochondrial complex I, ESSS subunit	ESSS
NADH dehydrogenase [ubiquinone] 1 subunit C1, mitochondrial	NDUFC1	Mitochondrial complex I, KFYI subunit	KFYI
NADH dehydrogenase [ubiquinone] 1 beta subcomplex subunit 1	NDUFB1	Mitochondrial complex I, MNLL subunit	MNLL
NADH dehydrogenase [ubiquinone] 1 alpha subcomplex subunit 1	NDUFA1	Mitochondrial complex I, MWFE subunit	MWFE

Table S2. Modelled residues in the ovine P+ module structures.

Ovine P+ module subunit	Open	Closed
49 kDa	41 - 430	41 - 424
ND3	31 - 48	-
ND1	205 - 210	-
ND6	78 - 86	-
NDUFB5	1 - 2	1 - 2
NDUFAB1	1	1
PDSW	1 - 2 174 - 175	1 - 2 174 - 175
NDUFA3	1 - 2	1 - 2
NDUFB3	1 - 10 90 - 97	1 - 10 90 - 97
NDUFA13	1 - 4	1 - 17
B17 subunit	38 - 64	38 - 64
NDUFB7	123 - 136	123 - 136
NDUFB9	178	178
NDUFB2	1 - 4 70 - 72	1 - 4 70 - 72
NDUFB8	1 - 2	1 - 2
ESSS	1 - 22 124 - 125	1 - 22 124 - 125
MNLL	1 - 6	1 - 6

Table S3. UniProt entries of the human aminoacidic sequences in the modelled systems and sequence identity with respect to the corresponding ovine CI subunit.

Human subunit	UniProt entry	Sequence identity (%)
NADH dehydrogenase [ubiquinone] iron-sulfur protein 2 (or 49 kDa subunit)	O75306	95.35
NADH-ubiquinone oxidoreductase chain 3 (or ND3)	P03897	73.04
NADH-ubiquinone oxidoreductase chain 1 (or ND1)	P03886	77.99
NADH-ubiquinone oxidoreductase chain 6 (or ND6)	P03923	60.92
NADH-ubiquinone oxidoreductase chain 4L (or ND4L)	P03901	76.53
NADH-ubiquinone oxidoreductase chain 5 (or ND5)	P03915	71.60
NADH-ubiquinone oxidoreductase chain 4 (or ND4)	P03905	75.66
NADH-ubiquinone oxidoreductase chain 2 (or ND2)	P03891	63.85
NADH dehydrogenase [ubiquinone] 1 α subcomplex subunit 11	Q86Y39	70.80
NADH dehydrogenase [ubiquinone] 1 β subcomplex subunit 5, mitochondrial	O43674	82.52
Acyl carrier protein, mitochondrial	O14561	97.73
NADH dehydrogenase [ubiquinone] 1 α subcomplex subunit 8	P51970	87.65
NADH dehydrogenase [ubiquinone] 1 β subcomplex subunit 10	O96000	78.86
NADH dehydrogenase [ubiquinone] 1 α subcomplex subunit 10, mitochondrial	O95299	79.69
NADH dehydrogenase [ubiquinone] iron-sulfur protein 5	O43920	70.48
NADH dehydrogenase [ubiquinone] 1 α subcomplex subunit 3	O95167	83.13
NADH dehydrogenase [ubiquinone] 1 β subcomplex subunit 3	O43676	83.51
NADH dehydrogenase [ubiquinone] 1 subunit C2	O95298	75.63
NADH dehydrogenase [ubiquinone] 1 β subcomplex subunit 4	O95168	75.00
NADH dehydrogenase [ubiquinone] 1 α subcomplex subunit 13	Q9P0J0	83.22
NADH dehydrogenase [ubiquinone] 1 β subcomplex subunit 6	O95139	77.95
NADH dehydrogenase [ubiquinone] 1 β subcomplex subunit 7	P17568	85.29
NADH dehydrogenase [ubiquinone] 1 β subcomplex subunit 9	Q9Y6M9	89.33
NADH dehydrogenase [ubiquinone] 1 β subcomplex subunit 2, mitochondrial	O95178	90.28
NADH dehydrogenase [ubiquinone] 1 β subcomplex subunit 8, mitochondrial	O95169	86.08
NADH dehydrogenase [ubiquinone] 1 β subcomplex subunit 11, mitochondrial	Q9NX14	86.29
NADH dehydrogenase [ubiquinone] 1 subunit C1, mitochondrial	O43677	79.59
NADH dehydrogenase [ubiquinone] 1 β subcomplex subunit 1	O75438	77.19
NADH dehydrogenase [ubiquinone] 1 α subcomplex subunit 1	O15239	80.00

Table S4. Results of the ProCheck [1] and Prosa [2, 3] analysis done on the model structures of human and ovine P+ module generated in this work together with the main template structures (in parentheses).

System	Subunit	Procheck Ramachandran plot (%)				Procheck G-factor	Prosa Z-score
		Most favored	Additionally allowed	Generously allowed	Disallowed		
wtO^{cl} (6ZKB)	all	94.5 (90.2)	5.4 (9.7)	0.1 (0.0)	0.0 (0.0)	0.09 (0.19)	-
	ND3	93.3 (94.2)	5.8 (5.8)	1.0 (0.0)	1.9 (0.0)	0.05 (0.12)	-1.68 (-1,63)
	ND1	94.0 (89.4)	6.0 (10.3)	0.0 (0.4)	0.0 (0.0)	0.04 (0.07)	-6.05 (-6.04)
	ND6	93.1 (88.2)	6.9 (11.8)	0.0 (0.0)	0.0 (0.0)	0.06 (0.07)	0.38 (0.34)
	ND4L	95.6 (90.1)	4.4 (9.9)	0.0 (0.0)	0.0 (0.0)	0.15 (0.16)	-2.80 (-2.87)
	ND5	93.1 (88.5)	6.7 (11.3)	0.2 (0.0)	0.0 (0.2)	0.09 (0.16)	-6.13 (-5.97)
	ND4	97.1 (93.8)	2.9 (6.2)	0.0 (0.0)	0.0 (0.0)	0.13 (0.17)	-7.76 (-7.79)
	ND2	96.1 (91.3)	3.9 (8.7)	0.0 (0.0)	0.0 (0.0)	0.13 (0.22)	-7.50 (-7.48)
wtO^{op} (6ZKA)	all	94.2 (91.7)	5.6 (8.2)	0.2 (0.0)	0.0 (0.0)	0.01 (0.21)	-
	ND3	96.2 (92.0)	3.8 (6.8)	0.0 (1.1)	0.0 (0.0)	0.08 (0.20)	-2.38 (-2.17)
	ND1	95.4 (92.0)	4.3 (8.0)	0.4 (0.0)	0.0 (0.0)	0.06 (0.18)	-6.33 (-5.61)
	ND6	93.1 (91.1)	6.9 (8.9)	0.0 (0.0)	0.0 (0.0)	0.08 (0.17)	0.41 (0.12)
	ND4L	93.4 (93.4)	6.6 (6.6)	0.0 (0.0)	0.0 (0.0)	0.18 (0.21)	-3.08 (-3.11)
	ND5	94.4 (89.6)	5.5 (10.2)	0.2 (0.0)	0.0 (0.2)	0.10 (0.18)	-6.33 (-6.21)
	ND4	97.6 (95.0)	2.4 (5.0)	0.0 (0.0)	0.0 (0.0)	0.12 (0.18)	-7.87 (-7.82)
	ND2	95.5 (93.6)	4.5 (6.4)	0.0 (0.0)	0.0 (0.0)	0.16 (0.24)	-7.45 (-7.47)
wtH^{cl}	all	94.4	5.5	0.2	0.0	0.03	-
	ND3	96.1	3.9	0.0	0.0	-0.03	-1.82
	ND1	96.1	3.9	0.0	0.0	-0.01	-5.69
	ND6	92.8	7.2	0.0	0.0	-0.01	0.39
	ND4L	94.4	5.6	0.0	0.0	0.10	-2.78
	ND5	93.7	5.9	0.4	0.0	0.01	-5.55
	ND4	97.1	2.9	0.0	0.0	0.08	-6.64
	ND2	96.4	3.6	0.0	0.0	0.02	-6.93
m1H^{cl}	all	94.4	5.5	0.2	0.0	0.03	-
	ND3	96.1	3.9	0.0	0.0	-0.03	-1.82
	ND1	96.1	3.9	0.0	0.0	-0.01	-5.69
	ND6	92.8	7.2	0.0	0.0	-0.01	0.51
	ND4L	94.4	5.6	0.0	0.0	0.10	-2.78
	ND5	93.7	5.9	0.4	0.0	0.01	-5.55
	ND4	97.1	2.9	0.0	0.0	0.08	-6.64
	ND2	96.4	3.6	0.0	0.0	0.02	-6.93

$m3H^{cl}$	all	94.4	5.5	0.2	0.0	0.03	-
	ND3	96.1	3.9	0.0	0.0	-0.03	-1.82
	ND1	96.1	3.9	0.0	0.0	-0.01	-5.69
	ND6	92.8	7.2	0.0	0.0	-0.01	0.51
	ND4L	94.4	5.6	0.0	0.0	0.10	-2.75
	ND5	93.7	5.9	0.4	0.0	0.01	-5.67
	ND4	97.1	2.9	0.0	0.0	0.08	-6.64
	ND2	96.4	3.6	0.0	0.0	0.02	-6.93
wtH^{op}	all	94.7	5.1	0.2	0.0	0.06	-
	ND3	93.1	5.9	1.0	0.0	0.00	-2.51
	ND1	95.0	5.0	0.0	0.0	-0.01	-5.91
	ND6	92.8	7.2	0.0	0.0	-0.02	0.32
	ND4L	96.7	3.3	0.0	0.0	0.15	-3.04
	ND5	93.0	6.8	0.2	0.0	0.01	-5.47
	ND4	97.4	2.6	0.0	0.0	0.04	-6.87
	ND2	96.8	3.2	0.0	0.0	0.05	-6.90
$m1H^{op}$	all	94.7	5.1	0.2	0.0	0.06	-
	ND3	93.1	5.9	1.0	0.0	0.00	-2.51
	ND1	95.0	5.0	0.0	0.0	-0.01	-5.91
	ND6	92.8	7.2	0.0	0.0	-0.02	0.32
	ND4L	96.7	3.3	0.0	0.0	0.15	-3.04
	ND5	93.0	6.8	0.2	0.0	0.01	-5.58
	ND4	97.4	2.6	0.0	0.0	0.04	-6.87
	ND2	96.8	3.2	0.0	0.0	0.05	-6.9
$m3H^{op}$	all	94.7	5.1	0.2	0.0	0.06	-
	ND3	93.1	5.9	1.0	0.0	0.00	-2.51
	ND1	95.0	5.0	0.0	0.0	-0.01	-5.91
	ND6	92.8	7.2	0.0	0.0	-0.02	0.32
	ND4L	96.7	3.3	0.0	0.0	0.15	-3.04
	ND5	93.0	6.8	0.2	0.0	0.01	-5.58
	ND4	97.4	2.6	0.0	0.0	0.04	-6.87
	ND2	96.8	3.2	0.0	0.0	0.05	-6.90

Fig. S1. Modelled regions in the ovine P+ modules.
Ribbon diagram of the structures of the ovine P+ module in the open (top panel) and closed (bottom panel) conformation with the addition of the modelled regions corresponding to the disordered regions not solved in the structures. The experimentally solved regions are in white, while the modelled ones are in red.

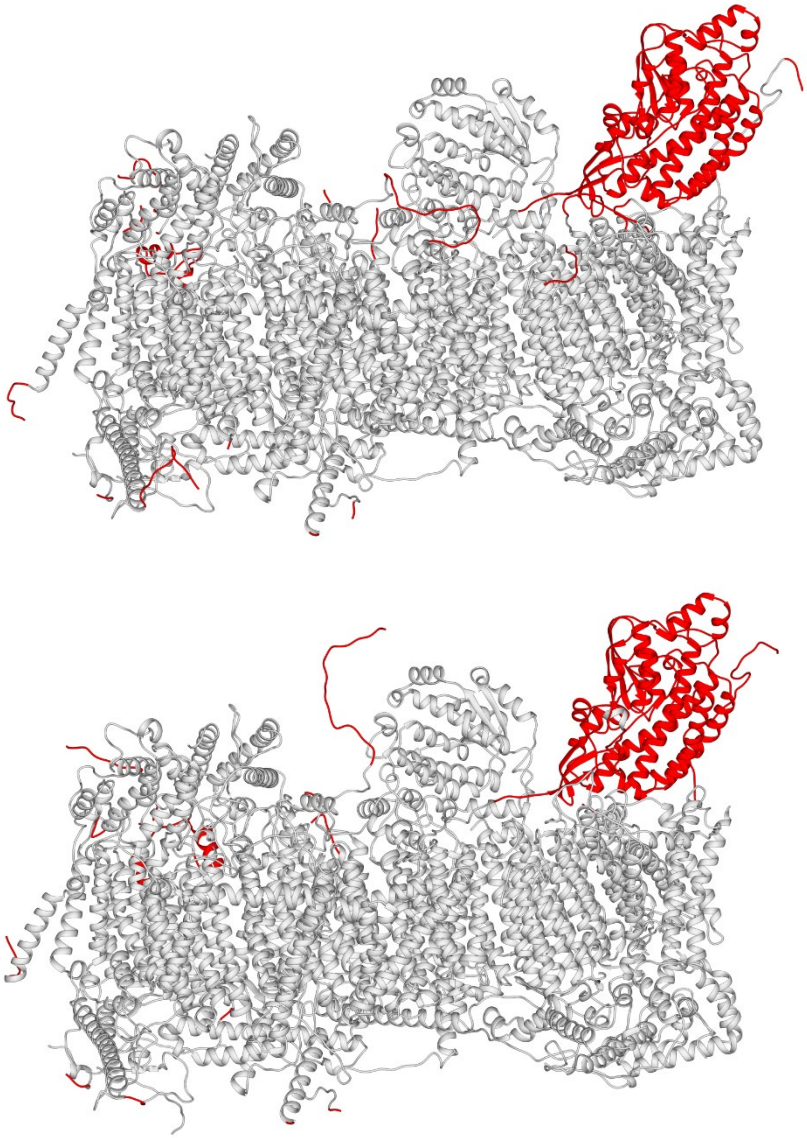

Fig. S2. Backbone beads RMSD *vs.* simulation time plots of the P+ module subunits in the wtO^{op} structures.
Each panel label corresponds to the equivalent subunit in Table S1. The RMSD values corresponding to the three replicas are in brown, orange, and light brown, respectively.

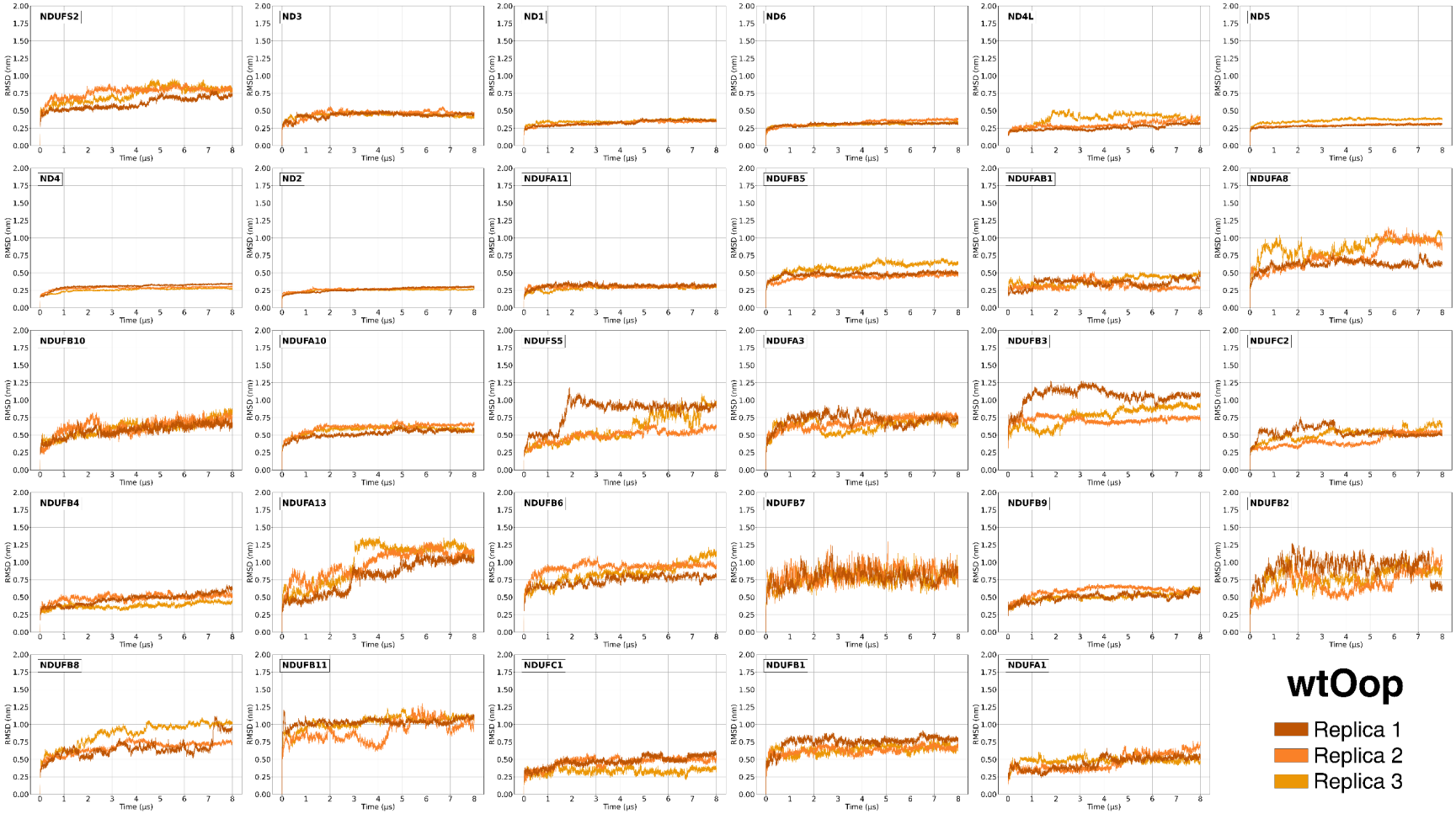

Fig. S3. Backbone beads RMSD *vs.* simulation time plots of the P+ module subunits in the wtO^{cl} structures.
Each panel label corresponds to the equivalent subunit in Table S1. The RMSD values corresponding to the three replicas are in brown, orange, and light brown, respectively.

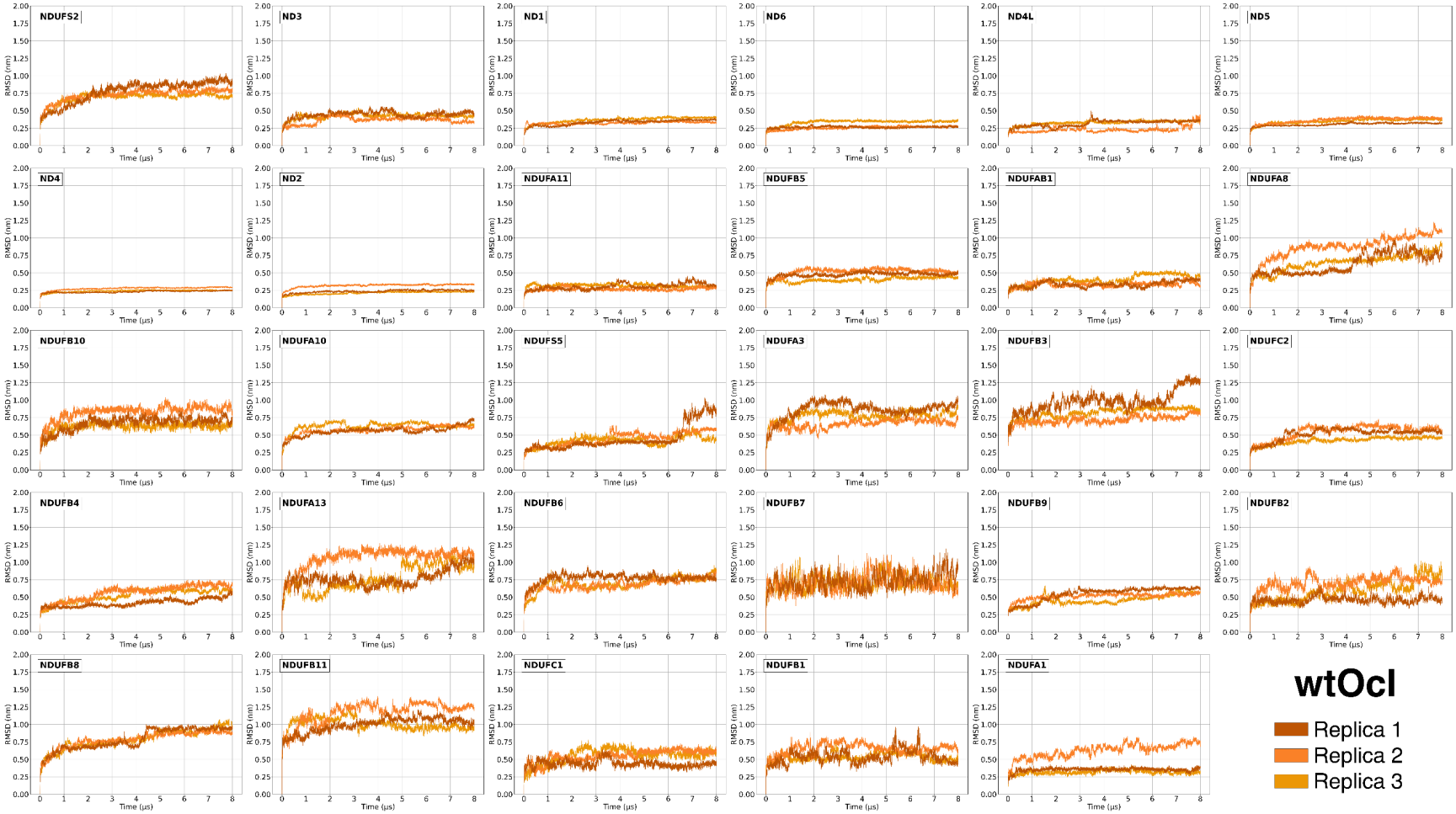

Fig. S4. Backbone beads RMSD *vs.* simulation time plots of the P+ module subunits in the wtH^{op} structures.
Each panel label corresponds to the equivalent subunit in Table S1. The RMSD values corresponding to the three replicas are in brown, maroon, and crimson, respectively.

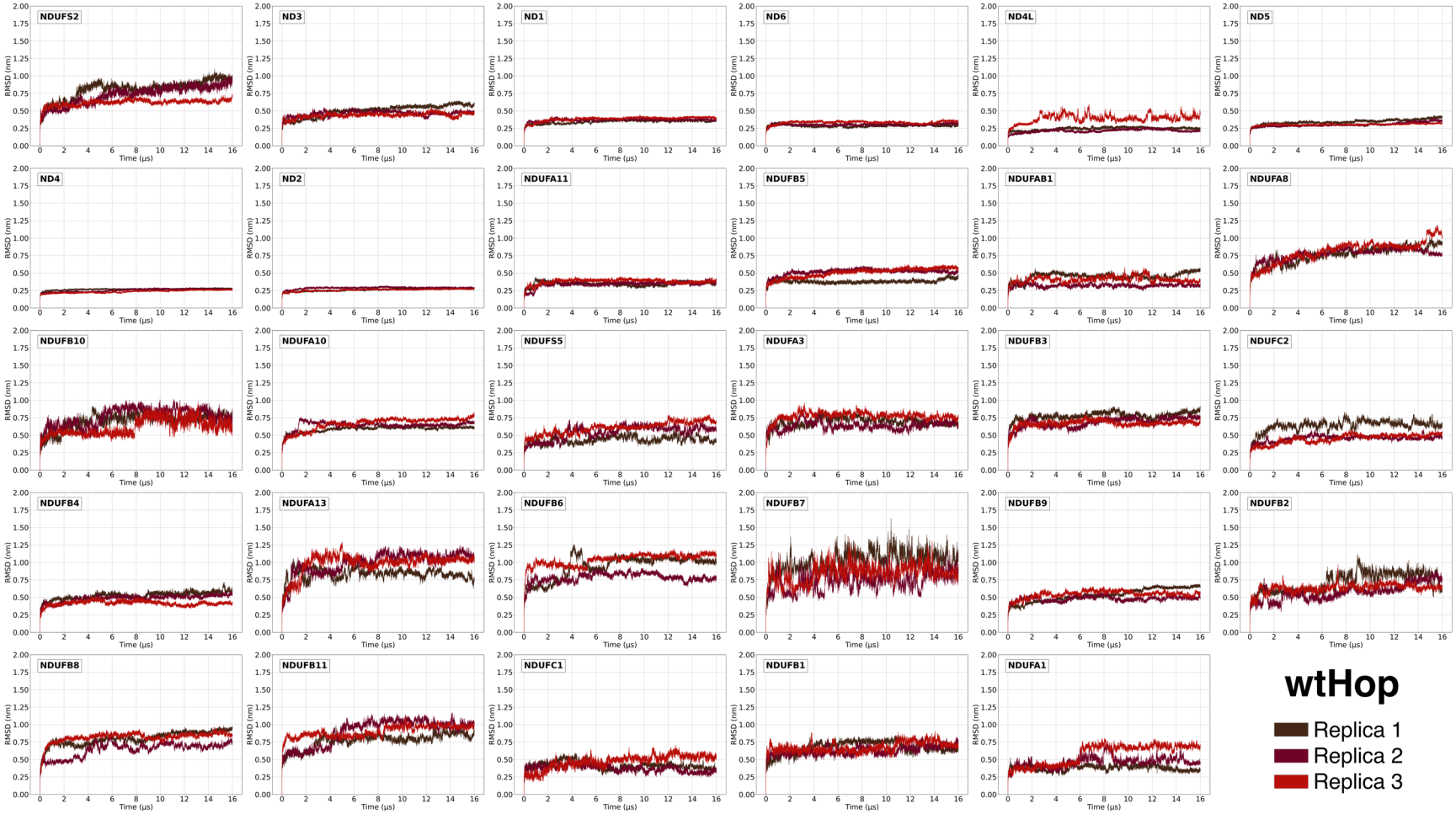

Fig. S5. Backbone beads RMSD *vs.* simulation time plots of the P+ module subunits in the wtH^{cl} structures.
Each panel label corresponds to the equivalent subunit in Table S1. The RMSD values corresponding to the three replicas are in brown, maroon, and crimson, respectively.

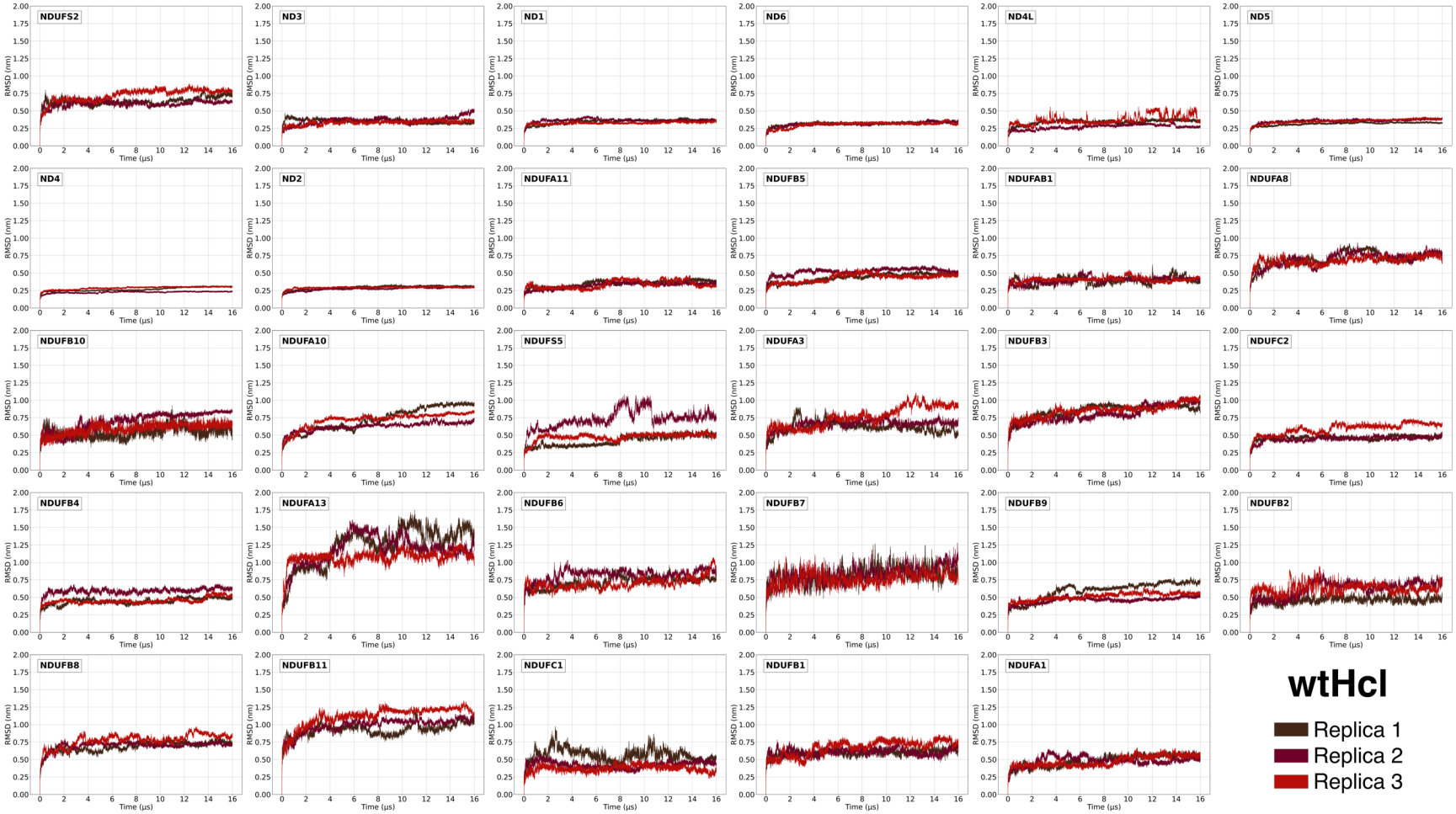

Fig. S6. Backbone beads RMSD *vs.* simulation time plots of the P+ module subunits in the m1H^{op} structures.
Each panel label corresponds to the equivalent subunit in Table S1. The RMSD values corresponding to the three replicas are in navy, royal blue, and fountain blue, respectively.

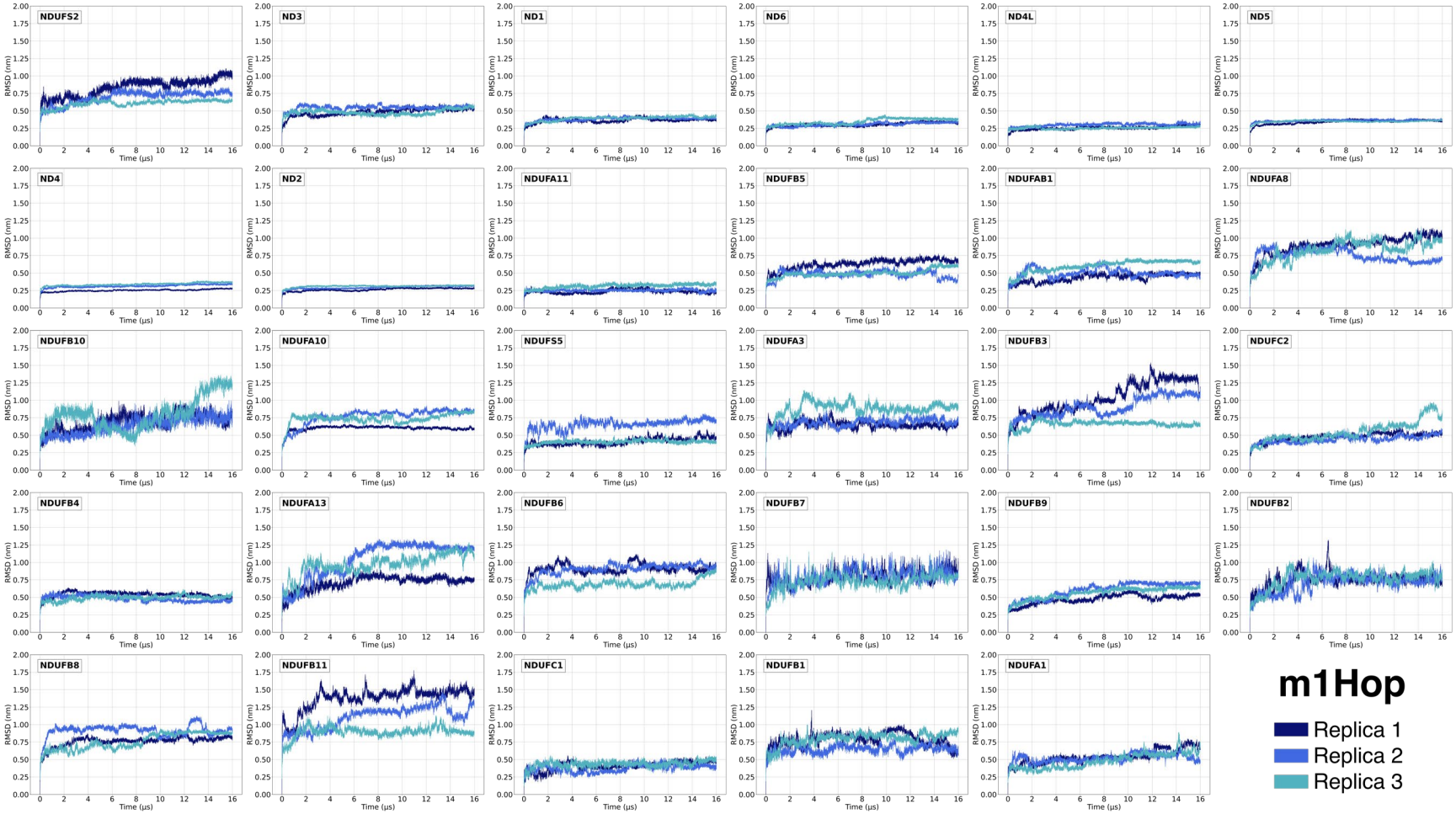

Fig. S7. Backbone beads RMSD *vs.* simulation time plots of the P+ module subunits in the m1H^{cl} structures.
Each panel label corresponds to the equivalent subunit in Table S1. The RMSD values corresponding to the three replicas are in navy, royal blue, and fountain blue, respectively.

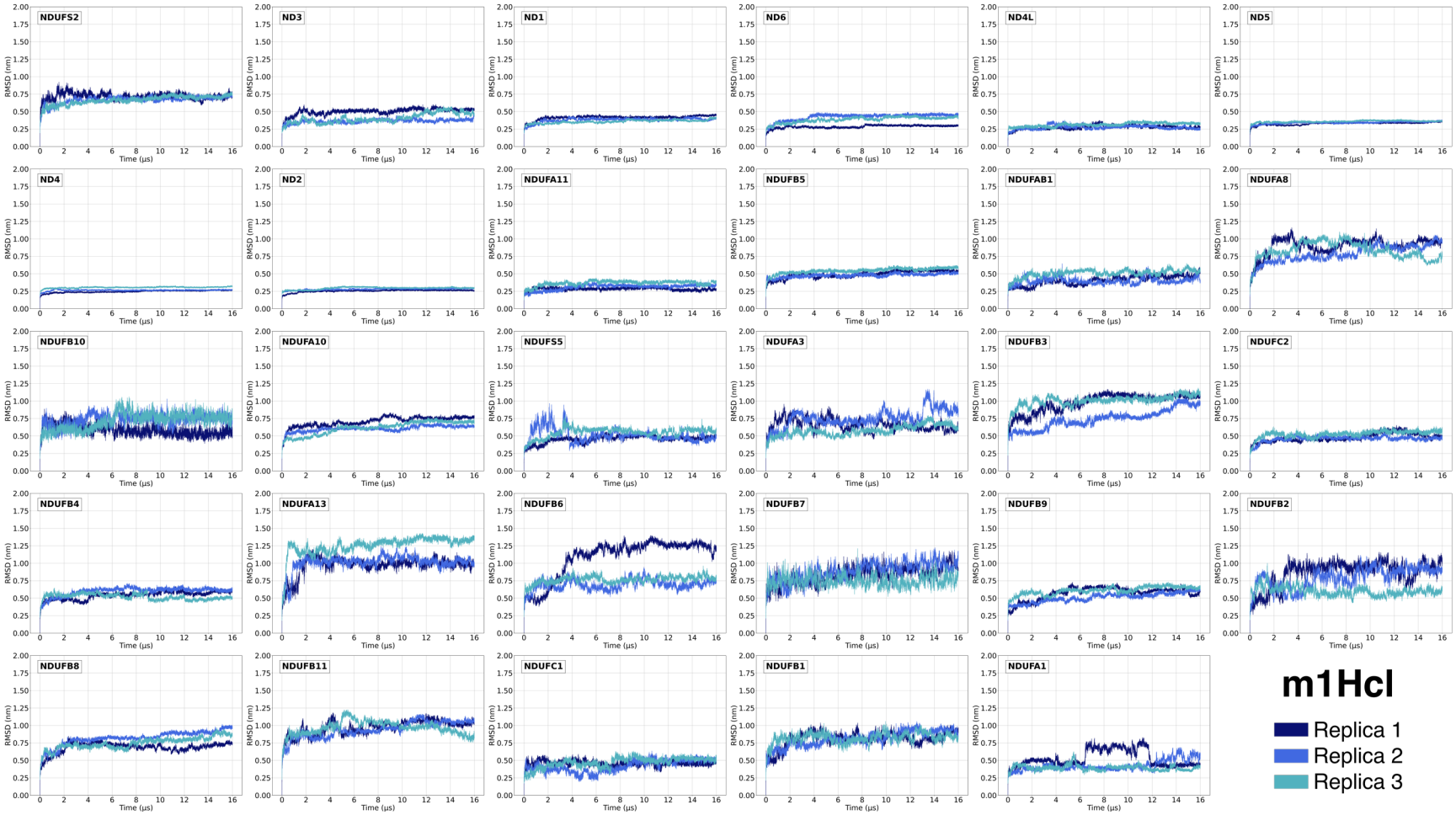

Fig. S8. Backbone beads RMSD *vs.* simulation time plots of the P+ module subunits in the m3H^{op} structures.
Each panel label corresponds to the equivalent subunit in Table S1. The RMSD values corresponding to the three replicas are in pine, dark lime, and lime, respectively.

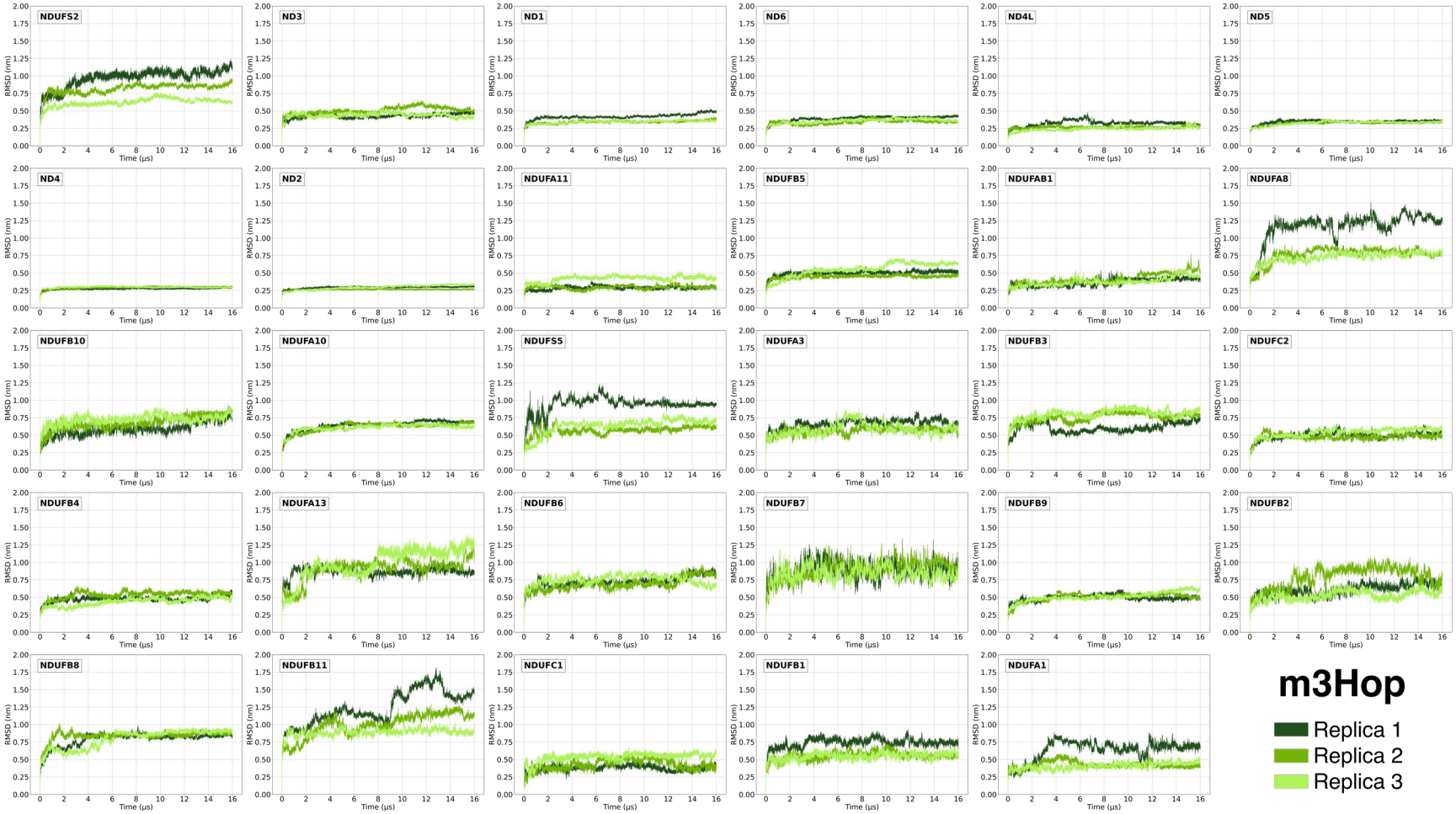

Fig. S9. Backbone beads RMSD *vs.* simulation time plots of the P+ module subunits in the m3H^{cl} structures.
Each panel label corresponds to the equivalent subunit in Table S1. The RMSD values corresponding to the three replicas are in dark pine, dark lime, and lime, respectively.

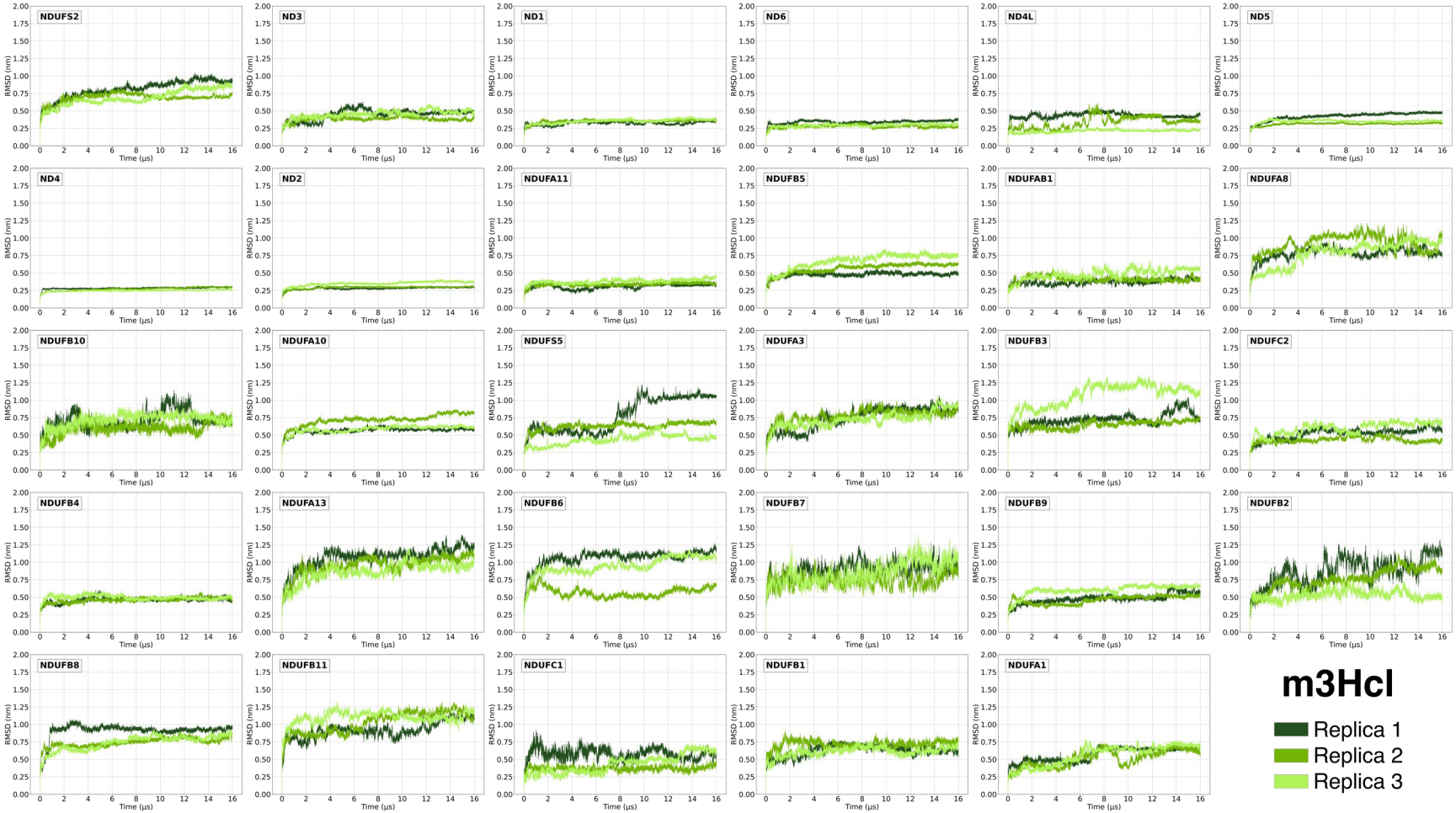

Table S5. Average and standard deviation of RMSD values (in nm) of backbone beads for each subunit of ovine and human P+ module. For each subunit, the ovine and human abbreviation (see Table S1) is reported. Each subunits line corresponds to a different replica.

Ovine/Human subunit	wtO^{op}	wtO^{cl}	wtH^{op}	wtH^{cl}	m1H^{op}	m1H^{cl}	m3H^{op}	m3H^{cl}
49 kDa / NDUFS2	0.7 ± 0.1	0.70 ± 0.08	0.8 ± 0.1	0.63 ± 0.06	0.8 ± 0.1	0.71 ± 0.05	1.0 ± 0.1	0.8 ± 0.1
	0.77 ± 0.08	0.71 ± 0.08	0.7 ± 0.1	0.60 ± 0.04	0.69 ± 0.09	0.67 ± 0.06	0.82 ± 0.08	0.69 ± 0.06
	0.62 ± 0.08	0.8 ± 0.2	0.63 ± 0.04	0.75 ± 0.09	0.61 ± 0.05	0.66 ± 0.06	0.63 ± 0.06	0.7 ± 0.1
ND3	0.44 ± 0.03	0.42 ± 0.04	0.50 ± 0.08	0.35 ± 0.03	0.48 ± 0.05	0.50 ± 0.04	0.43 ± 0.03	0.45 ± 0.08
	0.45 ± 0.04	0.42 ± 0.06	0.45 ± 0.03	0.37 ± 0.05	0.54 ± 0.03	0.36 ± 0.03	0.47 ± 0.05	0.35 ± 0.02
	0.43 ± 0.04	0.47 ± 0.05	0.44 ± 0.03	0.32 ± 0.03	0.48 ± 0.04	0.40 ± 0.07	0.44 ± 0.03	0.47 ± 0.06
ND1	0.35 ± 0.02	0.37 ± 0.04	0.34 ± 0.02	0.34 ± 0.03	0.36 ± 0.03	0.41 ± 0.03	0.42 ± 0.04	0.32 ± 0.03
	0.33 ± 0.03	0.33 ± 0.02	0.38 ± 0.02	0.38 ± 0.02	0.38 ± 0.03	0.38 ± 0.03	0.36 ± 0.02	0.37 ± 0.03
	0.34 ± 0.03	0.37 ± 0.03	0.40 ± 0.03	0.38 ± 0.02	0.39 ± 0.03	0.36 ± 0.02	0.36 ± 0.02	0.37 ± 0.02
ND6	0.30 ± 0.02	0.33 ± 0.04	0.29 ± 0.02	0.32 ± 0.02	0.30 ± 0.03	0.28 ± 0.02	0.39 ± 0.03	0.34 ± 0.02
	0.32 ± 0.03	0.28 ± 0.02	0.29 ± 0.02	0.32 ± 0.03	0.31 ± 0.03	0.42 ± 0.05	0.34 ± 0.02	0.29 ± 0.02
	0.32 ± 0.02	0.28 ± 0.01	0.32 ± 0.02	0.35 ± 0.03	0.34 ± 0.04	0.38 ± 0.04	0.36 ± 0.03	0.32 ± 0.03
ND4L	0.39 ± 0.07	0.33 ± 0.03	0.24 ± 0.02	0.34 ± 0.03	0.25 ± 0.03	0.27 ± 0.03	0.32 ± 0.04	0.43 ± 0.04
	0.32 ± 0.04	0.23 ± 0.04	0.24 ± 0.02	0.29 ± 0.03	0.30 ± 0.02	0.27 ± 0.03	0.25 ± 0.02	0.37 ± 0.07
	0.26 ± 0.03	0.33 ± 0.04	0.40 ± 0.06	0.37 ± 0.06	0.25 ± 0.01	0.31 ± 0.03	0.26 ± 0.02	0.25 ± 0.02
ND5	0.36 ± 0.03	0.35 ± 0.04	0.34 ± 0.03	0.31 ± 0.02	0.34 ± 0.03	0.33 ± 0.02	0.34 ± 0.02	0.42 ± 0.06
	0.31 ± 0.01	0.40 ± 0.04	0.31 ± 0.03	0.37 ± 0.02	0.36 ± 0.01	0.34 ± 0.02	0.34 ± 0.02	0.33 ± 0.02
	0.31 ± 0.02	0.36 ± 0.02	0.32 ± 0.01	0.37 ± 0.03	0.35 ± 0.01	0.36 ± 0.01	0.35 ± 0.02	0.37 ± 0.02
ND4	0.26 ± 0.03	0.24 ± 0.02	0.27 ± 0.01	0.27 ± 0.03	0.25 ± 0.02	0.24 ± 0.02	0.27 ± 0.01	0.28 ± 0.01
	0.30 ± 0.01	0.27 ± 0.02	0.26 ± 0.02	0.24 ± 0.01	0.31 ± 0.02	0.26 ± 0.01	0.31 ± 0.02	0.28 ± 0.02
	0.33 ± 0.03	0.26 ± 0.01	0.25 ± 0.01	0.29 ± 0.02	0.34 ± 0.02	0.30 ± 0.01	0.31 ± 0.01	0.29 ± 0.01
ND2	0.25 ± 0.02	0.21 ± 0.02	0.26 ± 0.02	0.29 ± 0.02	0.26 ± 0.02	0.25 ± 0.02	0.29 ± 0.01	0.28 ± 0.02
	0.30 ± 0.02	0.32 ± 0.02	0.31 ± 0.01	0.30 ± 0.02	0.29 ± 0.02	0.28 ± 0.01	0.30 ± 0.01	0.31 ± 0.01
	0.29 ± 0.03	0.28 ± 0.01	0.30 ± 0.01	0.31 ± 0.01	0.31 ± 0.01	0.29 ± 0.02	0.29 ± 0.03	0.38 ± 0.03
NDUFA11	0.28 ± 0.03	0.32 ± 0.02	0.34 ± 0.03	0.35 ± 0.04	0.24 ± 0.03	0.28 ± 0.02	0.29 ± 0.02	0.31 ± 0.03
	0.28 ± 0.02	0.27 ± 0.02	0.33 ± 0.04	0.33 ± 0.04	0.25 ± 0.02	0.31 ± 0.04	0.31 ± 0.03	0.35 ± 0.03
	0.29 ± 0.02	0.33 ± 0.03	0.40 ± 0.04	0.32 ± 0.06	0.31 ± 0.03	0.36 ± 0.03	0.40 ± 0.04	0.35 ± 0.03
NDUFB5	0.58 ± 0.07	0.40 ± 0.03	0.38 ± 0.03	0.43 ± 0.06	0.63 ± 0.07	0.49 ± 0.05	0.50 ± 0.03	0.48 ± 0.03
	0.44 ± 0.03	0.48 ± 0.04	0.52 ± 0.04	0.55 ± 0.04	0.48 ± 0.05	0.48 ± 0.03	0.44 ± 0.03	0.58 ± 0.07
	0.47 ± 0.03	0.46 ± 0.03	0.56 ± 0.07	0.49 ± 0.06	0.50 ± 0.05	0.54 ± 0.04	0.56 ± 0.09	0.6 ± 0.1
NDUFAB1	0.38 ± 0.06	0.40 ± 0.07	0.45 ± 0.05	0.38 ± 0.05	0.43 ± 0.06	0.40 ± 0.07	0.37 ± 0.05	0.37 ± 0.04
	0.33 ± 0.06	0.35 ± 0.03	0.34 ± 0.02	0.43 ± 0.04	0.49 ± 0.07	0.40 ± 0.05	0.46 ± 0.06	0.40 ± 0.04
	0.34 ± 0.05	0.34 ± 0.04	0.40 ± 0.03	0.42 ± 0.04	0.60 ± 0.08	0.51 ± 0.05	0.36 ± 0.04	0.51 ± 0.07

NDUFA8	0.9 ± 0.1	0.6 ± 0.1	0.8 ± 0.1	0.70 ± 0.09	0.9 ± 0.1	0.9 ± 0.1	1.2 ± 0.2	0.78 ± 0.09
	0.7 ± 0.2	0.9 ± 0.2	0.80 ± 0.08	0.71 ± 0.09	0.75 ± 0.09	0.8 ± 0.1	0.8 ± 0.1	0.9 ± 0.1
	0.60 ± 0.06	0.6 ± 0.1	0.8 ± 0.1	0.71 ± 0.06	0.8 ± 0.1	0.8 ± 0.1	0.78 ± 0.07	0.8 ± 0.2
PDSW / NDUFB10	0.6 ± 0.1	0.62 ± 0.06	0.7 ± 0.1	0.54 ± 0.08	0.7 ± 0.1	0.58 ± 0.07	0.59 ± 0.09	0.7 ± 0.1
	0.6 ± 0.1	0.82 ± 0.09	0.8 ± 0.1	0.7 ± 0.1	0.6 ± 0.1	0.74 ± 0.08	0.68 ± 0.09	0.61 ± 0.09
	0.60 ± 0.09	0.69 ± 0.09	0.6 ± 0.1	0.61 ± 0.07	0.8 ± 0.2	0.7 ± 0.1	0.69 ± 0.06	0.76 ± 0.09
NDUFA10	0.57 ± 0.05	0.63 ± 0.07	0.59 ± 0.04	0.7 ± 0.2	0.60 ± 0.04	0.70 ± 0.07	0.64 ± 0.07	0.57 ± 0.04
	0.63 ± 0.06	0.57 ± 0.05	0.66 ± 0.05	0.63 ± 0.06	0.8 ± 0.1	0.60 ± 0.04	0.66 ± 0.07	0.72 ± 0.07
	0.50 ± 0.05	0.57 ± 0.06	0.66 ± 0.08	0.72 ± 0.09	0.74 ± 0.07	0.61 ± 0.09	0.62 ± 0.05	0.60 ± 0.05
NDUFS5	0.6 ± 0.2	0.41 ± 0.07	0.43 ± 0.05	0.42 ± 0.07	0.41 ± 0.05	0.45 ± 0.05	0.9 ± 0.1	0.8 ± 0.2
	0.52 ± 0.08	0.45 ± 0.08	0.52 ± 0.08	0.7 ± 0.1	0.65 ± 0.07	0.51 ± 0.09	0.56 ± 0.05	0.64 ± 0.05
	0.8 ± 0.2	0.5 ± 0.2	0.64 ± 0.09	0.52 ± 0.06	0.40 ± 0.03	0.55 ± 0.07	0.6 ± 0.1	0.42 ± 0.07
NDUFA3	0.63 ± 0.09	0.77 ± 0.07	0.69 ± 0.06	0.61 ± 0.08	0.64 ± 0.05	0.65 ± 0.08	0.66 ± 0.06	0.7 ± 0.1
	0.66 ± 0.08	0.70 ± 0.07	0.65 ± 0.06	0.65 ± 0.07	0.68 ± 0.05	0.7 ± 0.1	0.57 ± 0.04	0.74 ± 0.09
	0.73 ± 0.08	0.9 ± 0.1	0.78 ± 0.07	0.8 ± 0.1	0.9 ± 0.1	0.58 ± 0.07	0.57 ± 0.09	0.7 ± 0.1
NDUFB3	0.8 ± 0.1	0.81 ± 0.07	0.78 ± 0.05	0.85 ± 0.09	1.0 ± 0.2	1.0 ± 0.1	0.61 ± 0.07	0.72 ± 0.09
	0.77 ± 0.04	0.81 ± 0.05	0.63 ± 0.06	0.8 ± 0.1	0.9 ± 0.1	0.7 ± 0.1	0.77 ± 0.07	0.66 ± 0.06
	1.1 ± 0.1	0.9 ± 0.1	0.66 ± 0.05	0.9 ± 0.1	0.66 ± 0.05	1.01 ± 0.08	0.78 ± 0.07	1.1 ± 0.2
NDUFC2	0.51 ± 0.08	0.42 ± 0.05	0.64 ± 0.08	0.46 ± 0.03	0.48 ± 0.06	0.48 ± 0.06	0.50 ± 0.05	0.52 ± 0.07
	0.43 ± 0.08	0.54 ± 0.09	0.45 ± 0.04	0.45 ± 0.03	0.44 ± 0.05	0.46 ± 0.04	0.49 ± 0.05	0.44 ± 0.03
	0.55 ± 0.07	0.54 ± 0.08	0.46 ± 0.07	0.60 ± 0.07	0.5 ± 0.1	0.53 ± 0.05	0.55 ± 0.06	0.58 ± 0.09
NDUFB4	0.38 ± 0.04	0.52 ± 0.09	0.52 ± 0.05	0.44 ± 0.04	0.54 ± 0.04	0.54 ± 0.05	0.47 ± 0.04	0.46 ± 0.04
	0.53 ± 0.04	0.60 ± 0.09	0.51 ± 0.04	0.59 ± 0.04	0.48 ± 0.04	0.60 ± 0.06	0.56 ± 0.05	0.50 ± 0.03
	0.51 ± 0.07	0.46 ± 0.04	0.46 ± 0.04	0.44 ± 0.04	0.49 ± 0.04	0.52 ± 0.04	0.47 ± 0.06	0.51 ± 0.03
NDUFA13	1.0 ± 0.3	0.8 ± 0.2	0.83 ± 0.08	1.2 ± 0.3	0.7 ± 0.1	1.0 ± 0.1	0.86 ± 0.06	1.1 ± 0.1
	1.0 ± 0.2	1.0 ± 0.1	1.0 ± 0.2	1.2 ± 0.2	1.0 ± 0.2	1.0 ± 0.1	0.9 ± 0.1	0.9 ± 0.1
	0.8 ± 0.2	0.8 ± 0.1	1.0 ± 0.1	1.1 ± 0.1	1.0 ± 0.1	1.2 ± 0.1	1.0 ± 0.2	0.9 ± 0.1
NDUFB6	0.8 ± 0.1	0.69 ± 0.09	0.9 ± 0.2	0.72 ± 0.08	0.91 ± 0.07	1.1 ± 0.3	0.73 ± 0.07	1.1 ± 0.1
	0.89 ± 0.07	0.70 ± 0.07	0.81 ± 0.06	0.83 ± 0.08	0.90 ± 0.08	0.69 ± 0.07	0.73 ± 0.09	0.57 ± 0.06
	0.74 ± 0.08	0.77 ± 0.06	1.03 ± 0.08	0.71 ± 0.09	0.69 ± 0.07	0.77 ± 0.05	0.76 ± 0.06	0.9 ± 0.1
NDUFB7	0.8 ± 0.1	0.71 ± 0.09	1.0 ± 0.1	0.8 ± 0.1	0.79 ± 0.09	0.8 ± 0.1	0.9 ± 0.1	0.9 ± 0.1
	0.8 ± 0.1	0.7 ± 0.1	0.7 ± 0.1	0.8 ± 0.1	0.8 ± 0.1	0.9 ± 0.1	0.9 ± 0.1	0.73 ± 0.09
	0.8 ± 0.1	0.8 ± 0.1	0.9 ± 0.1	0.80 ± 0.09	0.7 ± 0.1	0.74 ± 0.08	0.9 ± 0.1	0.8 ± 0.1
NDUFB9	0.51 ± 0.06	0.45 ± 0.07	0.53 ± 0.09	0.6 ± 0.1	0.47 ± 0.07	0.57 ± 0.09	0.49 ± 0.04	0.48 ± 0.07
	0.59 ± 0.06	0.55 ± 0.05	0.50 ± 0.04	0.47 ± 0.04	0.6 ± 0.1	0.51 ± 0.07	0.52 ± 0.05	0.44 ± 0.05
	0.51 ± 0.05	0.61 ± 0.09	0.57 ± 0.05	0.50 ± 0.05	0.56 ± 0.08	0.61 ± 0.06	0.52 ± 0.06	0.58 ± 0.07

NDUFB2	0.8 ± 0.1	0.6 ± 0.1	0.7 ± 0.1	0.46 ± 0.04	0.7 ± 0.1	0.9 ± 0.2	0.61 ± 0.08	0.9 ± 0.2
	0.7 ± 0.2	0.72 ± 0.09	0.6 ± 0.1	0.7 ± 0.1	0.7 ± 0.1	0.8 ± 0.1	0.8 ± 0.1	0.8 ± 0.1
	1.0 ± 0.1	0.48 ± 0.05	0.62 ± 0.06	0.67 ± 0.08	0.8 ± 0.1	0.60 ± 0.06	0.61 ± 0.07	0.56 ± 0.07
NDUFB8	0.9 ± 0.2	0.8 ± 0.1	0.80 ± 0.09	0.68 ± 0.07	0.76 ± 0.07	0.69 ± 0.07	0.79 ± 0.09	0.9 ± 0.1
	0.67 ± 0.08	0.8 ± 0.1	0.67 ± 0.09	0.72 ± 0.06	0.92 ± 0.08	0.8 ± 0.1	0.85 ± 0.07	0.76 ± 0.06
	0.6 ± 0.1	0.8 ± 0.1	0.85 ± 0.08	0.76 ± 0.09	0.8 ± 0.1	0.75 ± 0.08	0.8 ± 0.1	0.75 ± 0.09
ESSS / NDUFB11	1.03 ± 0.09	1.00 ± 0.08	0.8 ± 0.1	0.93 ± 0.09	1.4 ± 0.2	1.0 ± 0.1	1.2 ± 0.2	0.9 ± 0.1
	0.9 ± 0.1	1.2 ± 0.1	0.9 ± 0.2	0.98 ± 0.09	1.1 ± 0.2	0.94 ± 0.11	1.0 ± 0.2	1.0 ± 0.2
	1.03 ± 0.05	1.0 ± 0.1	0.91 ± 0.08	1.1 ± 0.1	0.89 ± 0.08	0.96 ± 0.09	0.88 ± 0.05	1.10 ± 0.09
KFYI / NDUFC1	0.33 ± 0.04	0.6 ± 0.1	0.42 ± 0.05	0.56 ± 0.09	0.41 ± 0.06	0.46 ± 0.04	0.38 ± 0.04	0.58 ± 0.08
	0.48 ± 0.07	0.49 ± 0.07	0.40 ± 0.05	0.41 ± 0.04	0.37 ± 0.05	0.41 ± 0.08	0.37 ± 0.07	0.39 ± 0.04
	0.46 ± 0.08	0.35 ± 0.04	0.46 ± 0.09	0.41 ± 0.04	0.43 ± 0.05	0.47 ± 0.07	0.51 ± 0.06	0.4 ± 0.2
MNLL/ NDUFB1	0.64 ± 0.06	0.53 ± 0.06	0.68 ± 0.09	0.60 ± 0.04	0.79 ± 0.09	0.8 ± 0.1	0.74 ± 0.06	0.63 ± 0.08
	0.64 ± 0.05	0.61 ± 0.07	0.62 ± 0.07	0.63 ± 0.05	0.65 ± 0.06	0.8 ± 0.1	0.57 ± 0.05	0.69 ± 0.05
	0.75 ± 0.08	0.57 ± 0.09	0.67 ± 0.08	0.64 ± 0.08	0.80 ± 0.09	0.82 ± 0.07	0.56 ± 0.05	0.60 ± 0.07
MWFE / NDUFA1	0.49 ± 0.05	0.32 ± 0.03	0.38 ± 0.04	0.48 ± 0.08	0.54 ± 0.09	0.5 ± 0.1	0.6 ± 0.1	0.57 ± 0.09
	0.4 ± 0.1	0.65 ± 0.9	0.48 ± 0.07	0.49 ± 0.06	0.52 ± 0.06	0.42 ± 0.08	0.42 ± 0.05	0.6 ± 0.1
	0.44 ± 0.08	0.33 ± 0.02	0.6 ± 0.1	0.47 ± 0.06	0.5 ± 0.1	0.39 ± 0.04	0.40 ± 0.05	0.6 ± 0.2

The NDUFS2 (49 kDa in the ovine naming, Table S2) subunit has higher average RMSD values (between 0.6 and 1.0 nm). This is probably caused by the absence of the Q module subunits that usually surround and stabilize this subunit, and, consequently, the solvent exposure. The NDUFA11, NDUFB5, NDUFAB1, NDUFC1 (KFYI) and the NDUFA1 (MWFE) subunits have the lowest average RMSD values between the supernumerary subunits (below 0.5 nm). On the other hand, the NDUFA13, NDUFB6, NDUFB7 and NDUFB11 (ESSS) subunits shows the higher average RMSD values (over 0.8 nm) because of the large oscillations of their C-terminals (see below). The other supernumerary subunits have generally intermediate RMSD values (between 0.5 and 0.8 nm).

Fig. S10. Backbone beads RMSF *vs.* residue number of the P+ module subunits in the wtO^{op} structures.
Each panel label corresponds to the equivalent subunit in Table S1. The RMSF values corresponding to the three replicas are in brown, orange, and light brown, respectively.

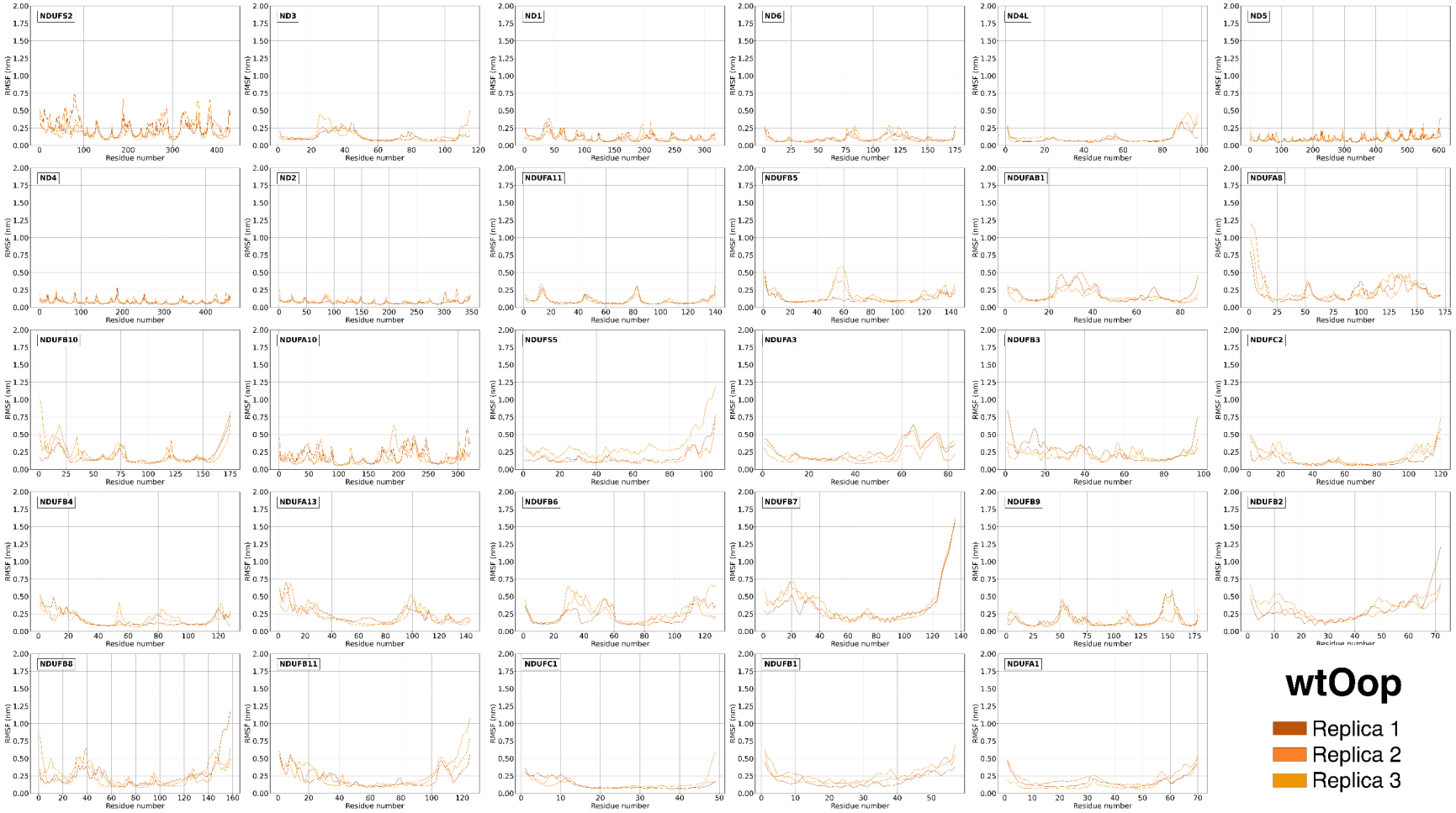

Fig. S11. Backbone beads RMSF *vs.* residue number plots of the P+ module subunits in the wtO^{cl} structures.
Each panel label corresponds to the equivalent subunit in Table S1. The RMSF values corresponding to the three replicas are in brown, orange, and light brown, respectively.

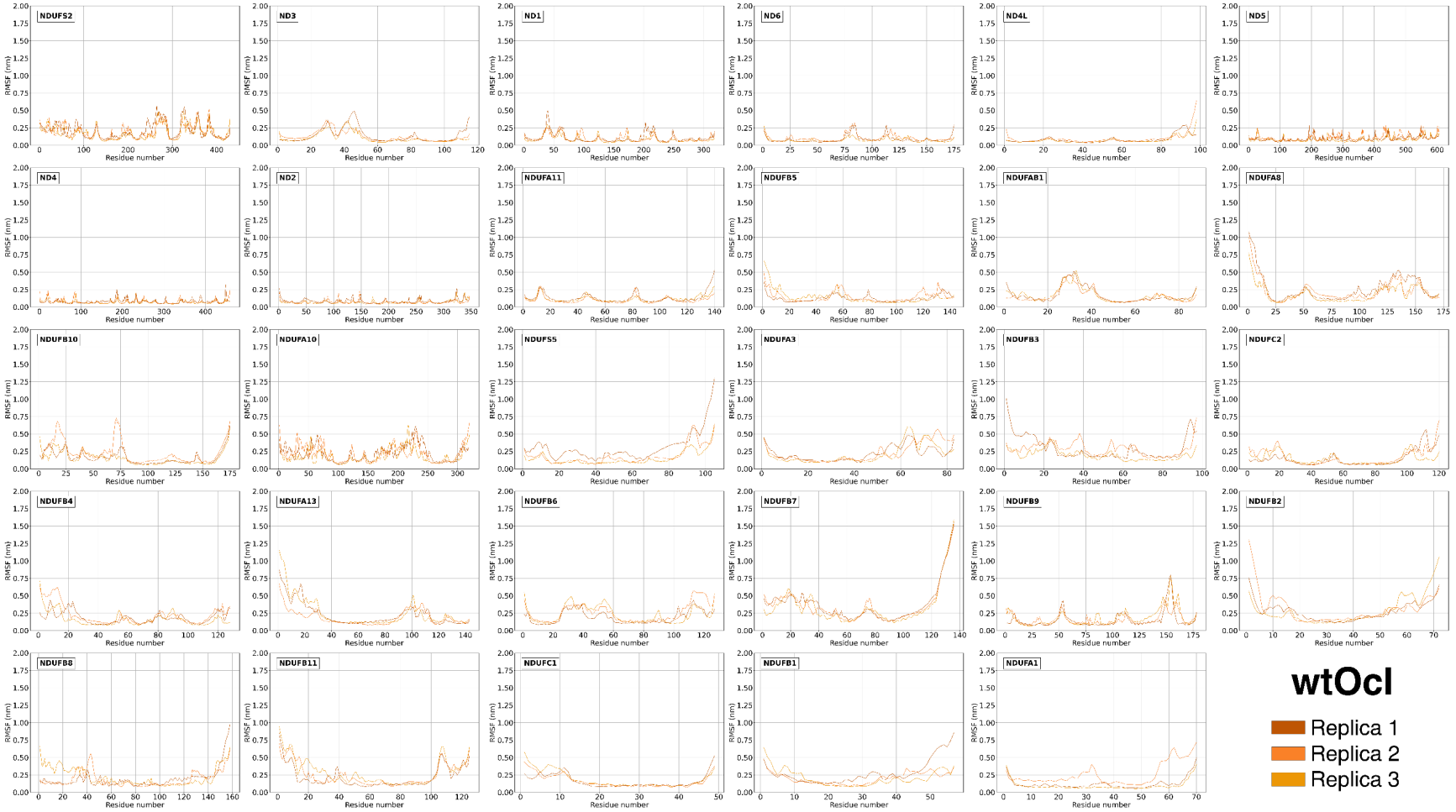

Fig. S12. Backbone beads RMSF *vs.* residue number plots of the P+ module subunits in the wtH^{op} structures.
Each panel label corresponds to the equivalent subunit in Table S1. The RMSF values corresponding to the three replicas are in brown, maroon, and crimson, respectively.

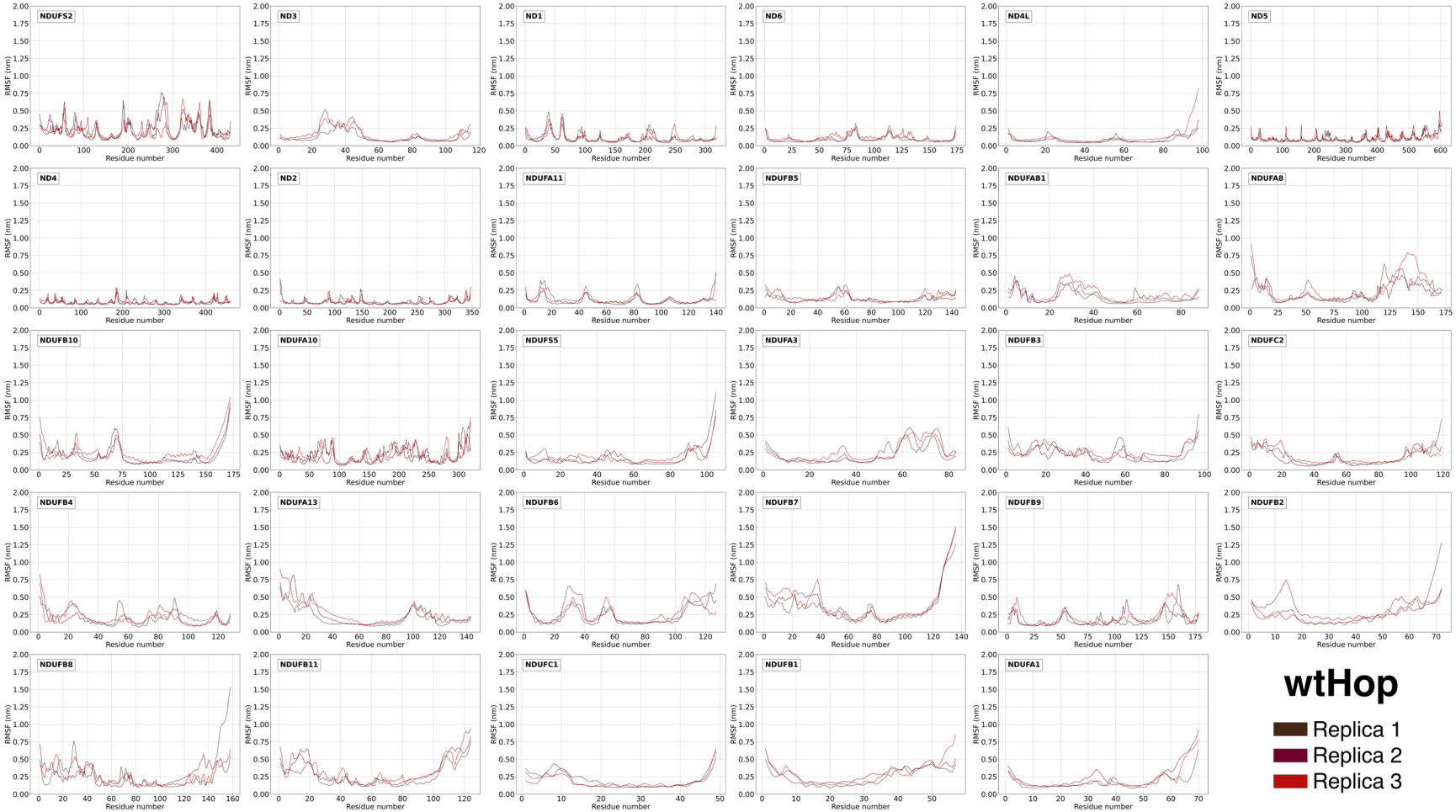

Fig. S13. Backbone beads RMSF *vs.* residue number plots of the P+ module subunits in the wtH^{cl} structures.
Each panel label corresponds to the equivalent subunit in Table S1. The RMSF values corresponding to the three replicas are in brown, maroon, and crimson, respectively.

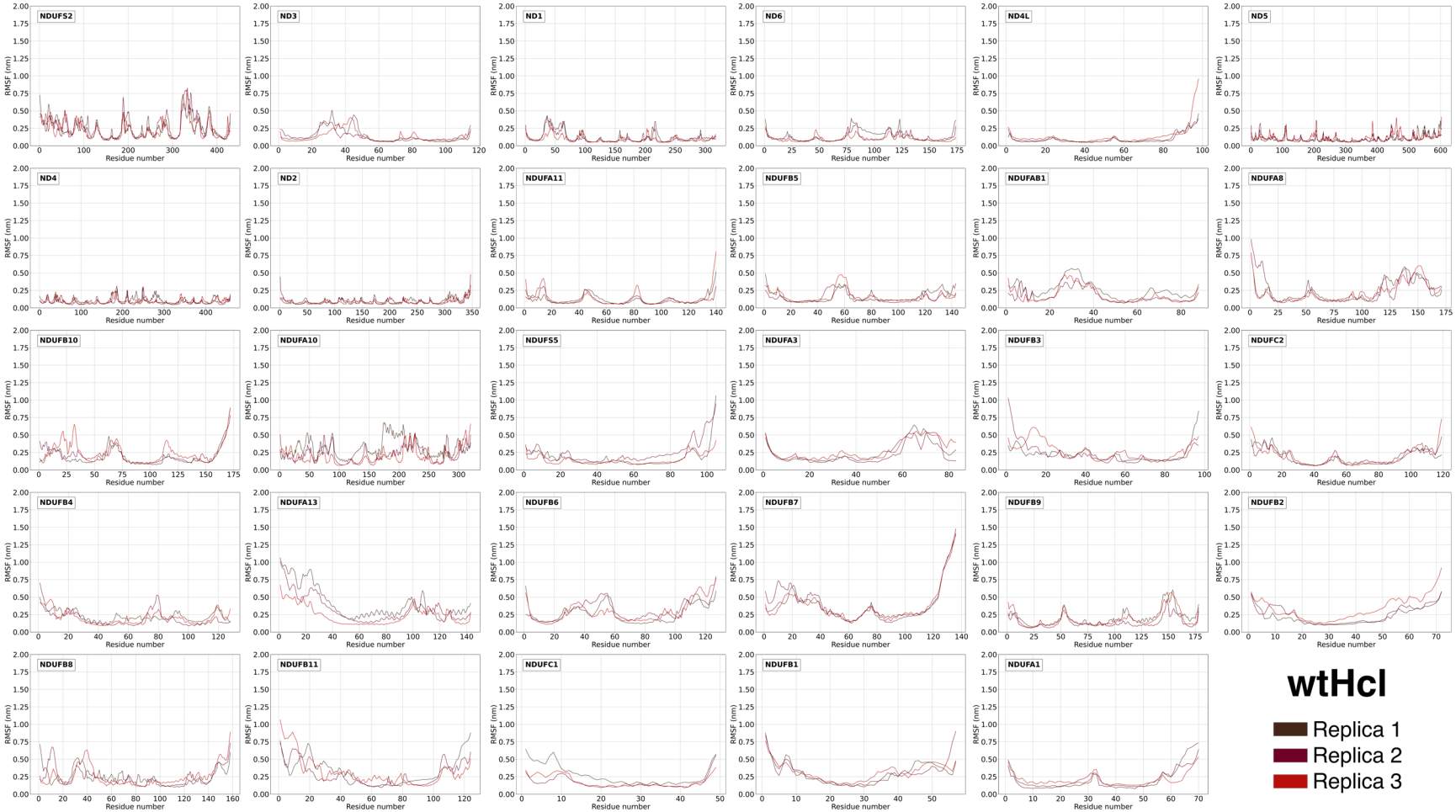

Fig. S14. Backbone beads RMSF *vs.* residue number plots of the P+ module subunits in the m1H^{op} structures.
Each panel label corresponds to the equivalent subunit in Table S1. The RMSF values corresponding to the three replicas are in navy, royal blue, and fountain blue, respectively.

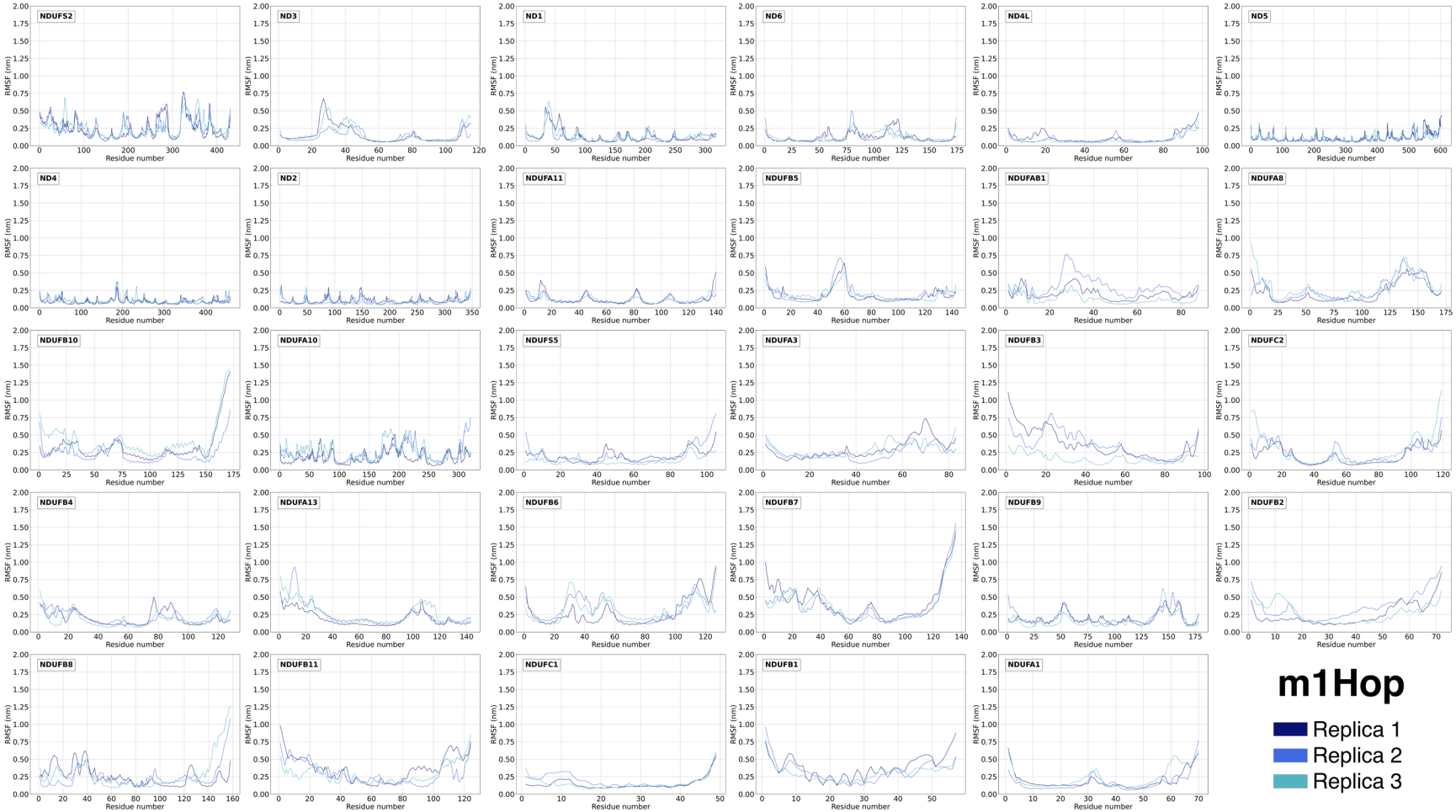

Fig. S15. Backbone beads RMSF *vs.* residue number plots of the P+ module subunits in the m1H^{cl} structures.
Each panel label corresponds to the equivalent subunit in Table S1. The RMSF values corresponding to the three replicas are in navy, royal blue, and fountain blue, respectively.

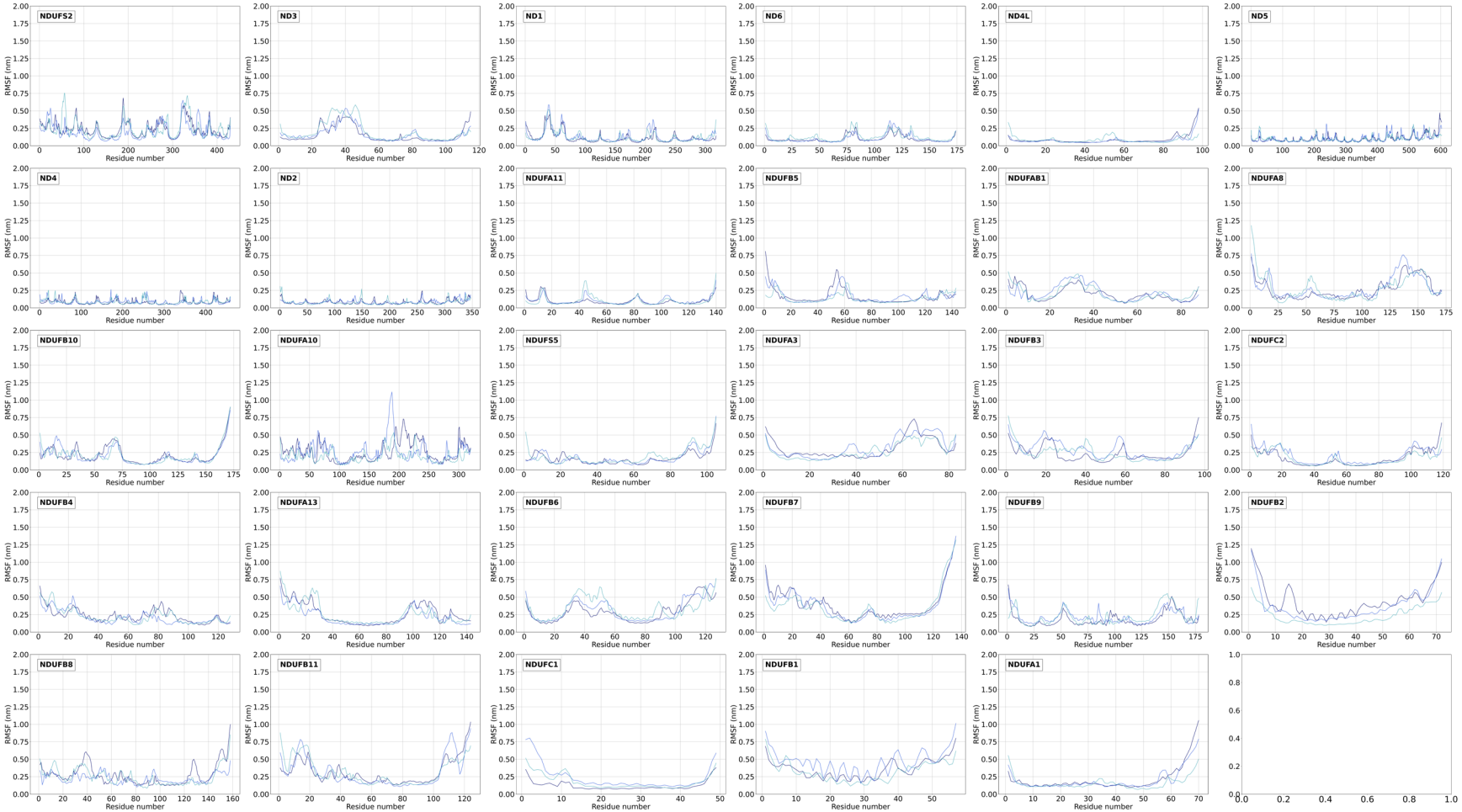

Fig. S16. Backbone beads RMSF *vs.* residue number plots of the P+ module subunits in the m3H^{op} structures.
Each panel label corresponds to the equivalent subunit in Table S1. The RMSF values corresponding to the three replicas are in pine, dark lime, and lime, respectively.

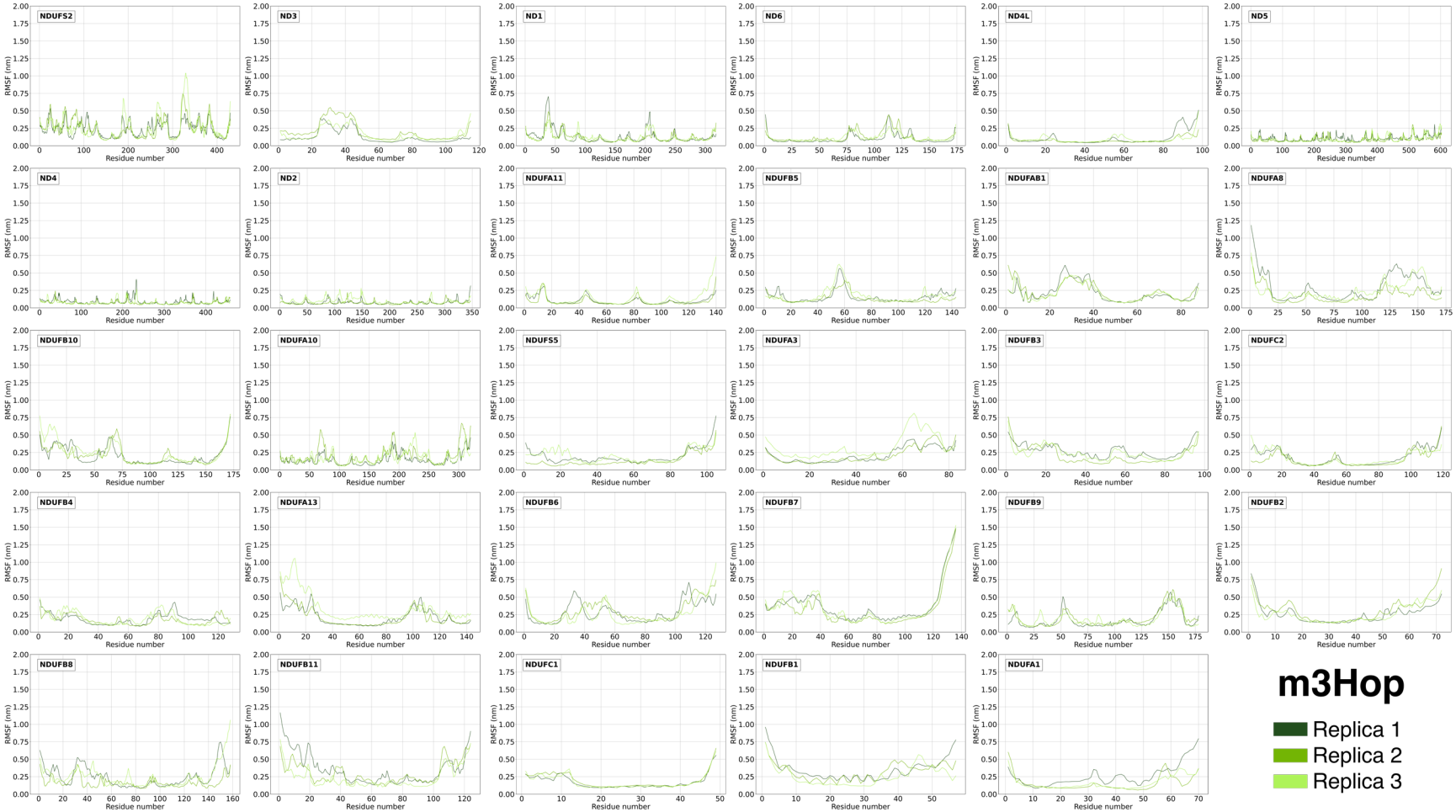

Fig. S17. Backbone beads RMSF *vs.* residue number plots of the P+ module subunits in the m3H^{cl} structures.
Each panel label corresponds to the equivalent subunit in Table S1. The RMSF values corresponding to the three replicas are in pine, dark lime, and lime, respectively.

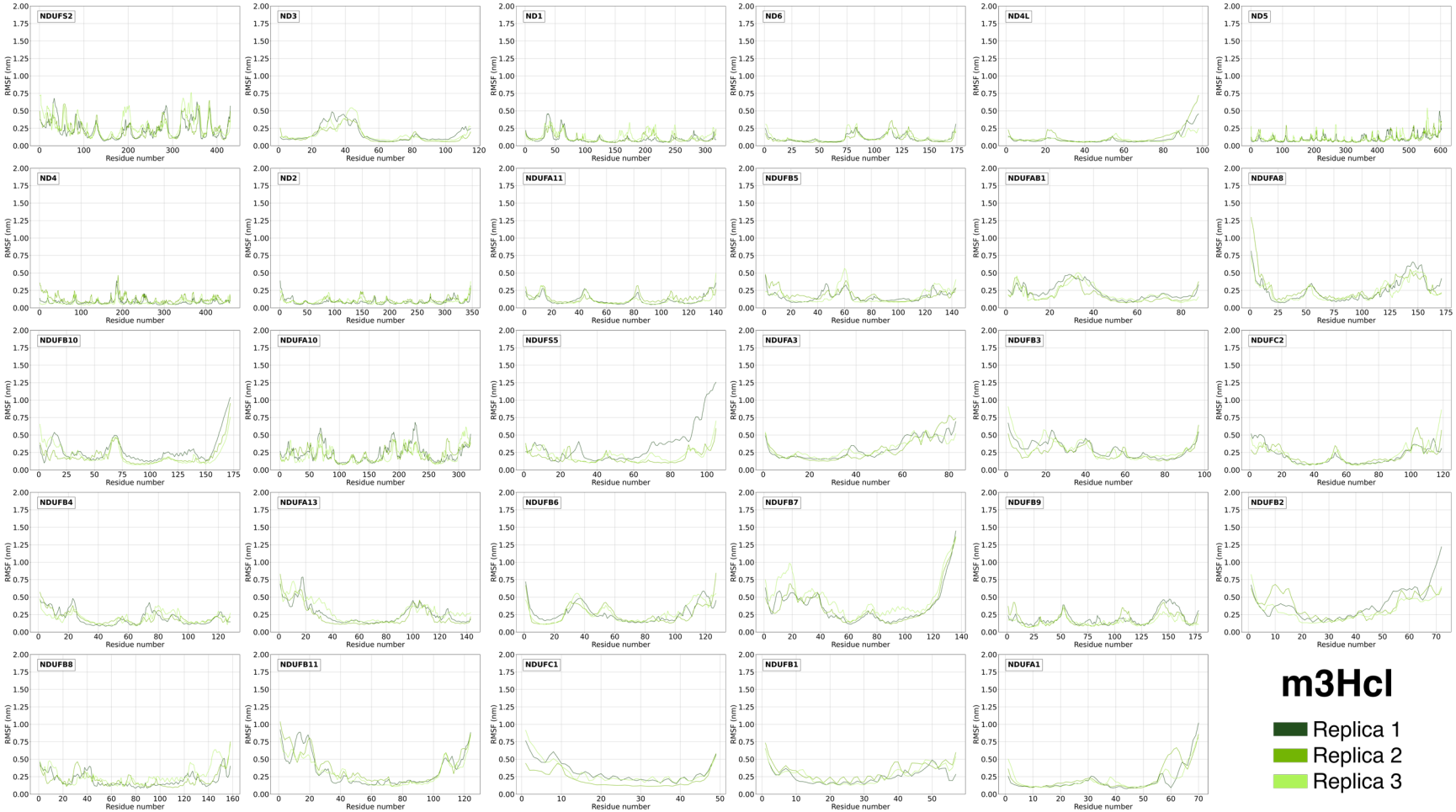

Table S6. Average and standard deviation of RMSF values (in nm) of backbone beads for each subunit of ovine and human P+ module. For each subunit, the ovine and human abbreviation (see Table S1) is reported. Each subunits line corresponds to a different replica.

Ovine/Human subunit	wtO^{op}	wtO^{cl}	wtH^{op}	wtH^{cl}	m1H^{op}	m1H^{cl}	m3H^{op}	m3H^{cl}
49 kDa / NDUFS2	0.3 ± 0.1	0.3 ± 0.1	0.3 ± 0.1	0.3 ± 0.2	0.3 ± 0.2	0.3 ± 0.1	0.3 ± 0.1	0.3 ± 0.2
	0.3 ± 0.1	0.3 ± 0.1	0.3 ± 0.2	0.3 ± 0.2	0.3 ± 0.2	0.3 ± 0.1	0.3 ± 0.2	0.3 ± 0.1
	0.3 ± 0.1	0.3 ± 0.1	0.3 ± 0.1	0.3 ± 0.2	0.3 ± 0.1	0.3 ± 0.1	0.3 ± 0.2	0.3 ± 0.2
ND3	0.14 ± 0.09	0.2 ± 0.1	0.2 ± 0.1	0.2 ± 0.1	0.2 ± 0.1	0.2 ± 0.1	0.15 ± 0.09	0.2 ± 0.1
	0.2 ± 0.1	0.2 ± 0.1	0.2 ± 0.1	0.15 ± 0.07	0.15 ± 0.07	0.2 ± 0.1	0.2 ± 0.1	0.2 ± 0.1
	0.16 ± 0.07	0.2 ± 0.1	0.2 ± 0.1	0.15 ± 0.09	0.2 ± 0.1	0.2 ± 0.1	0.2 ± 0.1	0.2 ± 0.1
ND1	0.12 ± 0.05	0.13 ± 0.08	0.14 ± 0.08	0.15 ± 0.08	0.14 ± 0.09	0.14 ± 0.08	0.1 ± 0.1	0.12 ± 0.08
	0.13 ± 0.07	0.13 ± 0.07	0.12 ± 0.07	0.13 ± 0.07	0.14 ± 0.07	0.15 ± 0.09	0.13 ± 0.08	0.13 ± 0.07
	0.14 ± 0.07	0.14 ± 0.08	0.14 ± 0.07	0.10 ± 0.05	0.16 ± 0.09	0.14 ± 0.08	0.13 ± 0.06	0.15 ± 0.07
ND6	0.12 ± 0.05	0.12 ± 0.05	0.12 ± 0.05	0.15 ± 0.07	0.13 ± 0.07	0.12 ± 0.05	0.12 ± 0.07	0.12 ± 0.06
	0.11 ± 0.05	0.11 ± 0.05	0.10 ± 0.05	0.14 ± 0.07	0.13 ± 0.07	0.14 ± 0.07	0.16 ± 0.09	0.11 ± 0.06
	0.13 ± 0.06	0.11 ± 0.05	0.13 ± 0.05	0.12 ± 0.06	0.14 ± 0.08	0.17 ± 0.08	0.14 ± 0.06	0.14 ± 0.07
ND4L	0.2 ± 0.1	0.10 ± 0.06	0.11 ± 0.05	0.11 ± 0.07	0.13 ± 0.09	0.11 ± 0.08	0.1 ± 0.1	0.2 ± 0.1
	0.10 ± 0.07	0.09 ± 0.08	0.09 ± 0.06	0.11 ± 0.08	0.11 ± 0.08	0.09 ± 0.07	0.10 ± 0.05	0.2 ± 0.1
	0.13 ± 0.09	0.1 ± 0.1	0.1 ± 0.1	0.1 ± 0.1	0.09 ± 0.06	0.10 ± 0.06	0.10 ± 0.06	0.10 ± 0.05
ND5	0.13 ± 0.07	0.12 ± 0.05	0.12 ± 0.06	0.11 ± 0.06	0.12 ± 0.06	0.13 ± 0.07	0.12 ± 0.05	0.13 ± 0.07
	0.10 ± 0.05	0.14 ± 0.05	0.11 ± 0.05	0.12 ± 0.06	0.12 ± 0.06	0.12 ± 0.06	0.11 ± 0.05	0.12 ± 0.06
	0.11 ± 0.05	0.12 ± 0.05	0.11 ± 0.06	0.13 ± 0.05	0.12 ± 0.06	0.11 ± 0.05	0.12 ± 0.06	0.13 ± 0.07
ND4	0.11 ± 0.04	0.10 ± 0.04	0.08 ± 0.03	0.11 ± 0.05	0.09 ± 0.04	0.10 ± 0.04	0.09 ± 0.04	0.09 ± 0.05
	0.10 ± 0.04	0.10 ± 0.04	0.09 ± 0.03	0.09 ± 0.04	0.10 ± 0.04	0.09 ± 0.04	0.09 ± 0.04	0.13 ± 0.06
	0.11 ± 0.05	0.09 ± 0.04	0.09 ± 0.04	0.10 ± 0.04	0.11 ± 0.06	0.09 ± 0.04	0.09 ± 0.04	0.09 ± 0.04
ND2	0.09 ± 0.04	0.09 ± 0.04	0.10 ± 0.04	0.11 ± 0.04	0.11 ± 0.05	0.09 ± 0.04	0.09 ± 0.04	0.10 ± 0.05
	0.10 ± 0.04	0.09 ± 0.04	0.09 ± 0.05	0.11 ± 0.05	0.11 ± 0.05	0.09 ± 0.04	0.09 ± 0.03	0.12 ± 0.04
	0.10 ± 0.04	0.09 ± 0.04	0.09 ± 0.04	0.09 ± 0.04	0.09 ± 0.04	0.09 ± 0.05	0.11 ± 0.05	0.12 ± 0.05
NDUFA11	0.11 ± 0.06	0.12 ± 0.06	0.14 ± 0.09	0.13 ± 0.08	0.12 ± 0.08	0.11 ± 0.07	0.13 ± 0.07	0.13 ± 0.08
	0.10 ± 0.06	0.12 ± 0.05	0.11 ± 0.07	0.12 ± 0.06	0.12 ± 0.06	0.13 ± 0.08	0.10 ± 0.07	0.15 ± 0.06
	0.12 ± 0.07	0.16 ± 0.07	0.13 ± 0.06	0.1 ± 0.1	0.13 ± 0.06	0.11 ± 0.08	0.2 ± 0.1	0.13 ± 0.07
NDUFB5	0.2 ± 0.1	0.18 ± 0.09	0.14 ± 0.05	0.18 ± 0.09	0.2 ± 0.1	0.2 ± 0.1	0.17 ± 0.09	0.19 ± 0.08
	0.19 ± 0.09	0.18 ± 0.09	0.16 ± 0.06	0.17 ± 0.08	0.22 ± 0.08	0.18 ± 0.09	0.16 ± 0.08	0.21 ± 0.08
	0.17 ± 0.06	0.16 ± 0.08	0.18 ± 0.08	0.2 ± 0.1	0.20 ± 0.08	0.17 ± 0.08	0.2 ± 0.1	0.2 ± 0.1
NDUFAB1	0.19 ± 0.09	0.21 ± 0.09	0.18 ± 0.08	0.2 ± 0.1	0.22 ± 0.09	0.2 ± 0.1	0.2 ± 0.1	0.2 ± 0.1
	0.2 ± 0.1	0.18 ± 0.09	0.14 ± 0.09	0.2 ± 0.1	0.3 ± 0.1	0.2 ± 0.1	0.3 ± 0.1	0.2 ± 0.1
	0.2 ± 0.1	0.2 ± 0.1	0.2 ± 0.1	0.2 ± 0.1	0.20 ± 0.09	0.2 ± 0.1	0.2 ± 0.1	0.2 ± 0.1

NDUFA8	0.3 ± 0.2	0.2 ± 0.1	0.3 ± 0.2	0.3 ± 0.2	0.3 ± 0.2	0.3 ± 0.2	0.4 ± 0.2	0.3 ± 0.2
	0.3 ± 0.2	0.3 ± 0.2	0.3 ± 0.1	0.3 ± 0.2	0.3 ± 0.2	0.3 ± 0.2	0.2 ± 0.2	0.3 ± 0.2
	0.3 ± 0.1	0.3 ± 0.2	0.3 ± 0.2	0.3 ± 0.1	0.3 ± 0.2	0.3 ± 0.2	0.3 ± 0.1	0.3 ± 0.2
PDSW / NDUFB10	0.3 ± 0.1	0.2 ± 0.1	0.3 ± 0.1	0.2 ± 0.1	0.3 ± 0.2	0.2 ± 0.1	0.2 ± 0.1	0.3 ± 0.2
	0.3 ± 0.1	0.3 ± 0.2	0.2 ± 0.2	0.3 ± 0.2	0.3 ± 0.2	0.2 ± 0.1	0.2 ± 0.1	0.2 ± 0.1
	0.3 ± 0.2	0.2 ± 0.1	0.3 ± 0.2	0.3 ± 0.1	0.4 ± 0.2	0.2 ± 0.1	0.3 ± 0.2	0.2 ± 0.1
NDUFA10	0.2 ± 0.1	0.3 ± 0.1	0.2 ± 0.1	0.4 ± 0.2	0.21 ± 0.09	0.3 ± 0.2	0.2 ± 0.1	0.3 ± 0.1
	0.2 ± 0.1	0.3 ± 0.1	0.2 ± 0.1	0.2 ± 0.1	0.3 ± 0.1	0.3 ± 0.2	0.3 ± 0.1	0.3 ± 0.1
	0.2 ± 0.1	0.3 ± 0.1	0.3 ± 0.1	0.3 ± 0.2	0.3 ± 0.1	0.3 ± 0.1	0.20 ± 0.09	0.2 ± 0.1
NDUFS5	0.4 ± 0.2	0.2 ± 0.1	0.2 ± 0.1	0.2 ± 0.1	0.20 ± 0.08	0.19 ± 0.09	0.3 ± 0.2	0.4 ± 0.3
	0.2 ± 0.1	0.2 ± 0.1	0.2 ± 0.2	0.3 ± 0.2	0.3 ± 0.2	0.3 ± 0.1	0.2 ± 0.1	0.2 ± 0.1
	0.3 ± 0.2	0.3 ± 0.2	0.2 ± 0.1	0.17 ± 0.08	0.14 ± 0.06	0.2 ± 0.1	0.3 ± 0.1	0.2 ± 0.1
NDUFA3	0.3 ± 0.1	0.3 ± 0.1	0.2 ± 0.1	0.3 ± 0.2	0.4 ± 0.2	0.3 ± 0.1	0.3 ± 0.1	0.4 ± 0.2
	0.23 ± 0.09	0.3 ± 0.1	0.3 ± 0.1	0.3 ± 0.1	0.3 ± 0.1	0.4 ± 0.2	0.3 ± 0.1	0.4 ± 0.2
	0.3 ± 0.1	0.3 ± 0.1	0.3 ± 0.1	0.3 ± 0.2	0.4 ± 0.1	0.3 ± 0.1	0.4 ± 0.2	0.3 ± 0.1
NDUFB3	0.3 ± 0.2	0.3 ± 0.1	0.3 ± 0.1	0.3 ± 0.1	0.4 ± 0.2	0.3 ± 0.1	0.3 ± 0.2	0.3 ± 0.1
	0.21 ± 0.09	0.3 ± 0.1	0.3 ± 0.1	0.3 ± 0.2	0.4 ± 0.2	0.4 ± 0.1	0.3 ± 0.2	0.30 ± 0.09
	0.4 ± 0.1	0.4 ± 0.2	0.3 ± 0.1	0.4 ± 0.2	0.21 ± 0.09	0.3 ± 0.1	0.3 ± 0.1	0.4 ± 0.2
NDUFC2	0.2 ± 0.1	0.19 ± 0.09	0.2 ± 0.1	0.2 ± 0.1	0.2 ± 0.1	0.2 ± 0.1	0.2 ± 0.1	0.2 ± 0.1
	0.2 ± 0.1	0.2 ± 0.2	0.2 ± 0.1	0.2 ± 0.1	0.2 ± 0.1	0.2 ± 0.1	0.2 ± 0.1	0.2 ± 0.1
	0.2 ± 0.1	0.2 ± 0.1	0.2 ± 0.1	0.2 ± 0.2	0.3 ± 0.2	0.2 ± 0.1	0.2 ± 0.1	0.2 ± 0.1
NDUFB4	0.2 ± 0.1	0.3 ± 0.1	0.24 ± 0.08	0.24 ± 0.08	0.2 ± 0.1	0.3 ± 0.1	0.21 ± 0.08	0.2 ± 0.1
	0.20 ± 0.08	0.3 ± 0.1	0.2 ± 0.1	0.2 ± 0.1	0.2 ± 0.1	0.2 ± 0.1	0.21 ± 0.08	0.22 ± 0.08
	0.20 ± 0.1	0.3 ± 0.1	0.22 ± 0.09	0.21 ± 0.08	0.2 ± 0.1	0.2 ± 0.1	0.22 ± 0.09	0.24 ± 0.08
NDUFA13	0.4 ± 0.3	0.3 ± 0.2	0.2 ± 0.1	0.5 ± 0.3	0.2 ± 0.2	0.3 ± 0.2	0.2 ± 0.1	0.3 ± 0.2
	0.3 ± 0.2	0.3 ± 0.2	0.3 ± 0.2	0.4 ± 0.2	0.3 ± 0.2	0.3 ± 0.1	0.3 ± 0.2	0.3 ± 0.2
	0.4 ± 0.2	0.3 ± 0.2	0.4 ± 0.2	0.3 ± 0.2	0.3 ± 0.2	0.3 ± 0.2	0.4 ± 0.2	0.3 ± 0.2
NDUFB6	0.4 ± 0.2	0.3 ± 0.1	0.3 ± 0.2	0.3 ± 0.1	0.3 ± 0.2	0.5 ± 0.3	0.3 ± 0.2	0.4 ± 0.2
	0.3 ± 0.1	0.3 ± 0.1	0.3 ± 0.1	0.4 ± 0.2	0.4 ± 0.2	0.3 ± 0.2	0.3 ± 0.1	0.3 ± 0.1
	0.3 ± 0.1	0.3 ± 0.1	0.3 ± 0.1	0.3 ± 0.2	0.3 ± 0.1	0.4 ± 0.1	0.3 ± 0.2	0.3 ± 0.1
NDUFB7	0.4 ± 0.3	0.4 ± 0.3	0.4 ± 0.2	0.4 ± 0.3	0.5 ± 0.3	0.4 ± 0.2	0.4 ± 0.3	0.4 ± 0.2
	0.4 ± 0.3	0.4 ± 0.3	0.4 ± 0.3	0.4 ± 0.3	0.4 ± 0.3	0.4 ± 0.3	0.4 ± 0.3	0.4 ± 0.2
	0.4 ± 0.3	0.4 ± 0.3	0.5 ± 0.3	0.4 ± 0.3	0.4 ± 0.2	0.4 ± 0.2	0.4 ± 0.3	0.5 ± 0.2
NDUFB9	0.2 ± 0.1	0.2 ± 0.1	0.2 ± 0.1	0.3 ± 0.1	0.22 ± 0.08	0.2 ± 0.1	0.2 ± 0.1	0.21 ± 0.09
	0.18 ± 0.08	0.20 ± 0.09	0.20 ± 0.09	0.18 ± 0.08	0.26 ± 0.09	0.2 ± 0.1	0.2 ± 0.1	0.2 ± 0.1
	0.2 ± 0.1	0.2 ± 0.1	0.2 ± 0.1	0.2 ± 0.1	0.2 ± 0.1	0.2 ± 0.1	0.2 ± 0.1	0.18 ± 0.07

NDUFB2	0.4 ± 0.2	0.3 ± 0.2	0.3 ± 0.2	0.2 ± 0.1	0.3 ± 0.2	0.5 ± 0.2	0.3 ± 0.1	0.4 ± 0.2
	0.4 ± 0.2	0.3 ± 0.2	0.3 ± 0.1	0.3 ± 0.2	0.4 ± 0.2	0.4 ± 0.2	0.4 ± 0.2	0.4 ± 0.2
	0.3 ± 0.2	0.3 ± 0.1	0.3 ± 0.1	0.4 ± 0.2	0.3 ± 0.2	0.3 ± 0.1	0.3 ± 0.1	0.3 ± 0.1
NDUFB8	0.4 ± 0.2	0.3 ± 0.1	0.3 ± 0.1	0.3 ± 0.1	0.3 ± 0.1	0.3 ± 0.2	0.3 ± 0.2	0.3 ± 0.1
	0.3 ± 0.1	0.3 ± 0.1	0.3 ± 0.2	0.3 ± 0.1	0.3 ± 0.1	0.3 ± 0.1	0.21 ± 0.09	0.2 ± 0.1
	0.3 ± 0.2	0.3 ± 0.2	0.3 ± 0.1	0.3 ± 0.2	0.34 ± 0.3	0.3 ± 0.1	0.3 ± 0.2	0.3 ± 0.1
ESSS / NDUFB11	0.3 ± 0.2	0.3 ± 0.2	0.3 ± 0.2	0.3 ± 0.2	0.4 ± 0.2	0.4 ± 0.2	0.4 ± 0.2	0.4 ± 0.2
	0.4 ± 0.2	0.4 ± 0.2	0.4 ± 0.2	0.3 ± 0.2	0.4 ± 0.2	0.4 ± 0.2	0.4 ± 0.2	0.4 ± 0.2
	0.3 ± 0.1	0.3 ± 0.2	0.3 ± 0.2	0.4 ± 0.2	0.3 ± 0.2	0.4 ± 0.2	0.3 ± 0.1	0.3 ± 0.2
KFYI / NDUFC1	0.2 ± 0.1	0.2 ± 0.1	0.2 ± 0.1	0.3 ± 0.1	0.2 ± 0.1	0.14 ± 0.07	0.2 ± 0.1	0.3 ± 0.2
	0.17 ± 0.08	0.2 ± 0.1	0.2 ± 0.1	0.2 ± 0.1	0.2 ± 0.1	0.2 ± 0.2	0.2 ± 0.1	0.2 ± 0.1
	0.2 ± 0.1	0.2 ± 0.1	0.2 ± 0.1	0.18 ± 0.08	0.17 ± 0.09	0.2 ± 0.1	0.2 ± 0.1	0.3 ± 0.2
MNLL/ NDUFB1	0.3 ± 0.1	0.3 ± 0.1	0.3 ± 0.1	0.3 ± 0.1	0.4 ± 0.2	0.4 ± 0.1	0.4 ± 0.2	0.3 ± 0.09
	0.3 ± 0.1	0.3 ± 0.1	0.3 ± 0.1	0.3 ± 0.2	0.3 ± 0.2	0.5 ± 0.2	0.3 ± 0.1	0.4 ± 0.1
	0.3 ± 0.1	0.3 ± 0.1	0.3 ± 0.2	0.4 ± 0.1	0.4 ± 0.1	0.4 ± 0.1	0.3 ± 0.1	0.3 ± 0.1
MWFE / NDUFA1	0.2 ± 0.1	0.12 ± 0.08	0.2 ± 0.1	0.3 ± 0.2	0.2 ± 0.1	0.2 ± 0.2	0.3 ± 0.2	0.2 ± 0.2
	0.2 ± 0.1	0.3 ± 0.1	0.3 ± 0.2	0.2 ± 0.1	0.2 ± 0.1	0.2 ± 0.1	0.2 ± 0.1	0.3 ± 0.2
	0.2 ± 0.1	0.14 ± 0.07	0.3 ± 0.2	0.21 ± 0.09	0.3 ± 0.1	0.2 ± 0.1	0.2 ± 0.1	0.3 ± 0.2

The NDUFS2 (49 kDa in the ovine naming) subunit showed high average RMSF values (0.3 nm). As discussed above, these fluctuations are probably caused by the hydrophobic residues on the surface of this subunit, which are exposed to the solvent. The NDUFA11 and NDUFB5 subunits show the lower average RMSF values than the other supernumerary subunits (below 0.2 nm). The NDUFA3, NDUFA13, NDUFB6, NDUFB7, NDUFB2, NDUFB11 (ESSS) and NDUFB1 subunits have usually the highest average RMSF values (over 0.3 nm), which are caused by the large fluctuations of the N- and C-terminals.

Fig. S18. Radius of gyration (R_g) *vs.* simulation time plots of the P+ module subunits in the wtO^{op} structures.
Each panel label corresponds to the equivalent subunit in Table S1. The R_g values corresponding to the three replicas are in brown, orange, and light brown, respectively.

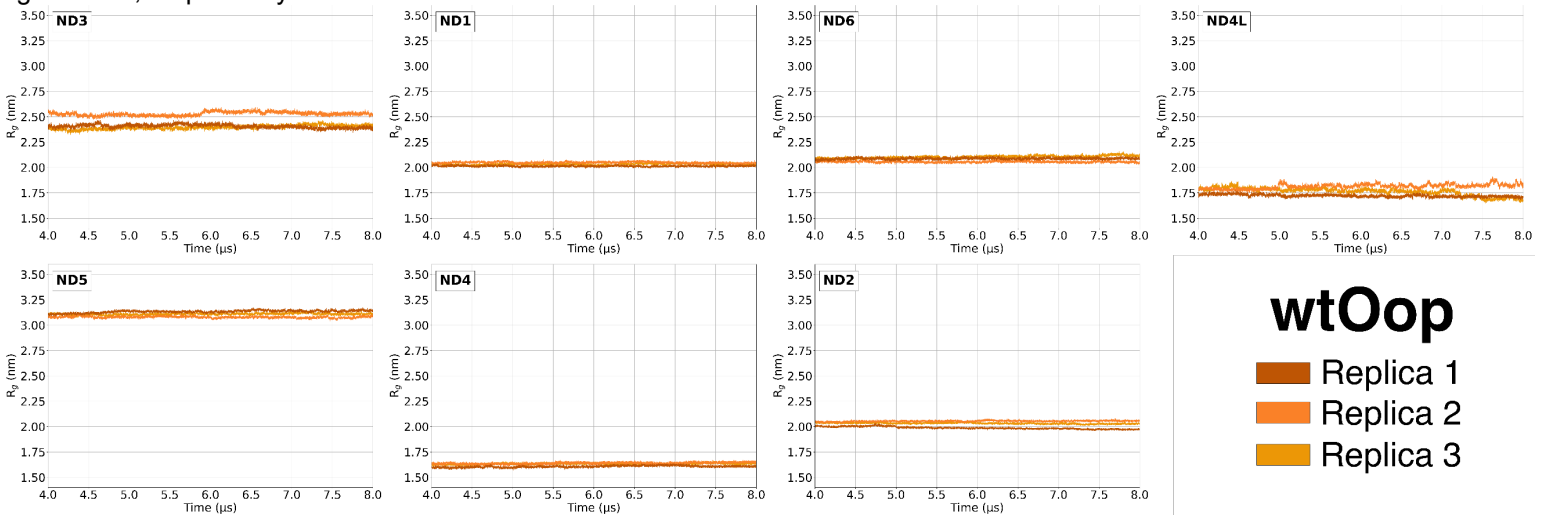

Fig. S19. Radius of gyration (R_g) *vs.* simulation time plots of the P+ module subunits in the wtO^{cl} structures.
Each panel label corresponds to the equivalent subunit in Table S1. The R_g values corresponding to the three replicas are in brown, orange, and light brown, respectively.

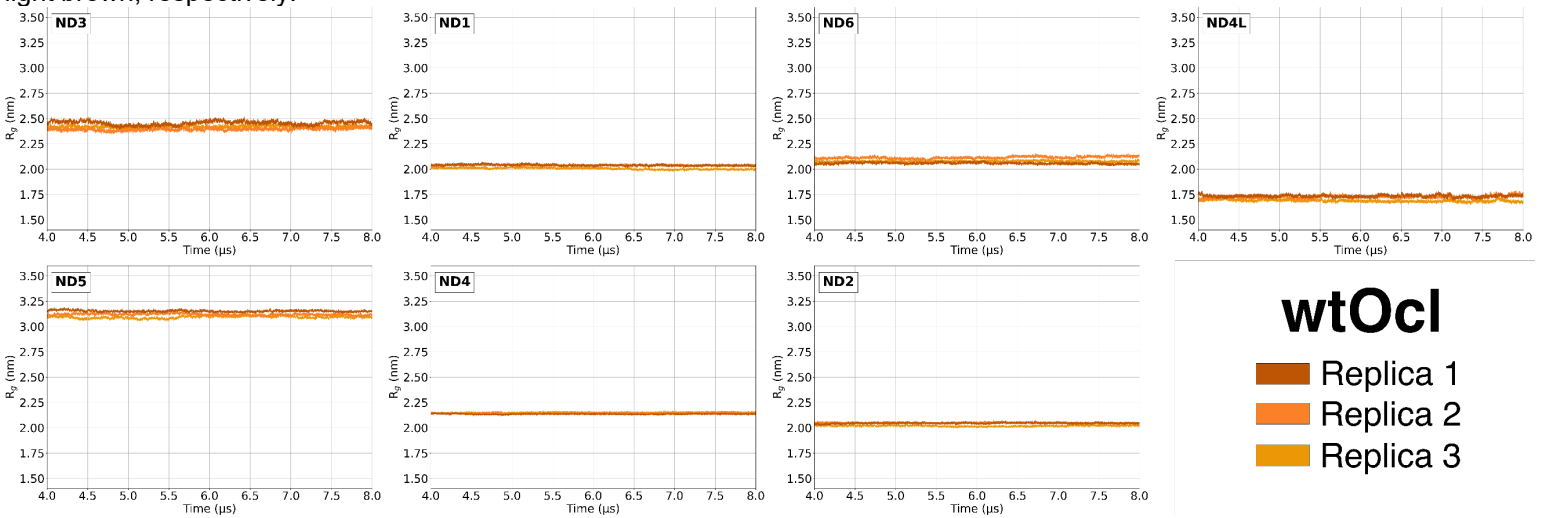

Fig. S20. Radius of gyration (R_g) *vs.* simulation time plots of the P+ module subunits in the wtH^{op} structures.
Each panel label corresponds to the equivalent subunit in Table S1. The R_g values corresponding to the three replicas are in brown, maroon, and crimson, respectively.

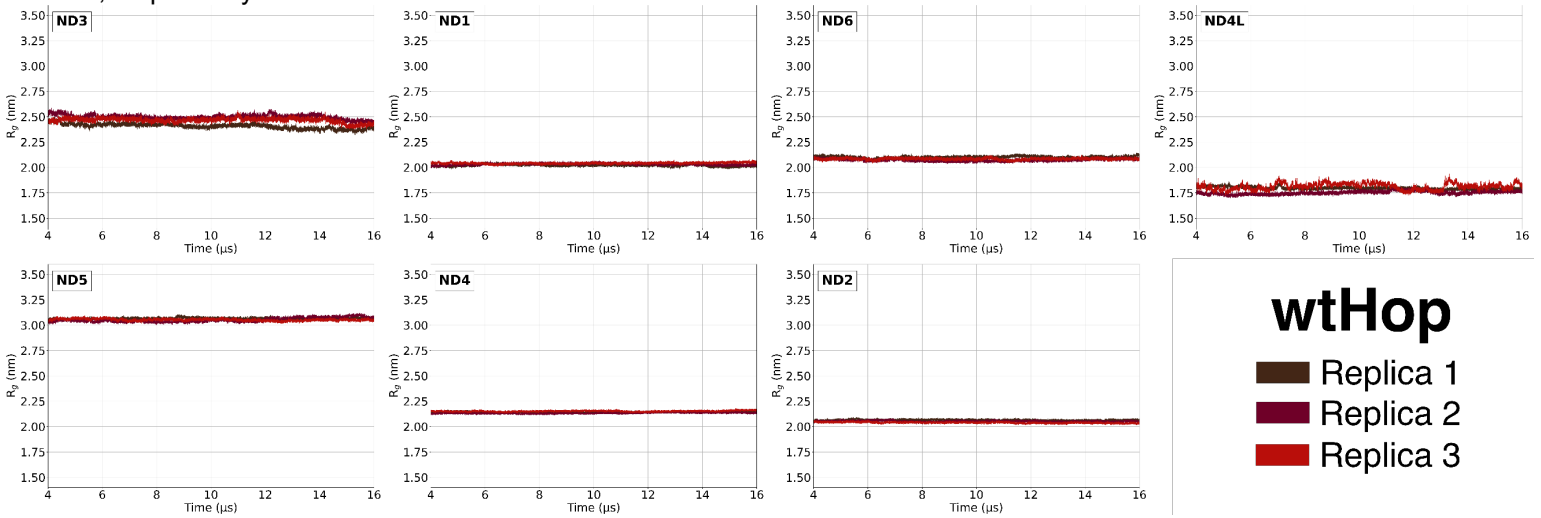

Fig. S21. Radius of gyration (R_g) *vs.* simulation time plots of the P+ module subunits in the wtHO^{cl} structures.
Each panel label corresponds to the equivalent subunit in Table S1. The R_g values corresponding to the three replicas are in brown, maroon, and crimson, respectively.

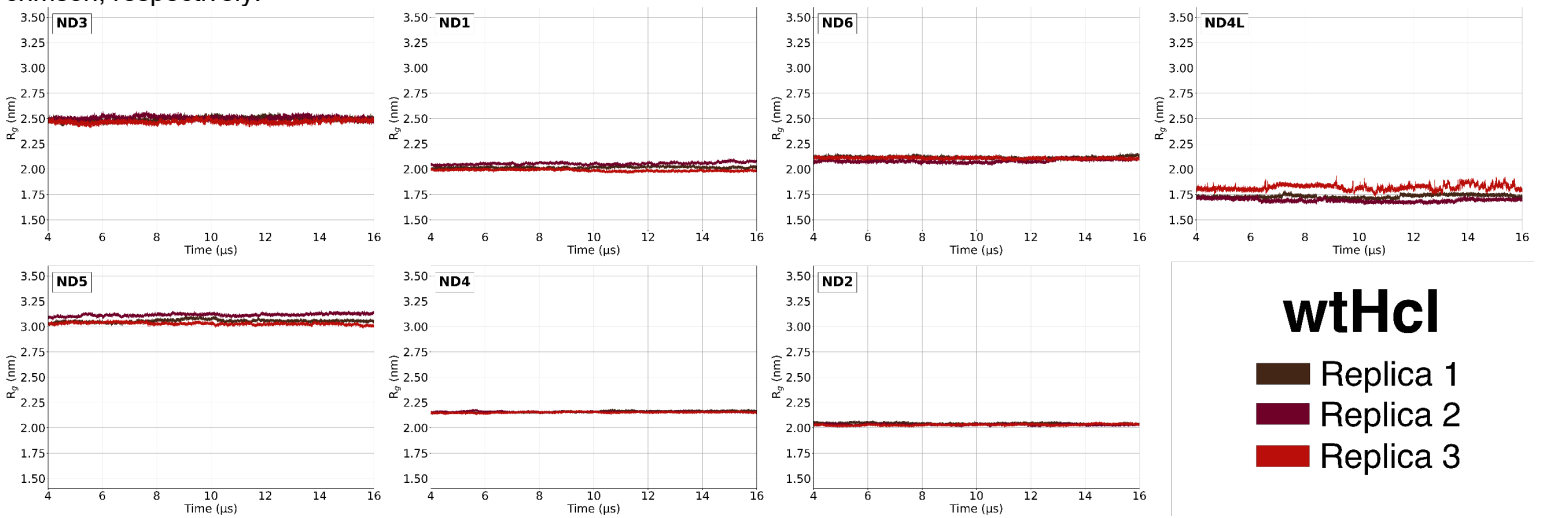

Fig. S22. Radius of gyration (R_g) *vs.* simulation time plots of the P+ module subunits in the m1H^{op} structures.
Each panel label corresponds to the equivalent subunit in Table S1. The R_g values corresponding to the three replicas are in navy, royal blue, and fountain blue, respectively.

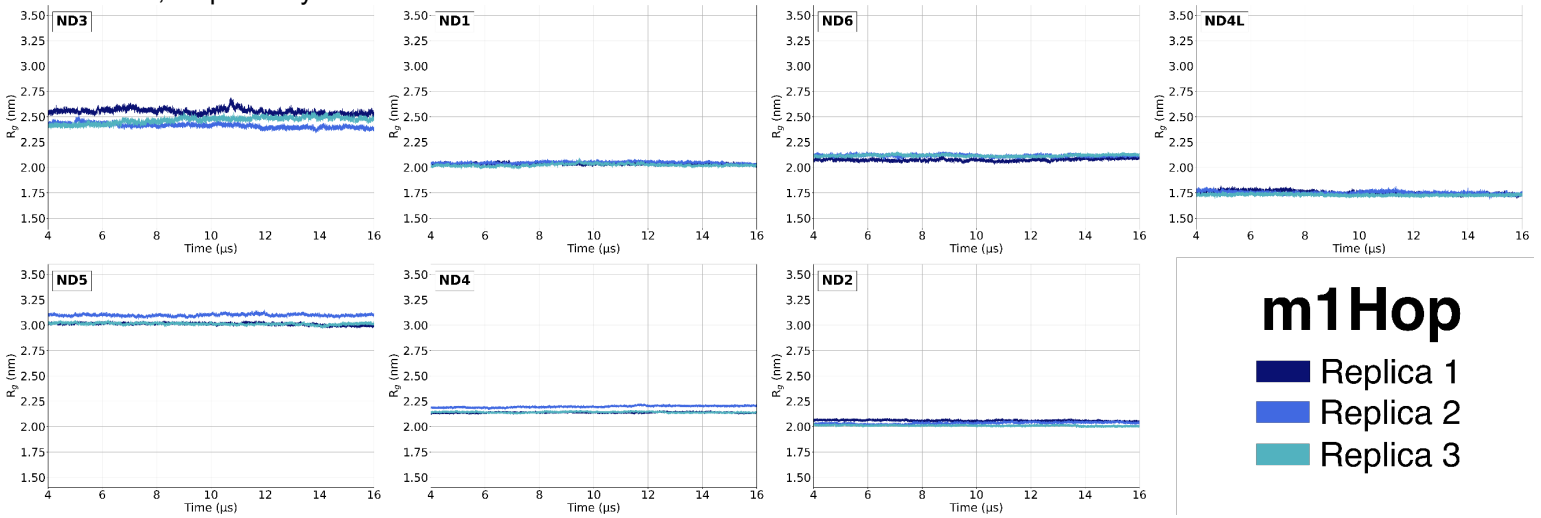

Fig. S23. Radius of gyration (R_g) *vs.* simulation time plots of the P+ module subunits in the m1H^{cl} structures.
Each panel label corresponds to the equivalent subunit in Table S1. The R_g values corresponding to the three replicas are in navy, royal blue, and fountain blue, respectively.

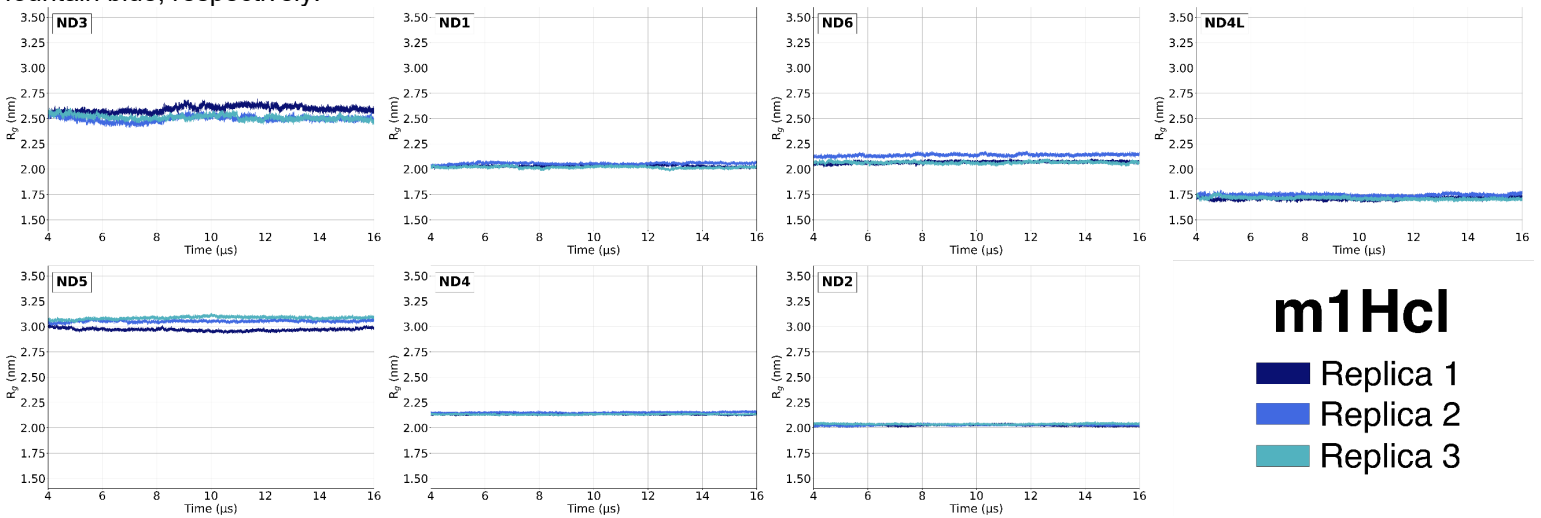

Fig. S24. Radius of gyration (R_g) *vs.* simulation time plots of the P+ module subunits in the m3H^{op} structures.
Each panel label corresponds to the equivalent subunit in Table S1. The R_g values corresponding to the three replicas are in pine, dark lime, and lime, respectively.

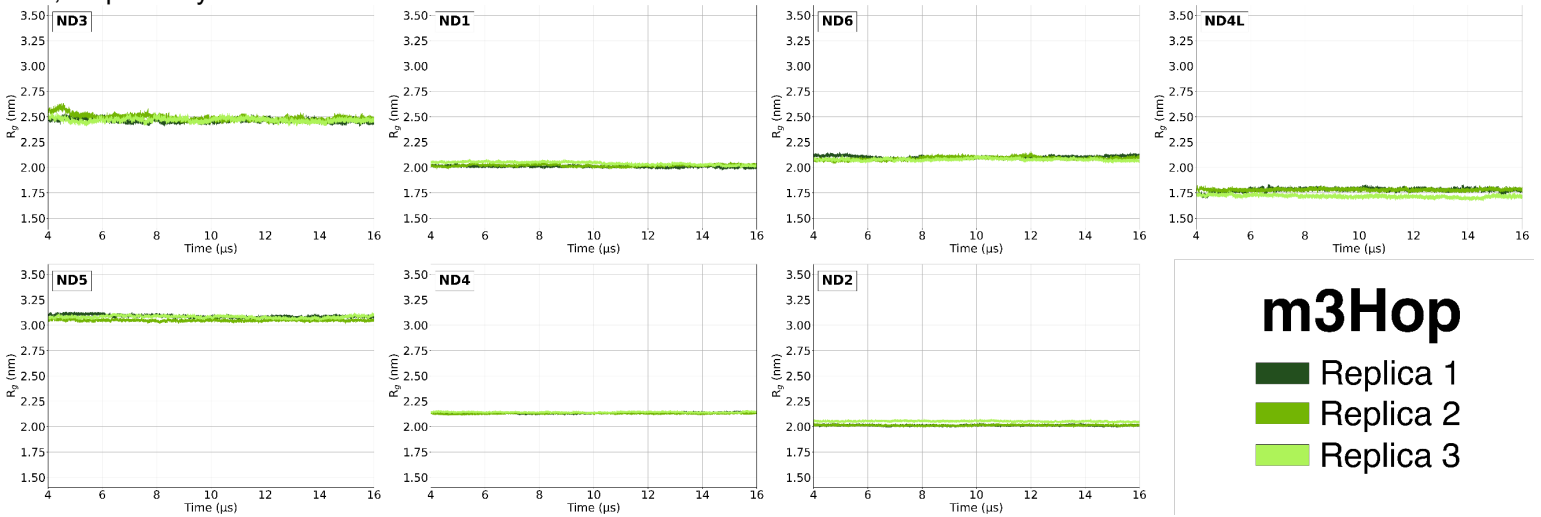

Fig. S25. Radius of gyration (R_g) *vs.* simulation time plots of the P+ module subunits in the m3H^{cl} structures.
Each panel label corresponds to the equivalent subunit in Table S1. The R_g values corresponding to the three replicas are in pine, dark lime, and lime, respectively.

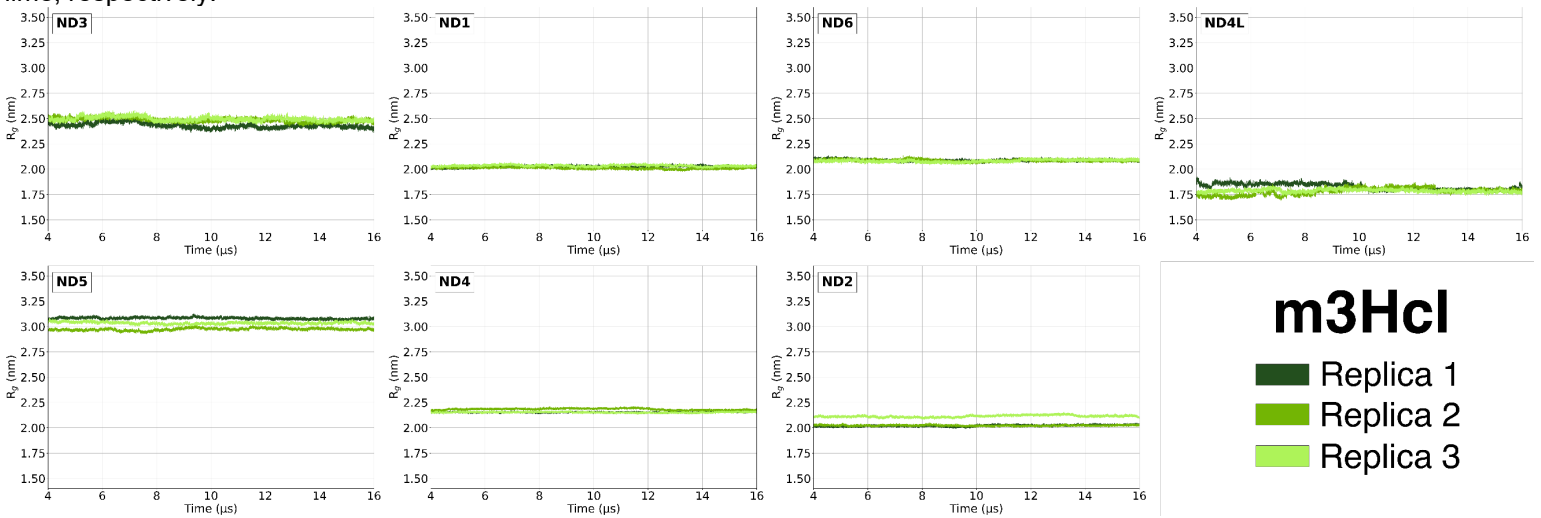

Fig. S26. Lipid density maps calculated on the summed trajectories of the wtH^{op} system.
Cardiolipin, POPC, POPE and POPI maps are in blue, orange, light blue and green, respectively. The section of P+ module is reported, and the subunits are colored according to Fig. 1B scheme.

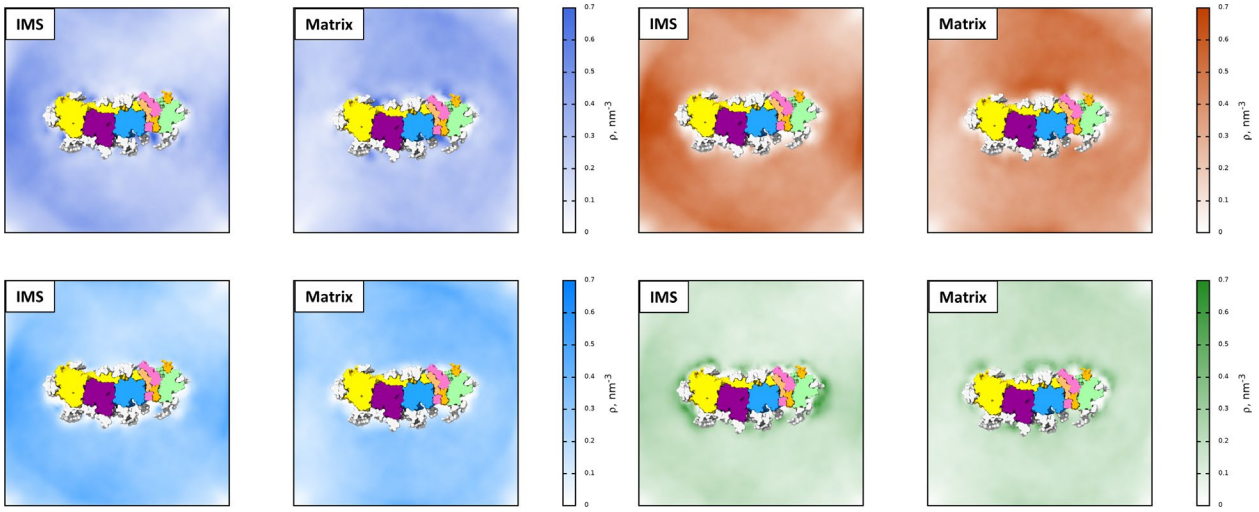

Fig. S27. Lipid density maps calculated on the summed trajectories of the 1mH^{op} system.
Cardiolipin, POPC, POPE and POPI maps are in blue, orange, light blue and green, respectively. The section of P+ module is reported, and the subunits are colored according to Fig. 1B scheme.

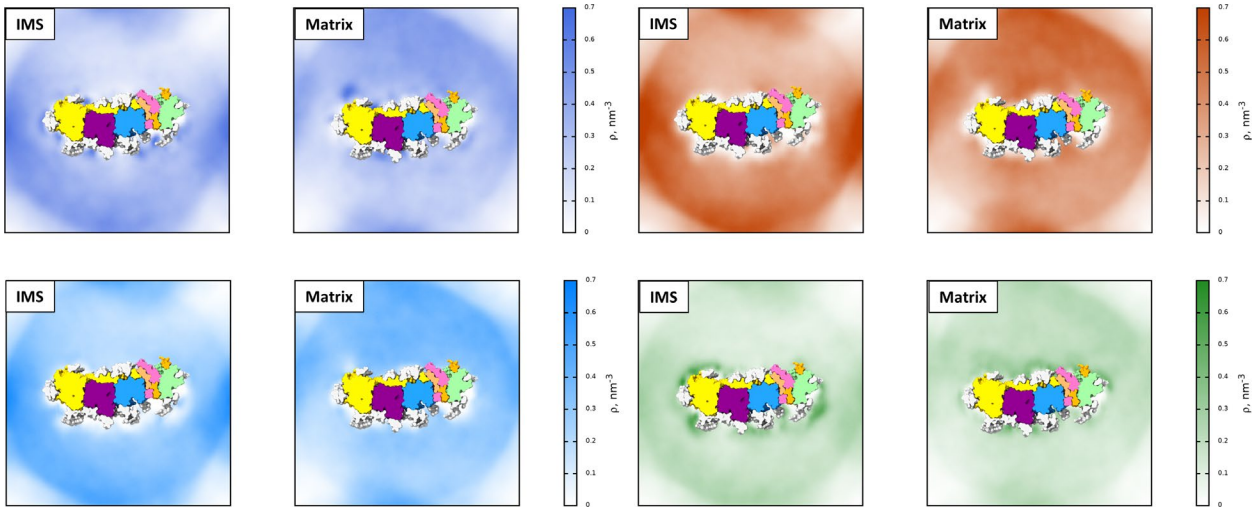

Fig. S28. Maps of lipid density on the summed trajectories of the 3mH^{op} system.
Cardiolipin, POPC, POPE and POPI maps are in blue, orange, light blue and green, respectively. The section of P+ module is reported, and the subunits are colored according to Fig. 1B scheme.

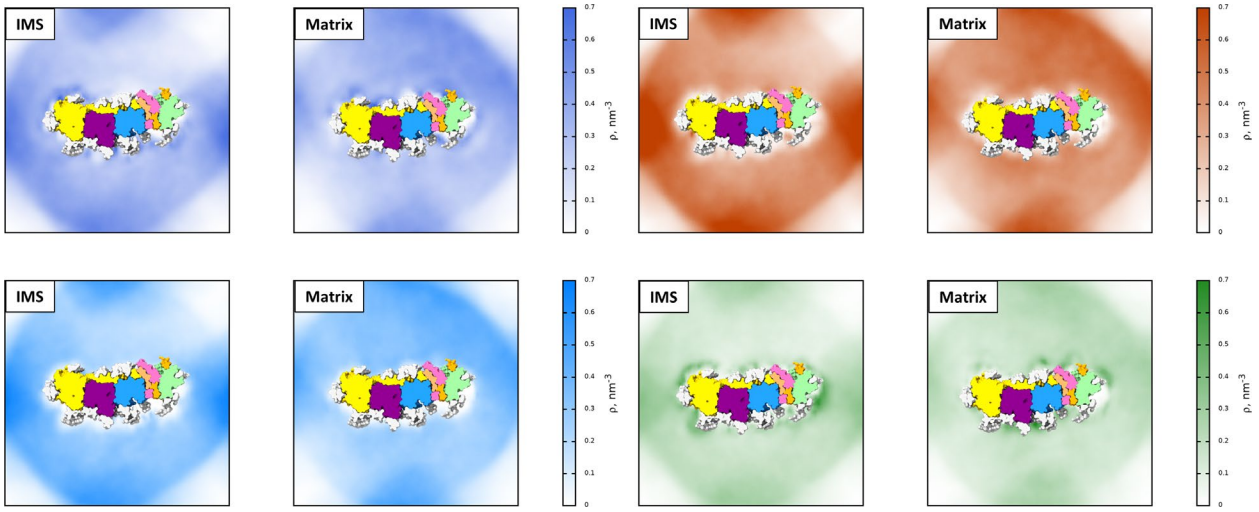

Fig. S29. Maps of lipid density on the summed trajectories of the wtH^{cl} system.
Cardiolipin, POPC, POPE and POPI maps are in blue, orange, light blue and green, respectively. The section of P+ module is reported, and the subunits are colored according to Fig. 1B scheme.

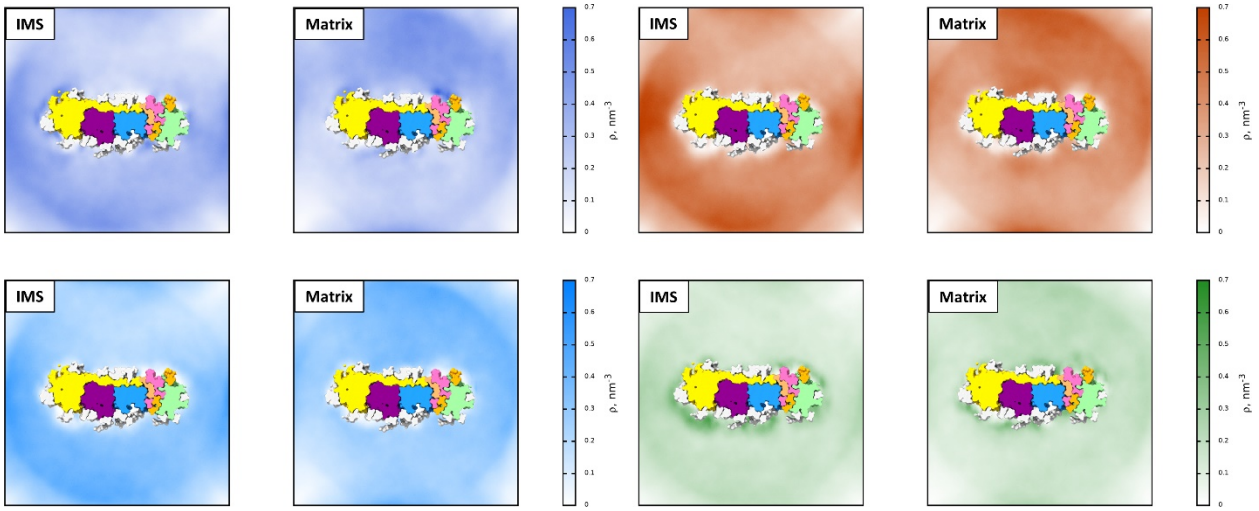

Fig. S30. Maps of lipid density on the summed trajectories of the 1mH^{cl} system.
Cardiolipin, POPC, POPE and POPI maps are in blue, orange, light blue and green, respectively. The section of P+ module is reported, and the subunits are colored according to Fig. 1B scheme.

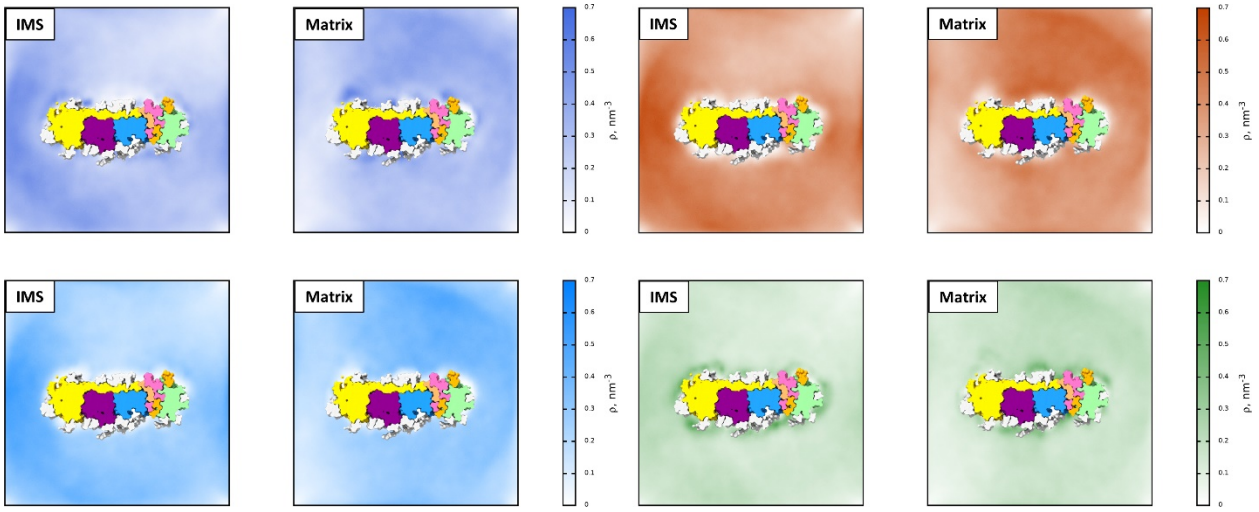

Fig. S31. Maps of lipid density on the summed trajectories of the 3mH^{cl} system.
Cardiolipin, POPC, POPE and POPI maps are in blue, orange, light blue and green, respectively. The section of P+ module is reported, and the subunits are colored according to Fig. 1B scheme.

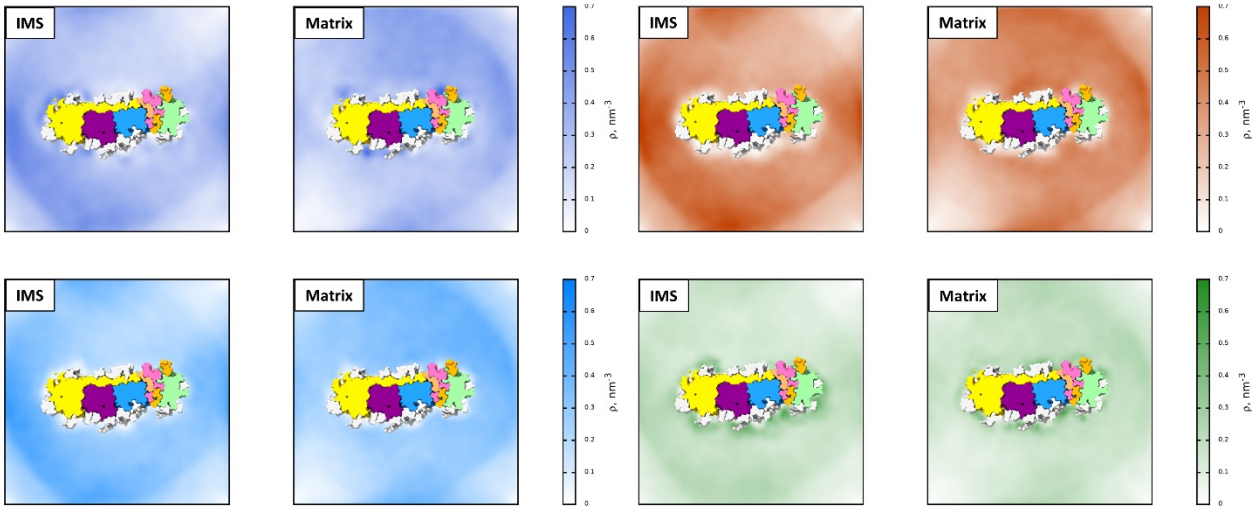

Fig. S32. Maps of lipid density on the summed trajectories of the wtO^{op} system.
Cardiolipin, POPC, POPE and POPI maps are in blue, orange, light blue and green, respectively. The section of P+ module is reported, and the subunits are colored according to Fig. 1B scheme.

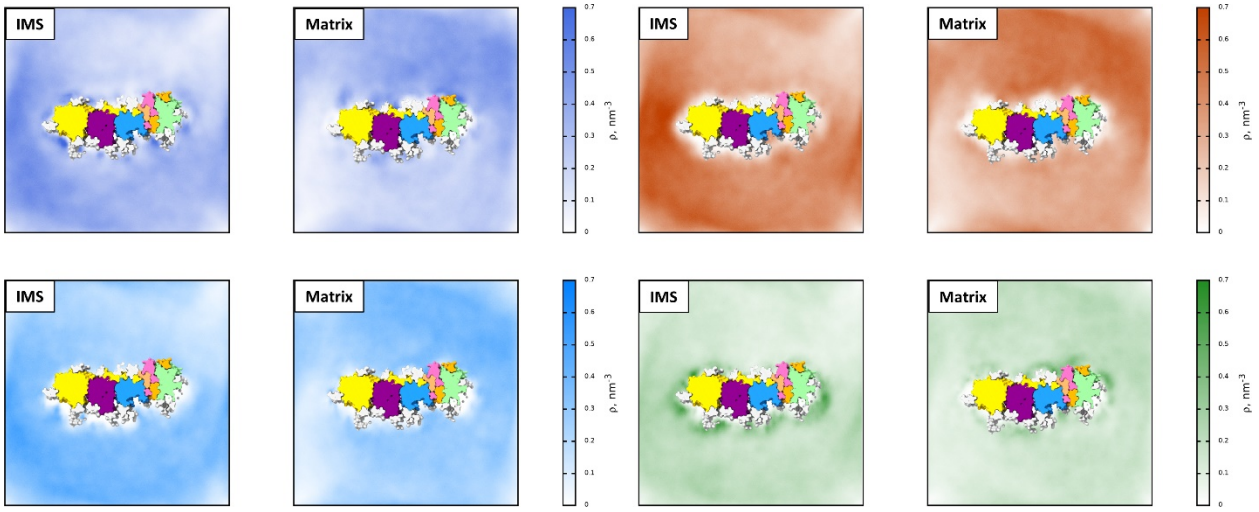

Fig. S33. Maps of lipid density on the summed trajectories of the wtO^{cl} system.
Cardiolipin, POPC, POPE and POPI maps are in blue, orange, light blue and green, respectively. The section of P+ module is reported, and the subunits are colored according to Fig. 1B scheme.

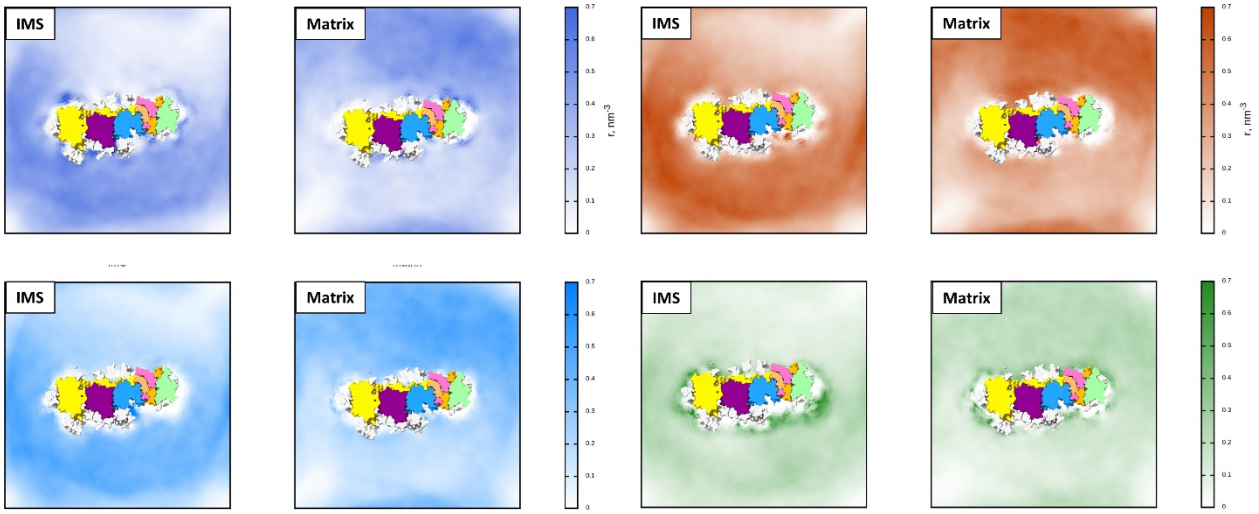

Fig. S34. Average RMSF *vs.* residue number plots of the ND1 (top panels) and ND3 (bottom panels) subunits in the human systems.
Left and right panels report the results for the closed and open system, respectively. The average RMSF of the *wild type* subunits are in red, while the single and the triple mutants are in blue and green, respectively. The width of the shading shows the standard deviation calculated on the three replicas of each simulation. The position of the TMHs is reported above the plots.

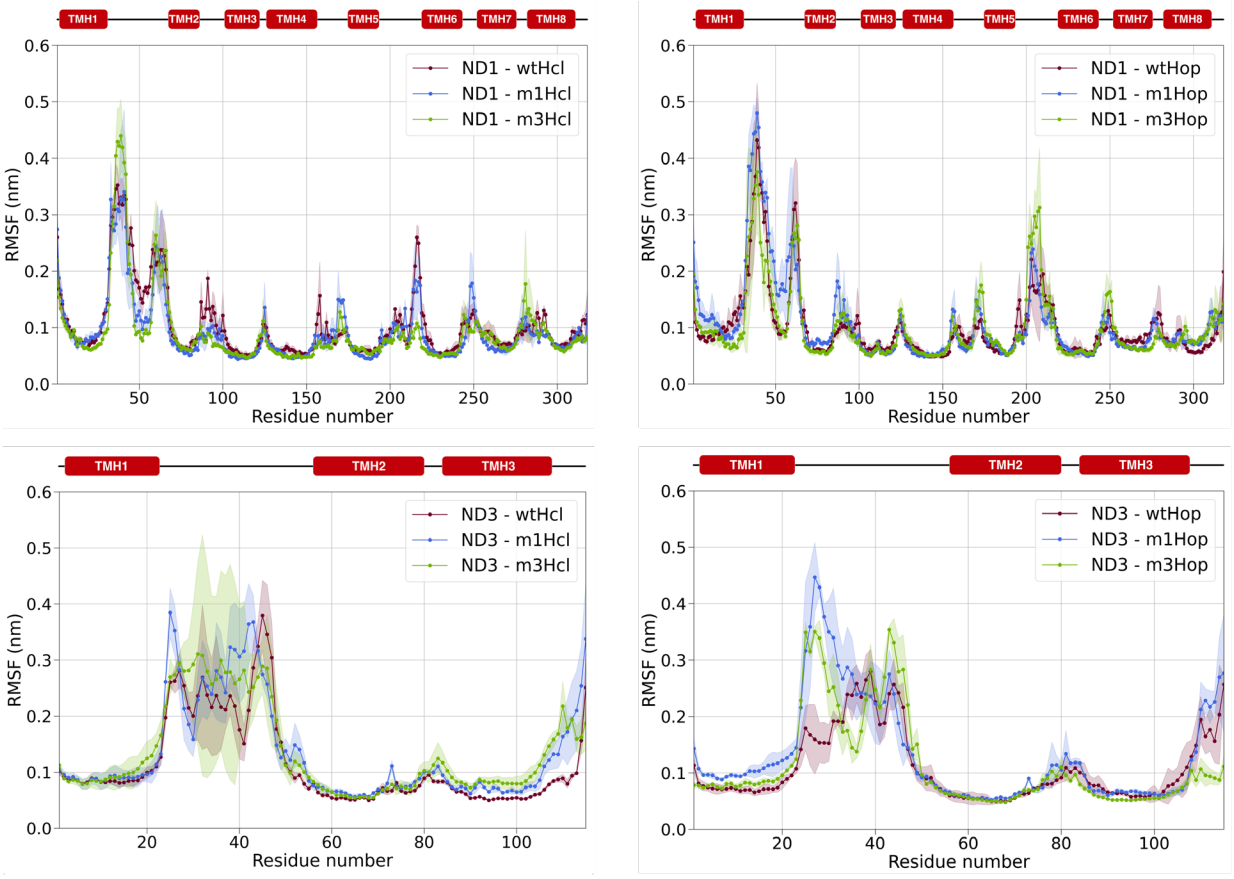

Fig. S35. Average RMSF *vs.* residue number plots of the ND2 (top panels) and ND4 (bottom panels) subunits in the human systems.
Left and right panels report the results for the closed and open system, respectively. The average RMSF of the *wild type* subunits are in red, while the single and the triple mutants are in blue and green, respectively. The width of the shading shows the standard deviation calculated on the three replicas of each simulation. The position of the TMHs is reported above the plots.

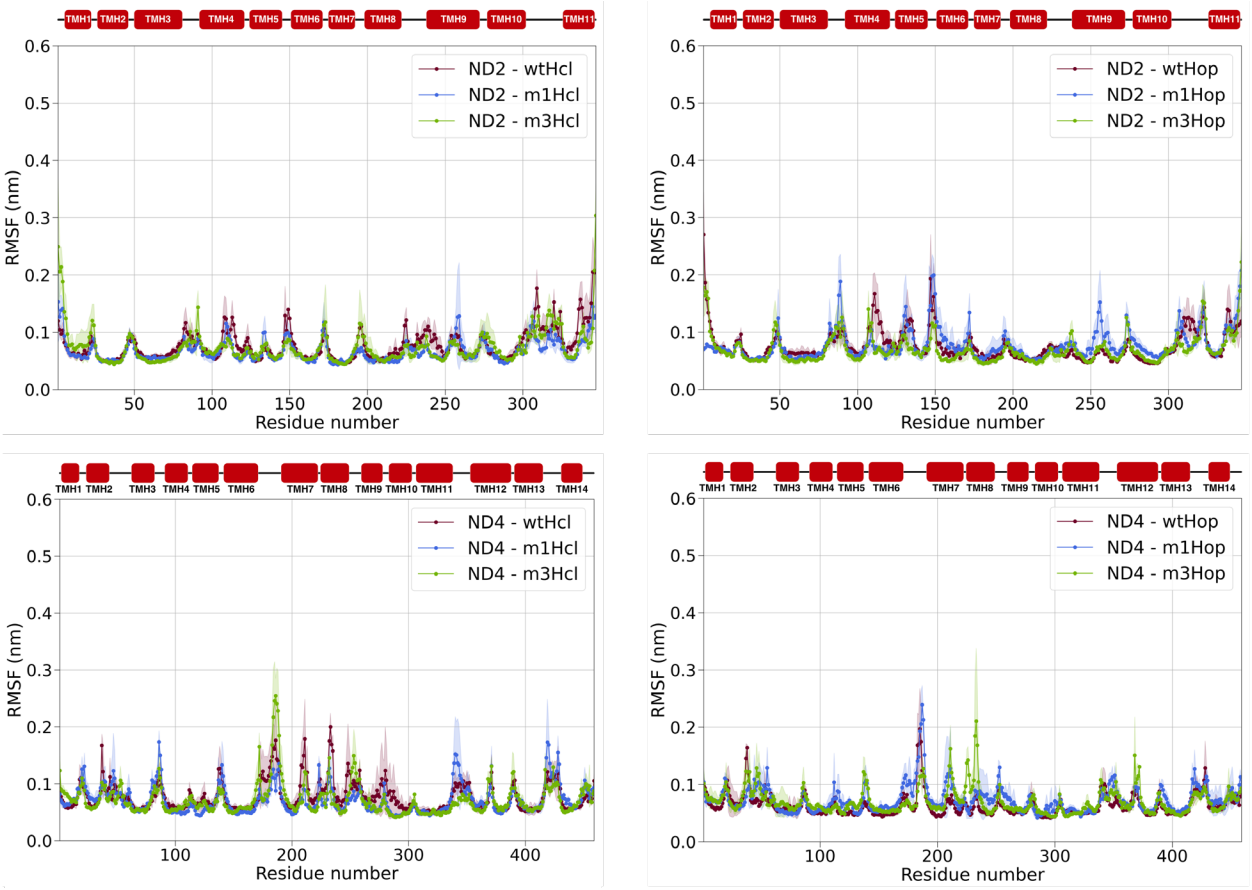

Fig. S36. Average root mean square fluctuations values as a function of the residue number for ND4L in the human closed and open conformation, respectively.
The *wild type* ND4L is in red, while the single and the triple mutants are in blue and green, respectively. The width of the shading shows the standard deviation calculated on the three replicas of each simulation. The mutation position is indicated by a black arrow, while the secondary structure is reported above the plots. The right panels report a close up of the average RMSF in the region around the p.A71T/ND4L variant, which includes the TMH3 and the nearby loops, for the human closed and open systems, respectively.

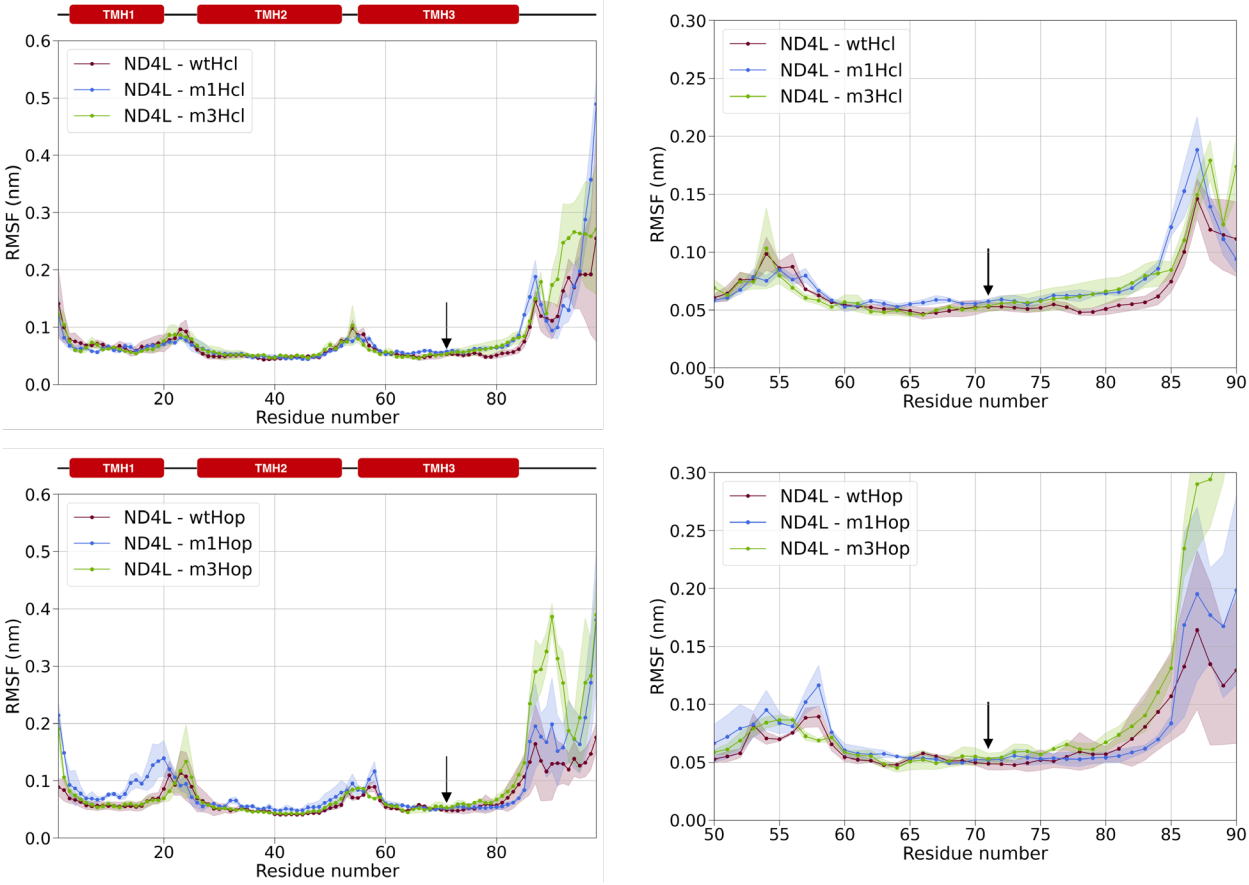

Fig. S37. Average root mean square fluctuations values as a function of the residue number for ND5 in the human closed and open conformation, respectively.
The *wild type* ND5 is in red, while the single and the triple mutants are in blue and green, respectively. The width of the shading shows the standard deviation calculated on the three replicas of each simulation. The mutation position is indicated by a black arrow, while the position of the TMHs is reported above the plots. The right panels report a detail of the average RMSF in the region around the p.T536A/ND5 mutation, which includes the lateral helix (HL) and the nearby loops, for the human closed and open systems, respectively.

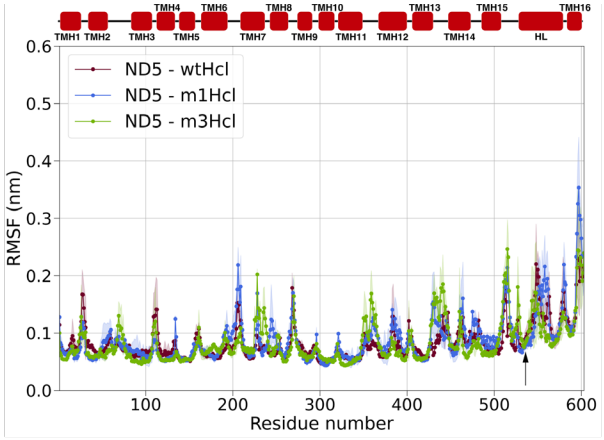

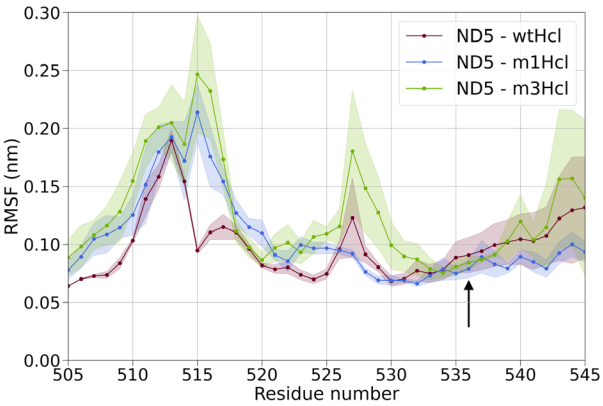

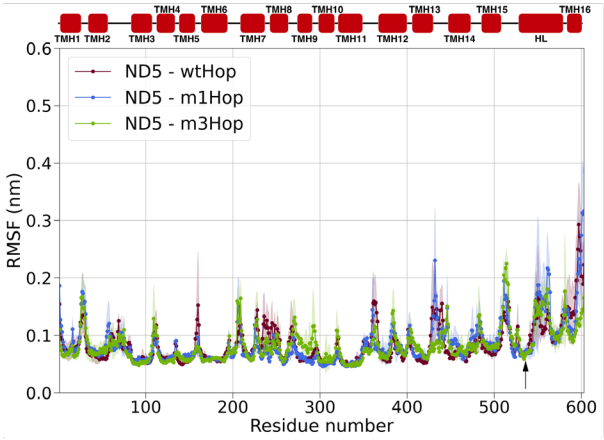

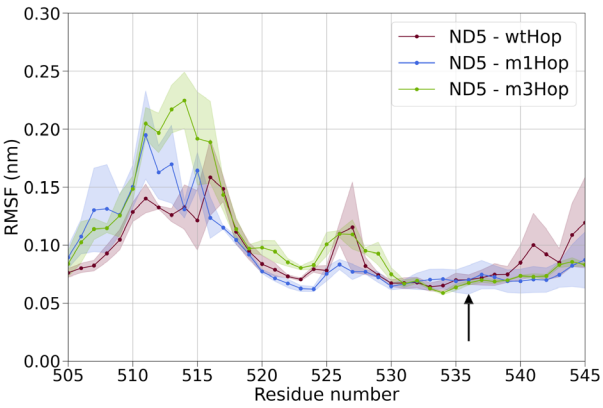

Fig. S38. Average RMSF *vs.* residue number plots of the ND1 (top panels) and ND3 (bottom panels) subunits in the ovine systems.
Left and right panels report the results for the closed and open system, respectively. The average RMSF of the *wild type* subunits are in prange. The width of the shading shows the standard deviation calculated on the three replicas of each simulation. The position of the TMHs is reported above the plots.

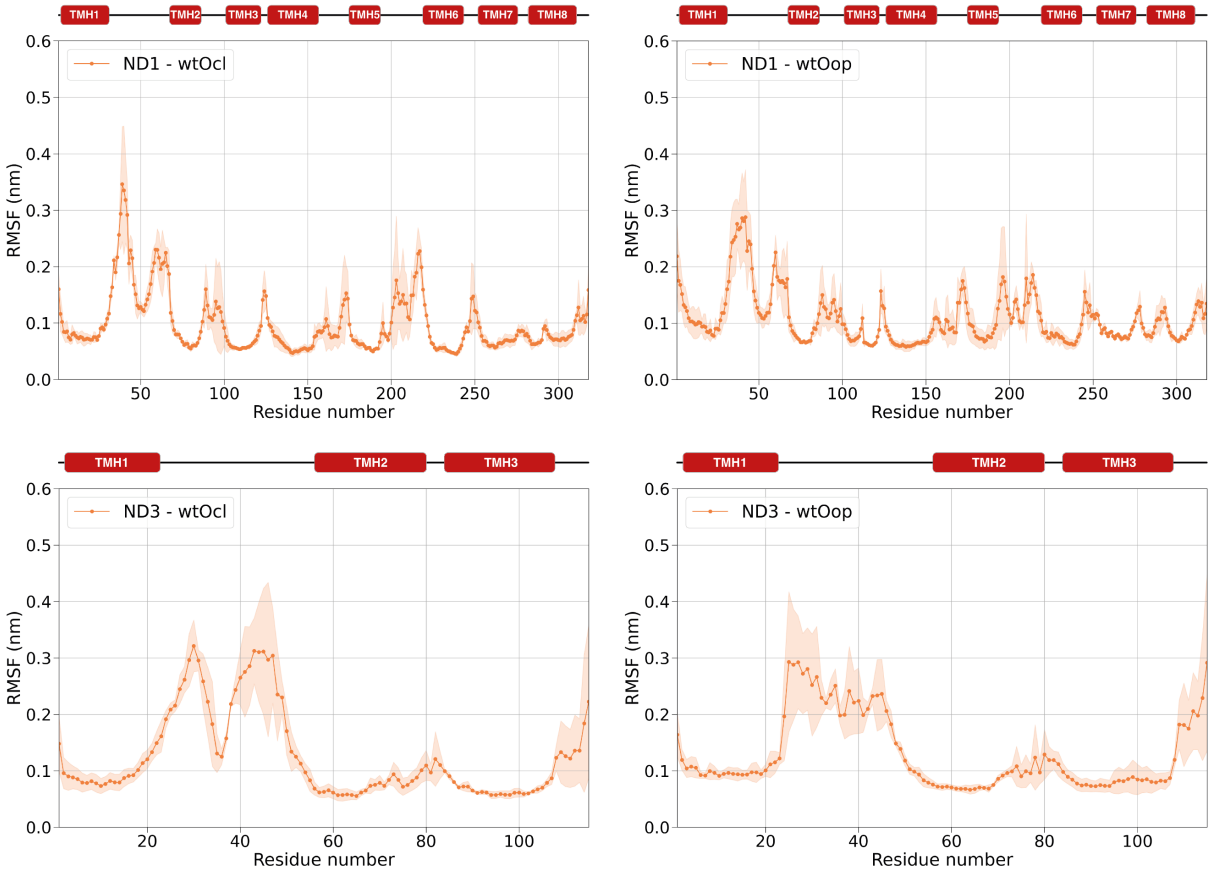

Fig. S39. Average RMSF *vs.* residue number plots of the ND2 (top panels) and ND4 (bottom panels) subunits in the ovine systems.
Left and right panels report the results for the closed and open system, respectively. The average RMSF of the *wild type* subunits are in orange. The width of the shading shows the standard deviation calculated on the three replicas of each simulation. The position of the TMHs is reported above the plots.

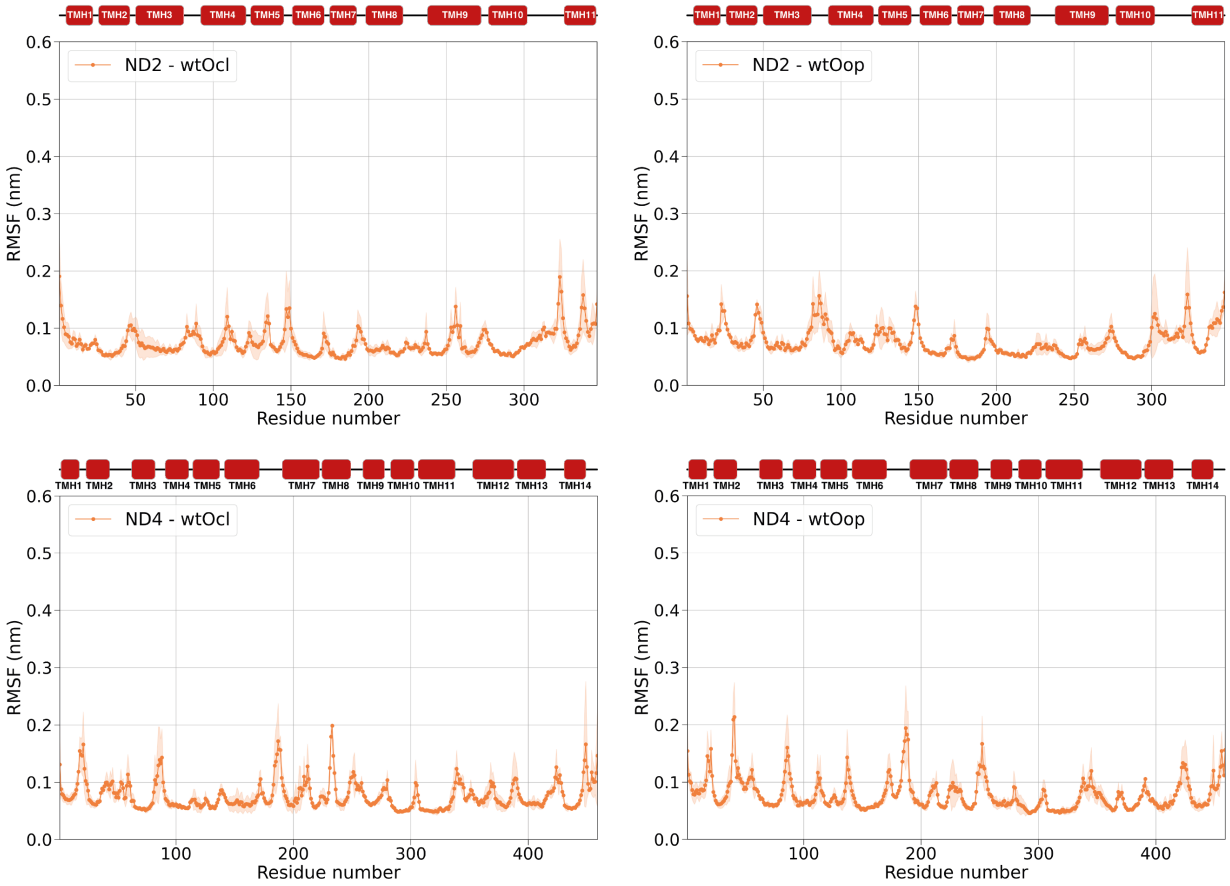

Fig. S40. Average root mean square fluctuations values as a function of the residue number for the ND6 (top panels), ND4L (middle panels) and ND5 (bottom panels) in the ovine closed (left panels) and open (right panels) conformation, respectively.
The average RMSF of the *wild type* subunits are in orange. The width of the shading shows the standard deviation calculated on the three replicas of each simulation. The positions of the mutated residues in the human subunits are indicated by a black arrow, while the position of the TMHs is reported above the plots.

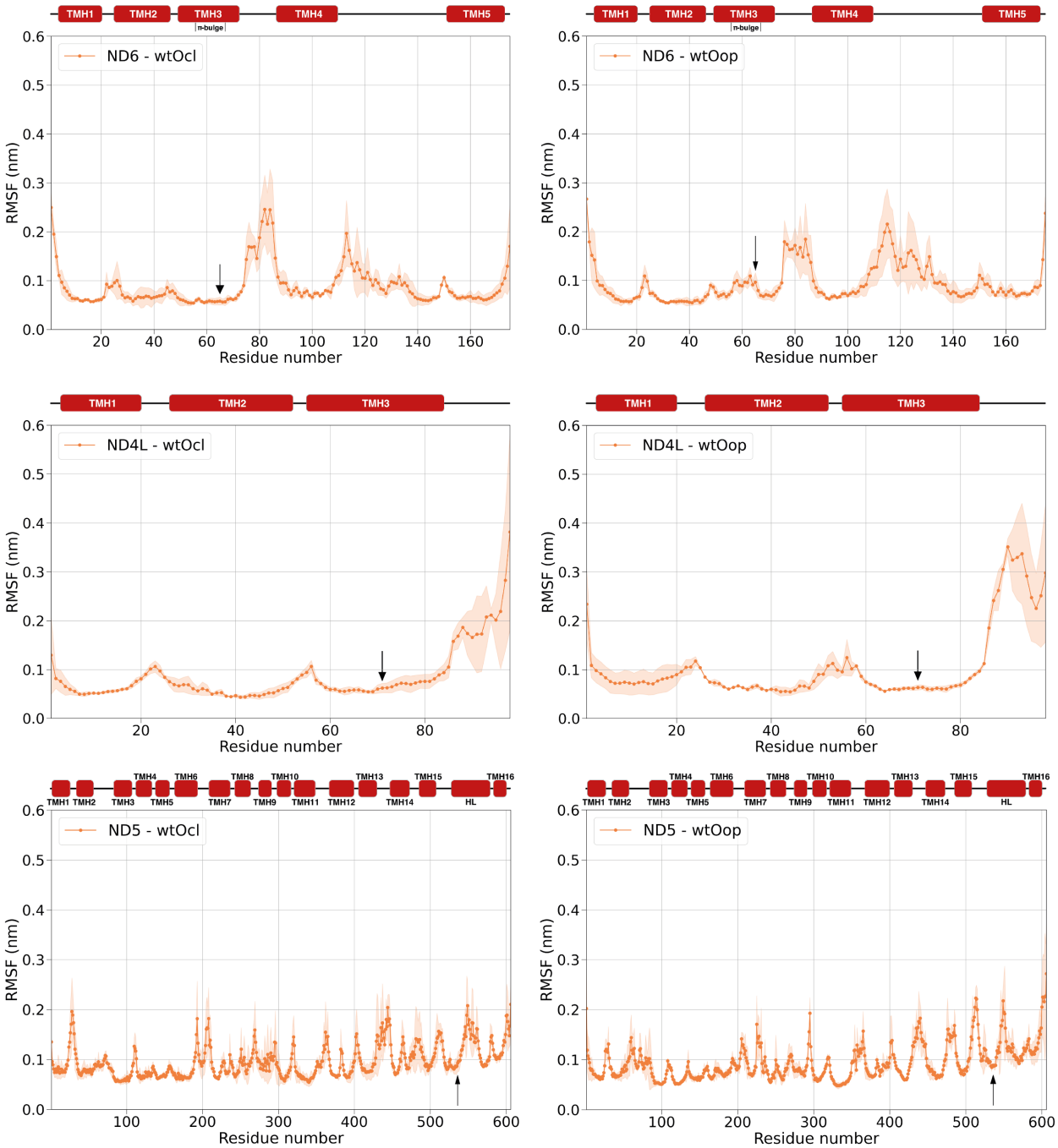

Fig. S41. Residues within 0.6 nm of p.T536A/ND5.
Simulations conducted from the *wild type*, single mutant and triple mutant systems are in red, blue and green bars, respectively. The height of the bars is proportional to the fraction of simulation time. The upper and bottom panels refer to the simulations conducted starting from the closed and the open conformation, respectively. The six nearest residues to p.T536A/ND5 in the ND5 aminoacidic sequence were excluded from the analysis.

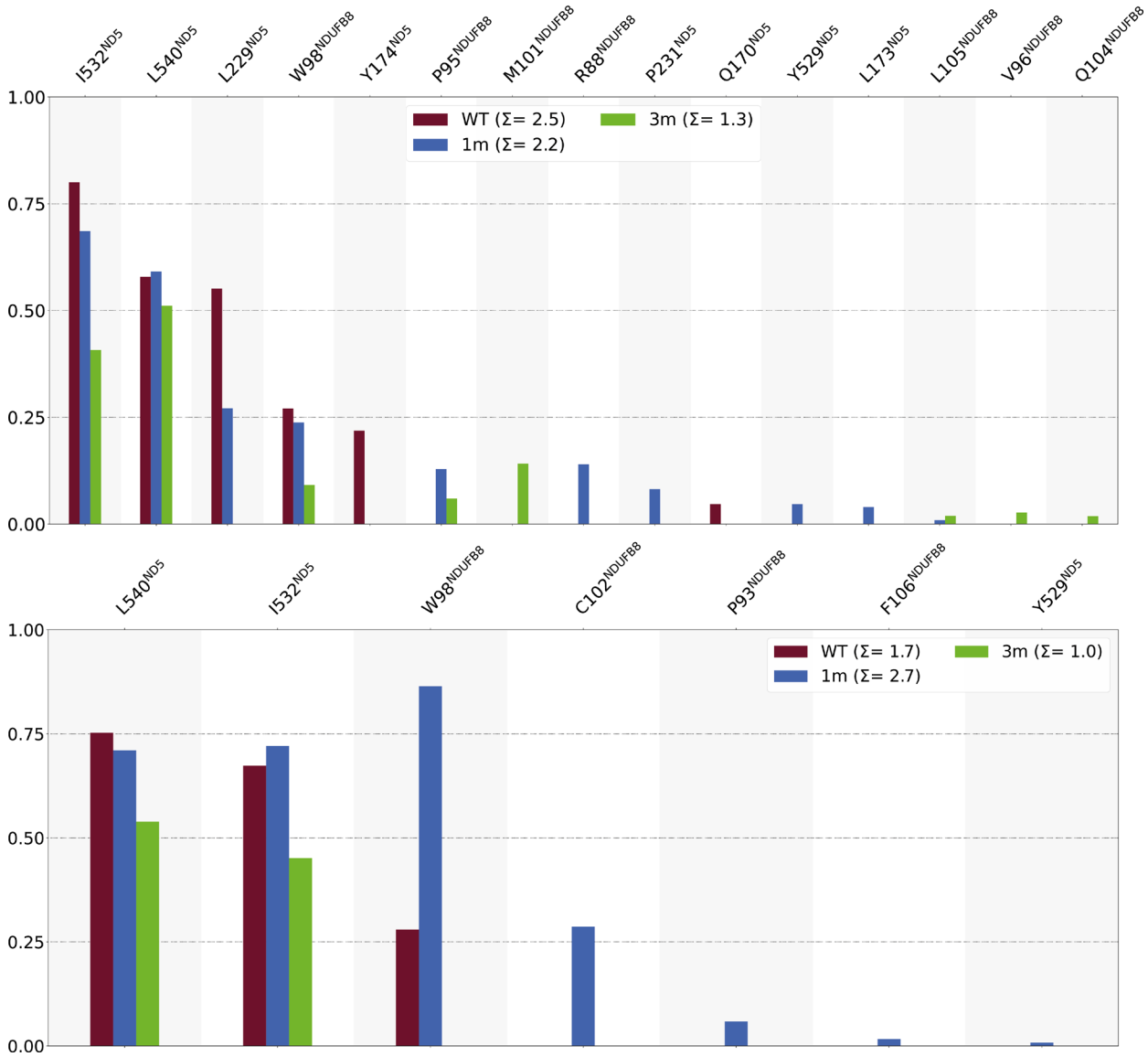

Figure S42. Cluster analysis performed on the ND6 subunit in the closed conformation. The results of cluster analysis performed on wtO^{cl} (**A**), wtH^{cl} (**B**), m1H^{cl} (**C**), and m3H^{cl} (**D**) trajectories are shown. In each panel, the bar plot of the relative cluster population of the first ten clusters is shown at the top, while the superposition of the ND6 backbone of the first ten cluster representative structures is shown at the bottom. In each panel, the ND6 subunit has been colored from blue to red from the N- to the C-terminus, and the position of the TMHs has been indicated. The position of ND6 M64 (M65 in the ovine sequence numbering) in each cluster representative is highlighted with a green sphere.

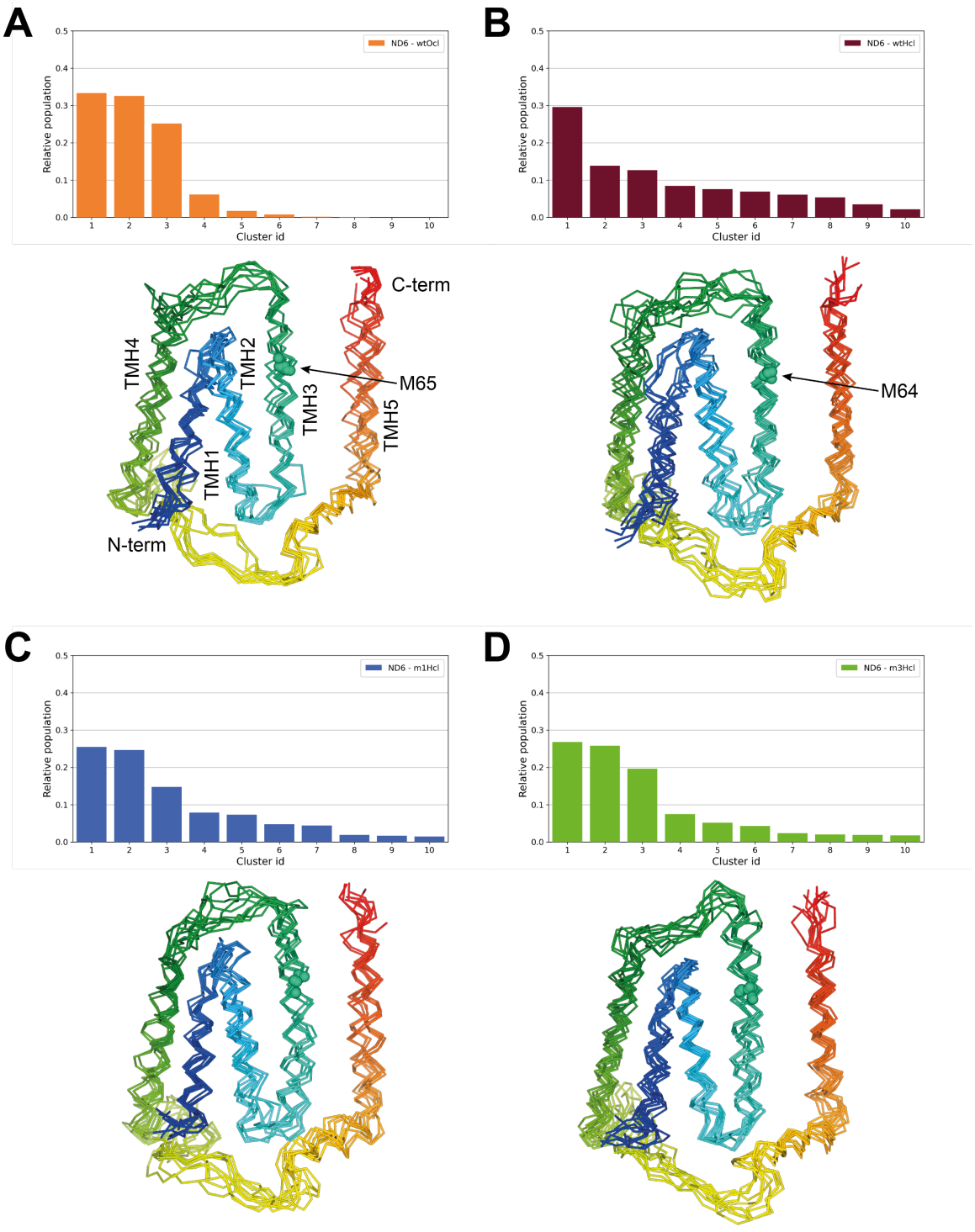

Fig. S43. Cluster analysis performed on the ND6 subunit in the open conformation. The results of cluster analysis performed on wtO^{op} (**A**), wtH^{op} (**B**), m1H^{op} (**C**), and m3H^{op} (**D**) trajectories are shown. In each panel, the bar plot of the relative cluster population of the first ten clusters is shown at the top, while the superposition of the ND6 backbone of the first ten cluster representative structures is shown at the bottom. In each panel, the ND6 subunit has been colored from blue to red from the N- to the C-terminus, and the position of the TMHs has been indicated. The position of ND6 M64 (M65 in the ovine sequence numbering) in each cluster representative is highlighted with a green sphere.

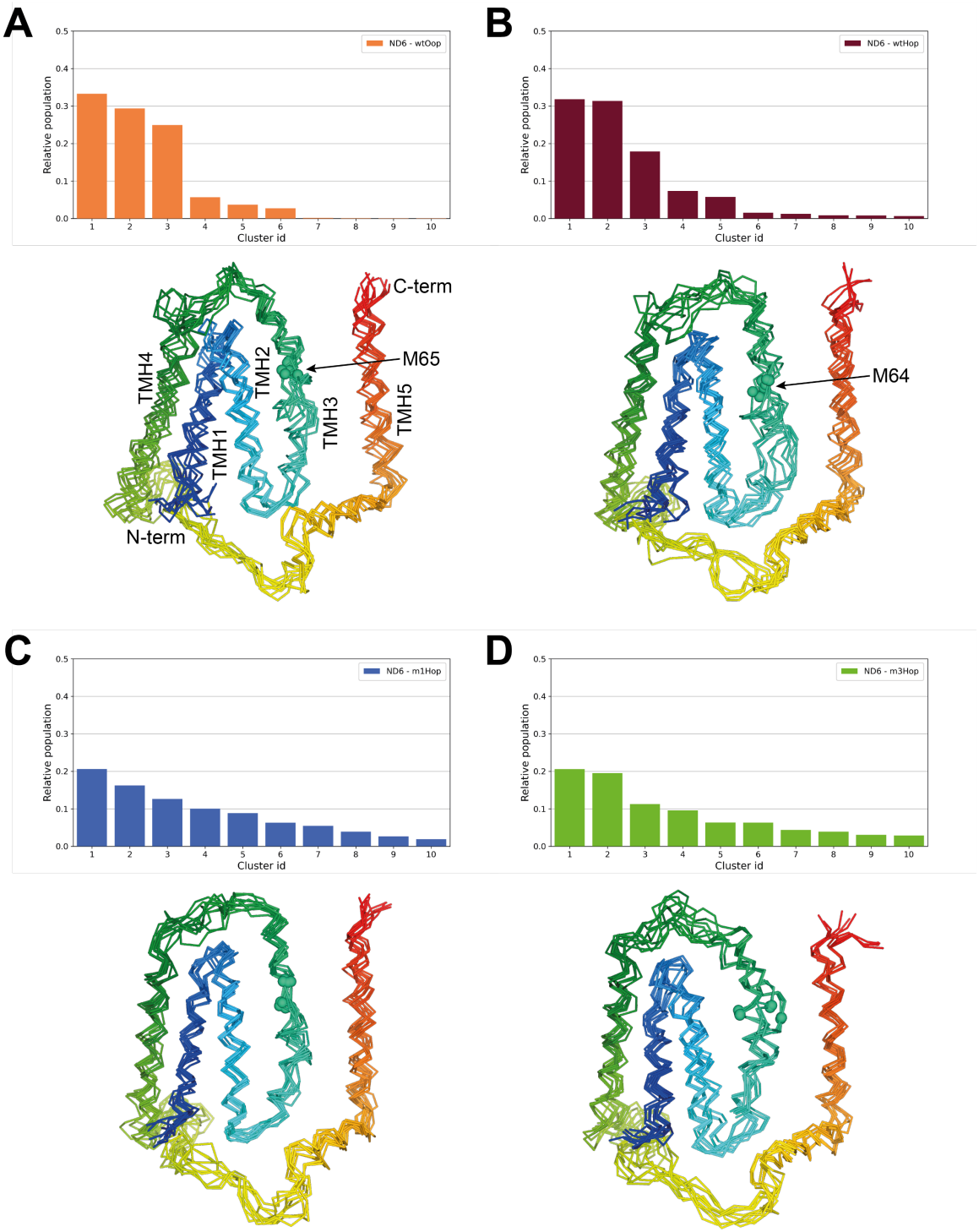

Fig. S44. Projections along the first three principal modes obtained from the combined essential dynamics analysis performed on the time evolving BB distance matrix.
Panels **A** and **B** refer to the open and closed systems respectively. The *wild type* projections are in red, while the single and the triple mutants are in blue and green, respectively.

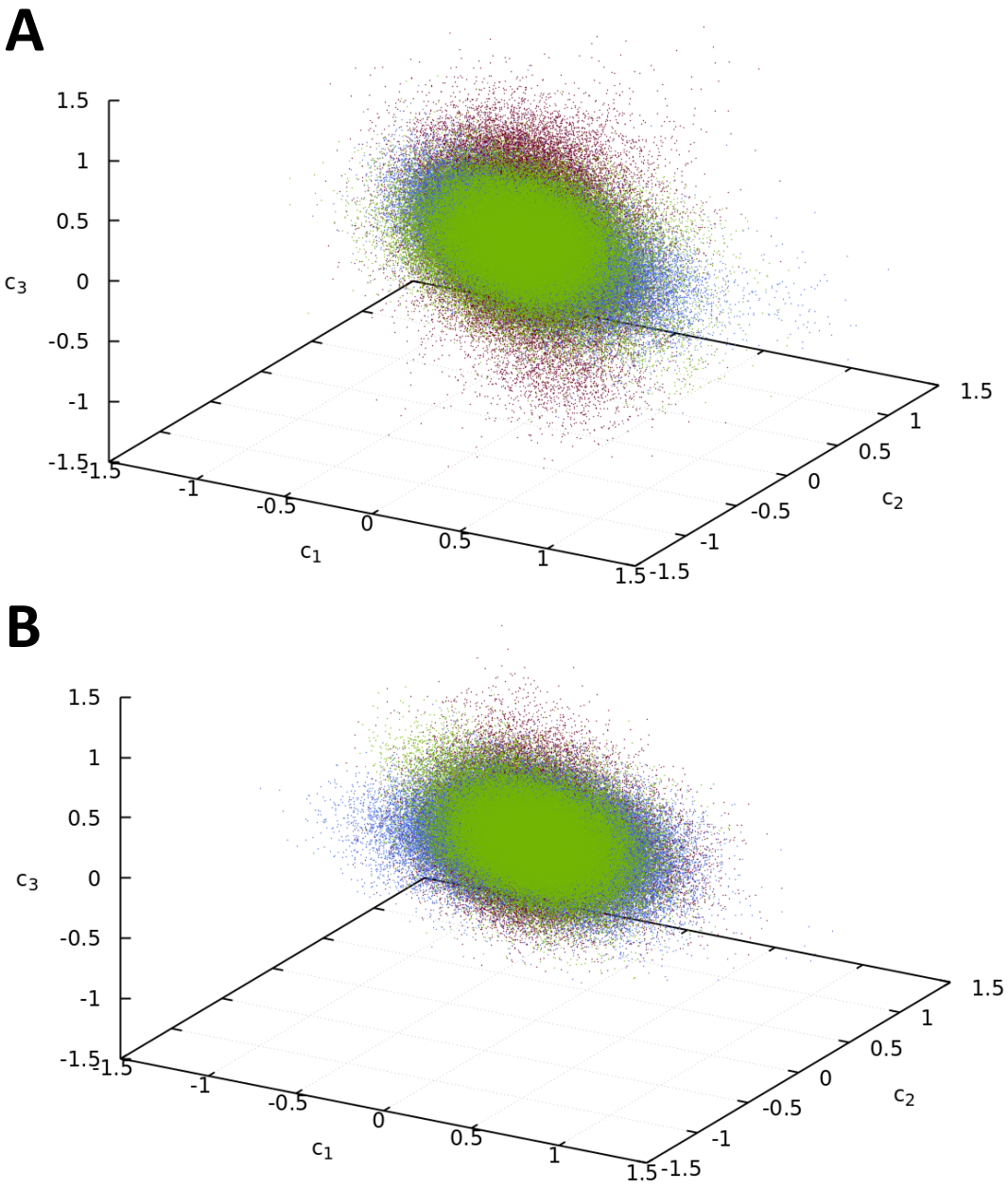

Fig. S45. Analysis of the BB dihedrals in the TMH3/ND6 π-bulge region.
Distribution of the backbone dihedral angles observed throughout the simulations in the closed systems. The *wild type* is in red, while the single and triple mutants are in blue and green.

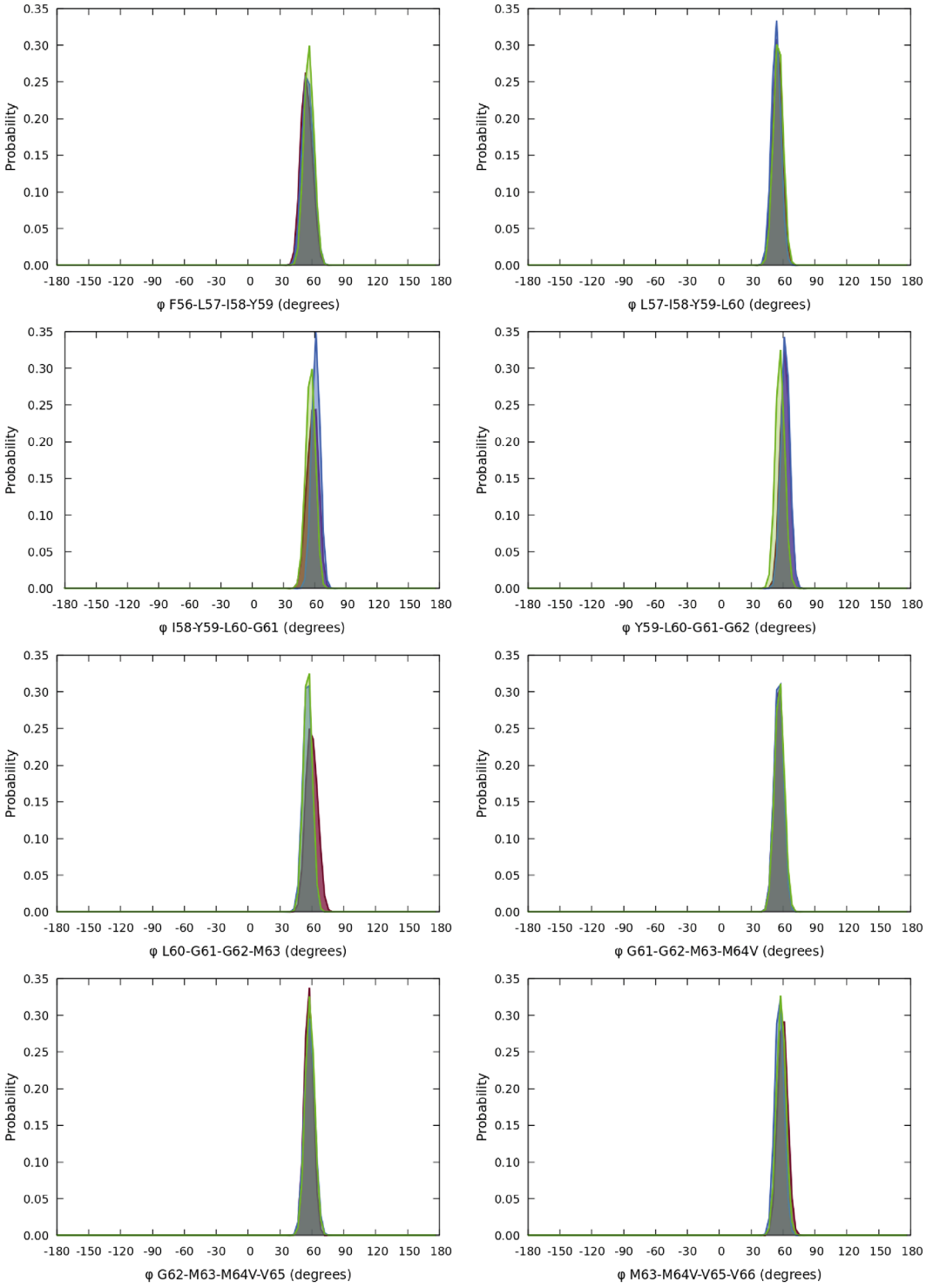

Fig. S46. Analysis of the BB dihedrals in the TMH3/ND6 π-bulge region.
Distribution of the backbone dihedral angles observed throughout the simulations in the first replica of wtH^{op} system (brown dots). The Gaussian curves used to fit the dihedral angles distribution and the sum of the fitting Gaussians are in red.

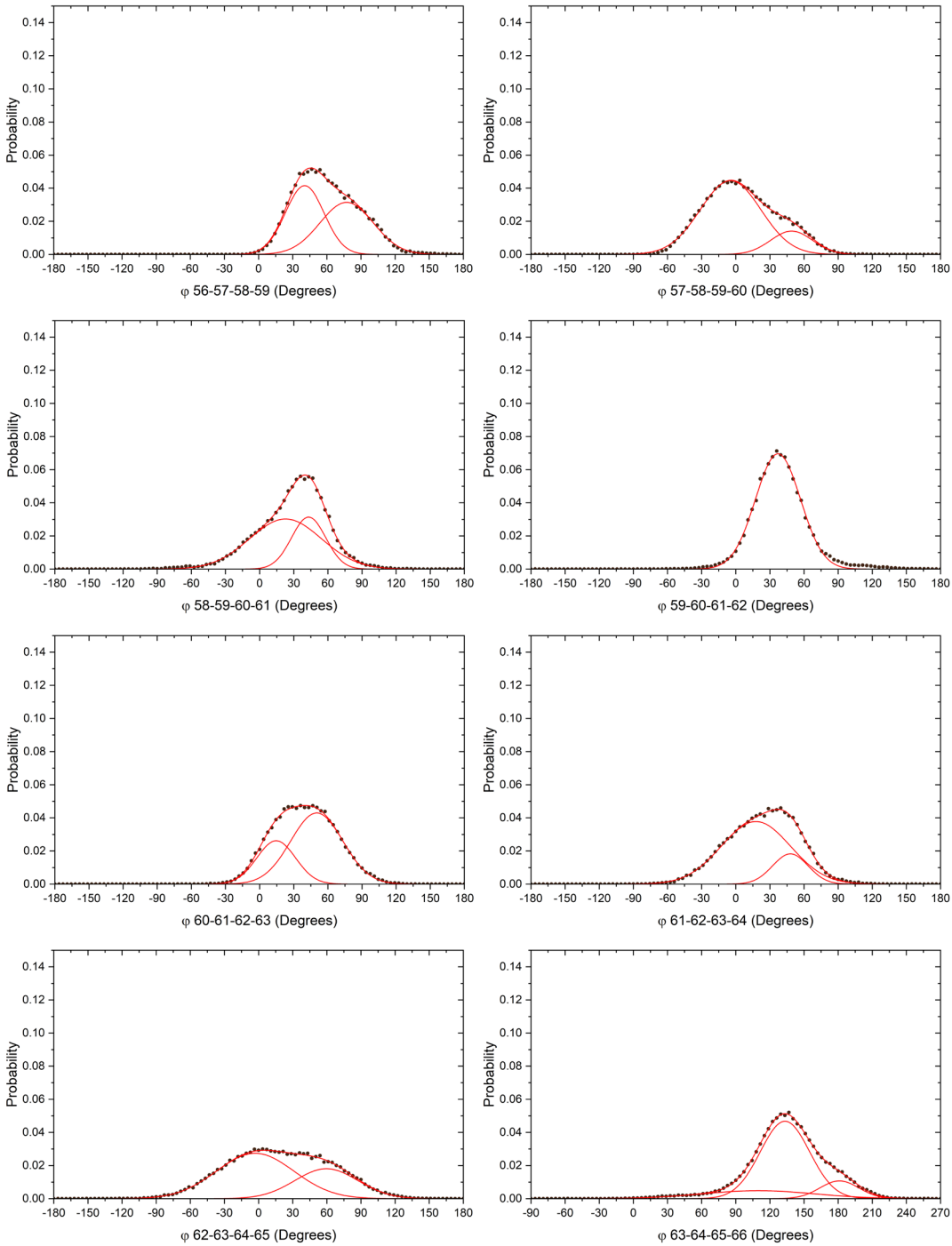

Fig. S47. Analysis of the BB dihedrals in the TMH3/ND6 π-bulge region.
Distribution of the backbone dihedral angles observed throughout the simulations in the second replica of wtH^{op} system (maroon dots). The Gaussian curves used to fit the dihedral angles distribution and the sum of the fitting Gaussians are in red.

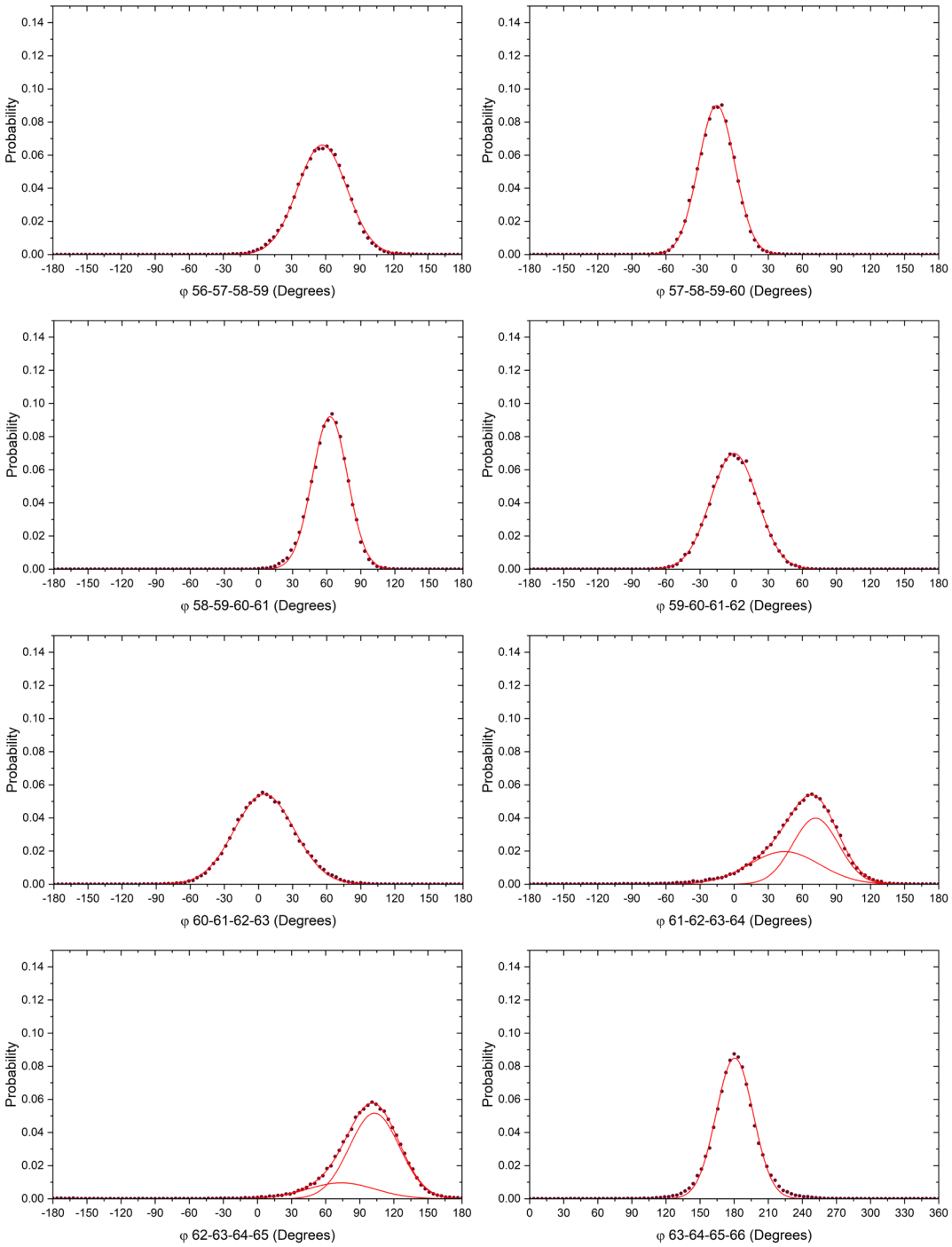

Fig. S48. Analysis of the BB dihedrals in the TMH3/ND6 π-bulge region.
Distribution of the backbone dihedral angles observed throughout the simulations in the third replica of wtH^{op} system (crimson dots). The Gaussian curves used to fit the dihedral angles distribution and the sum of the fitting Gaussians are in red.

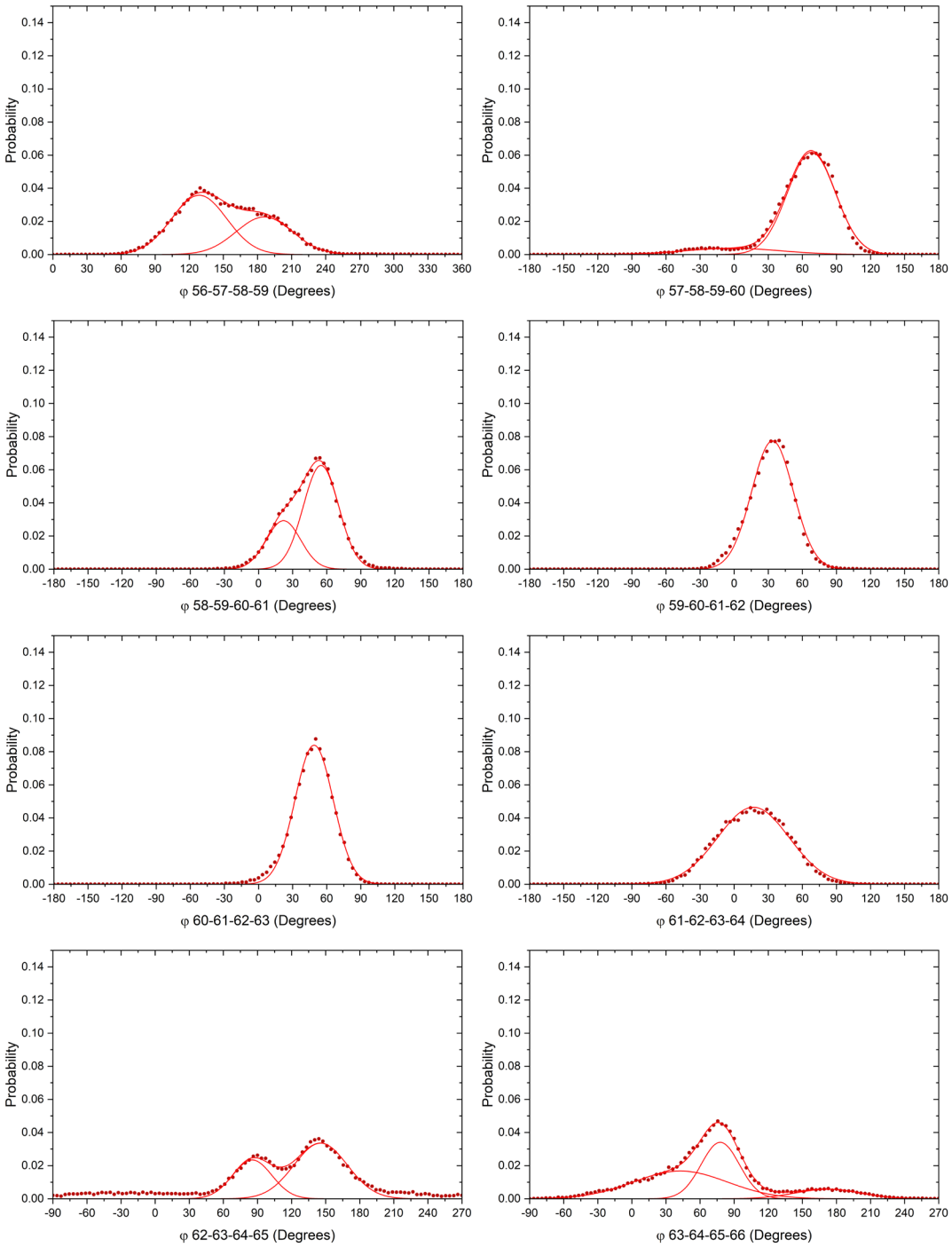

Fig. S49. Analysis of the BB dihedrals in the TMH3/ND6 π-bulge region.
Distribution of the backbone dihedral angles observed throughout the simulations in the first replica of m1H^{op} system (navy dots). The Gaussian curves used to fit the dihedral angles distribution and the sum of the fitting Gaussians are in red.

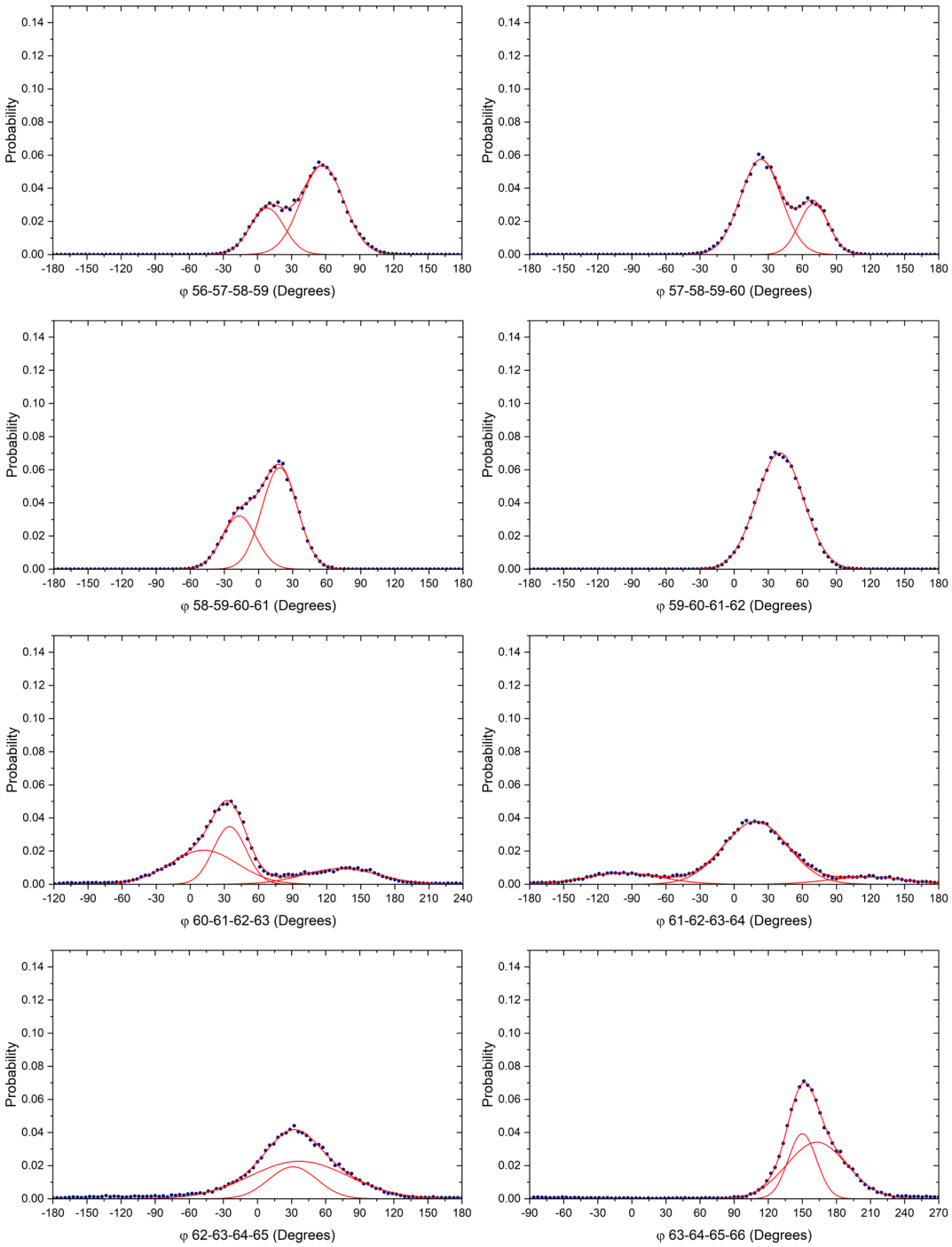

Fig. S50. Analysis of the BB dihedrals in the TMH3/ND6 π-bulge region.
Distribution of the backbone dihedral angles observed throughout the simulations in the second replica of m1H^{op} system (royal blue dots). The Gaussian curves used to fit the dihedral angles distribution and the sum of the fitting Gaussians are in red.

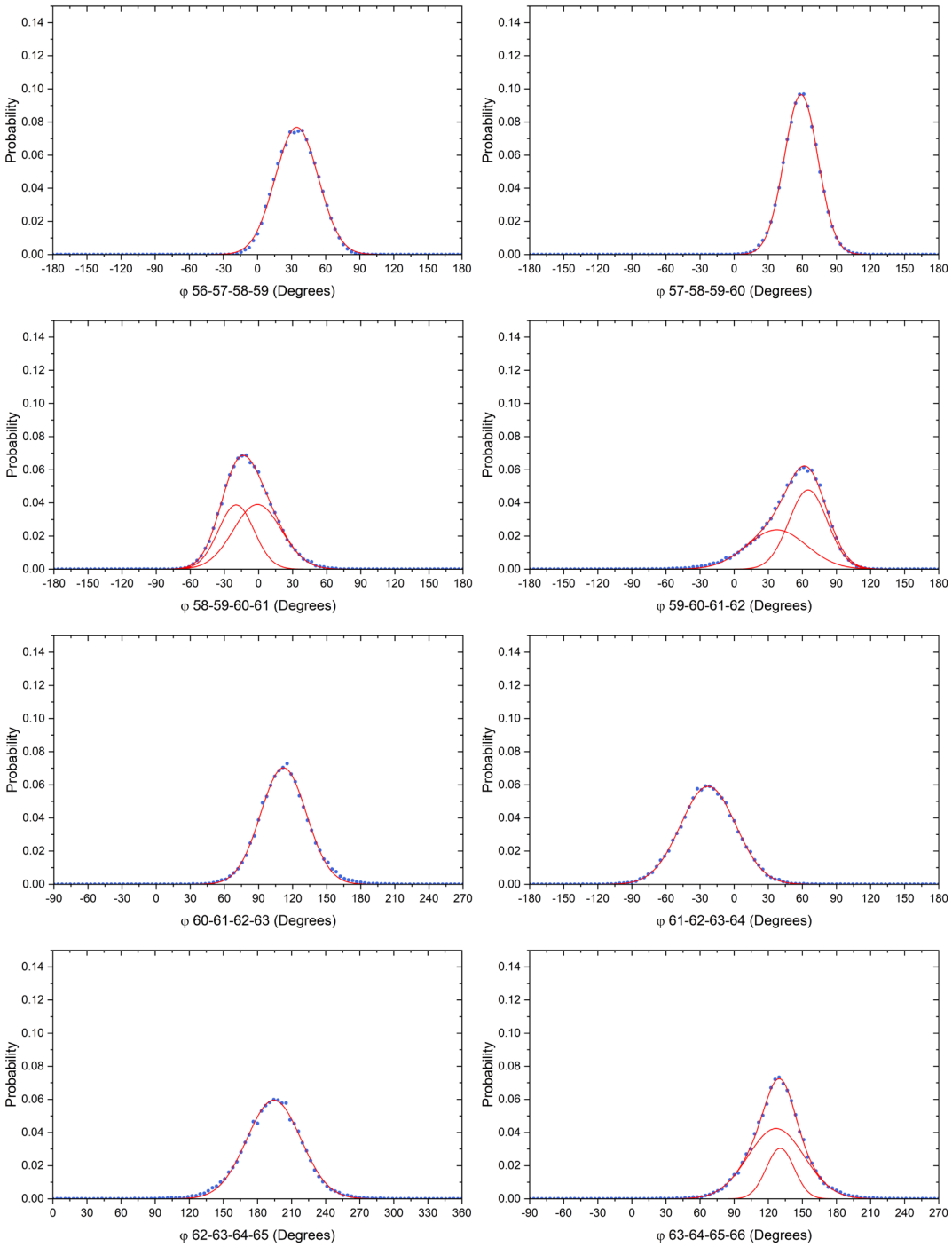

Fig. S51. Analysis of the BB dihedrals in the TMH3/ND6 π-bulge region.
Distribution of the backbone dihedral angles observed throughout the simulations in the third replica of m1H^{op} system (fountain blue dots). The Gaussian curves used to fit the dihedral angles distribution and the sum of the fitting Gaussians are in red.

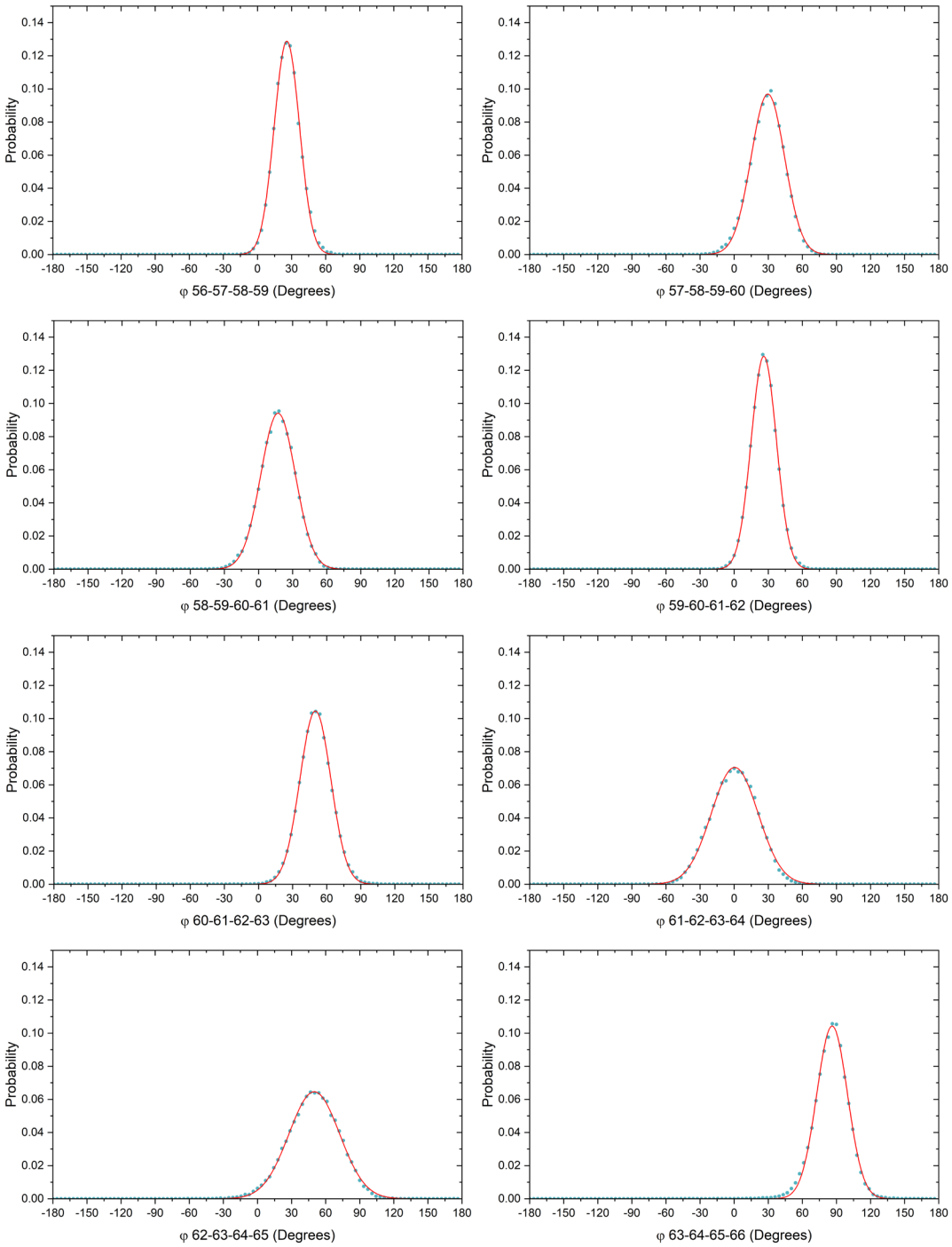

Fig. S52. Analysis of the BB dihedrals in the TMH3/ND6 π-bulge region.
Distribution of the backbone dihedral angles observed throughout the simulations in the first replica of m3H^{op} system (pine dots). The Gaussian curves used to fit the dihedral angles distribution and the sum of the fitting Gaussians are in red.

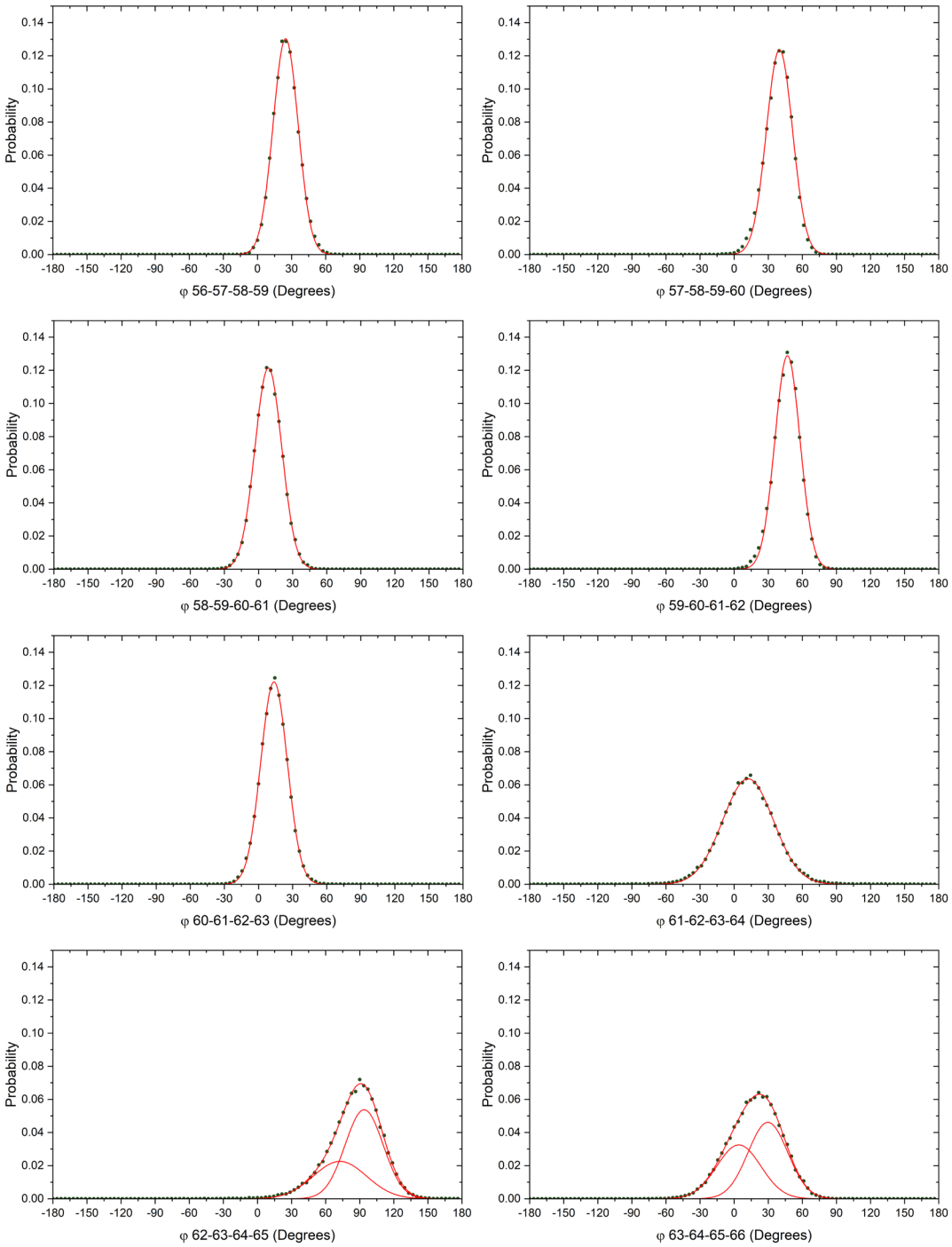

Fig. S53. Analysis of the BB dihedrals in the TMH3/ND6 π-bulge region.
Distribution of the backbone dihedral angles observed throughout the simulations in the second replica of m3H^{op} system (dark lime dots). The Gaussian curves used to fit the dihedral angles distribution and the sum of the fitting Gaussians are in red.

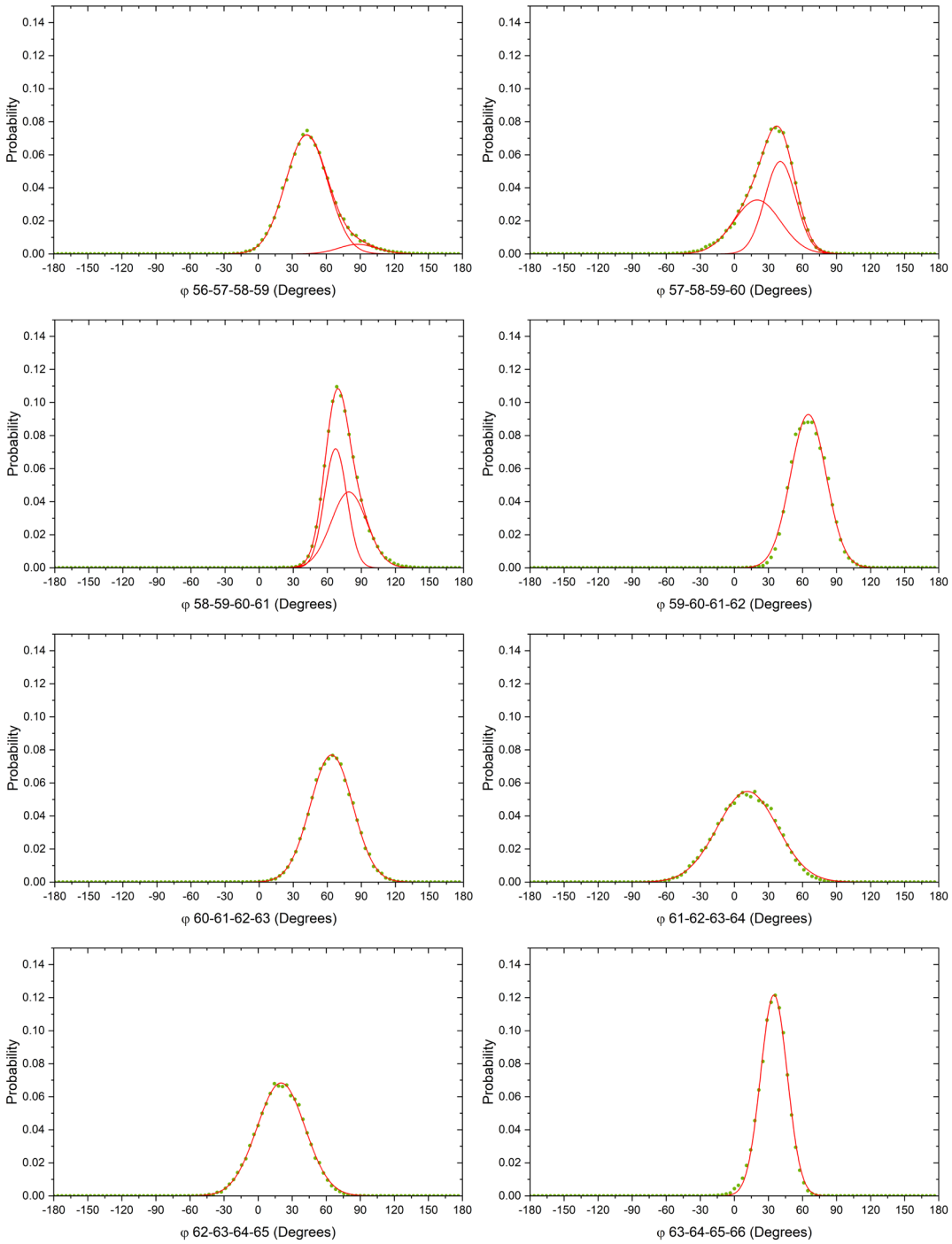

Fig. S54. Analysis of the BB dihedrals in the TMH3/ND6 π-bulge region.
Distribution of the backbone dihedral angles observed throughout the simulations in the third replica of m3H^{op} system (lime dots). The Gaussian curves used to fit the dihedral angles distribution and the sum of the fitting Gaussians are in red.

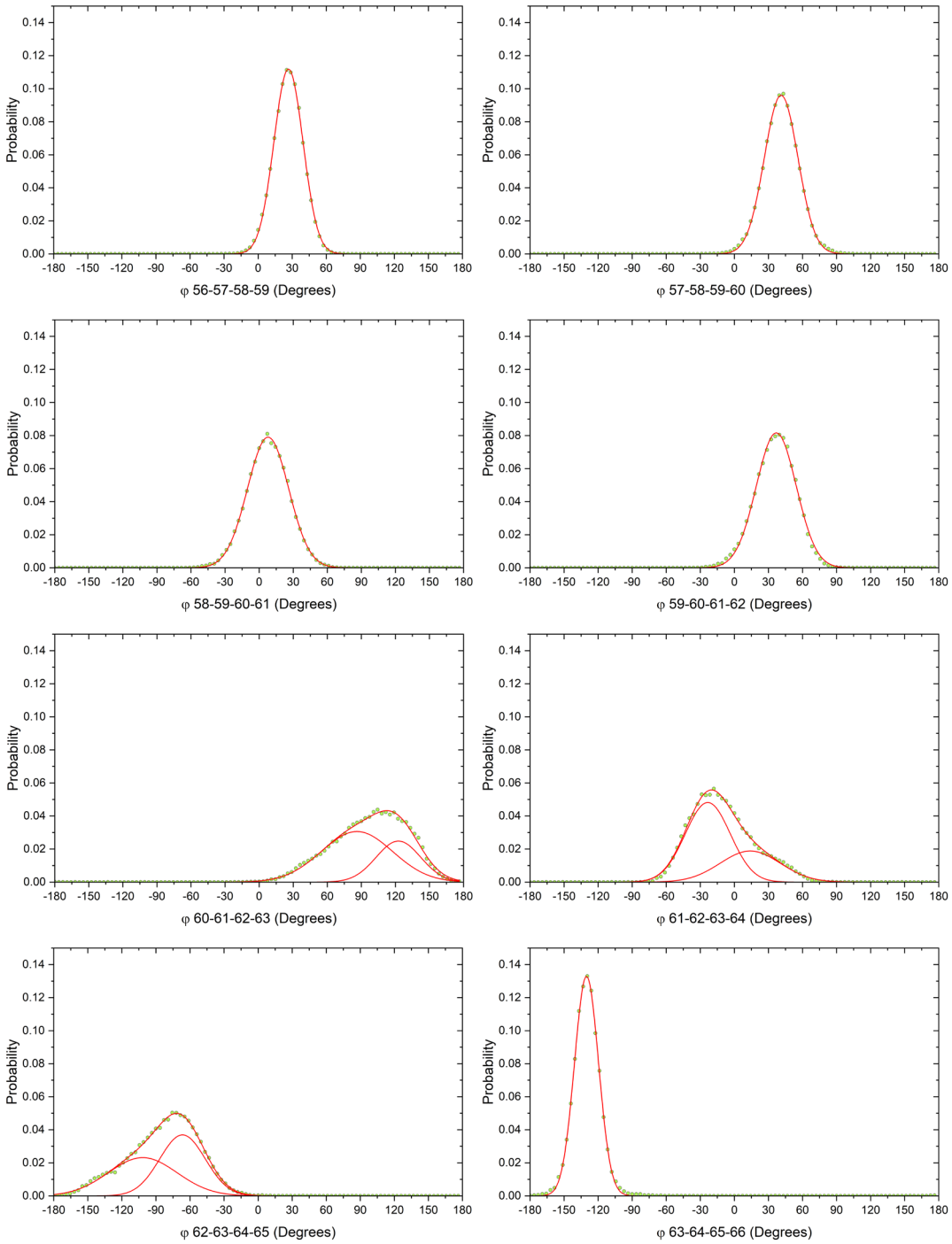

Supplementary Methods

Reconstruction of unsolved regions in ovine P+ module structures. The unsolved regions in the selected structures were reconstructed by using Modeller 10.0 [4] and generating 100 models for each system. The ovine CI structures in both open (PDB id 6ZKE) [5] and closed conformation (PDB id 6ZKC) [5] were chosen as template for the missing regions. Table S2 offers a list of the modelled regions in both systems. For each system, the best model was selected on the basis of the DOPE potential [6] included in Modeller and was subsequently analyzed using ProCheck [1]. A loop optimization procedure comprising the generation of 500 models for each system was then applied using Modeller to correct structurally problematic regions. Analysis of the models done with ProCheck [1] and Prosa [2, 3] (Table S4) showed that the models were of comparable quality with the starting experimental structures. Unlike the other P+ module subunits, the 49 kDa subunit is largely modelled and is not in its physiological environment. Consequently, the behavior of this subunit is not considered in this study.

Combined Essential Dynamics on the time evolving BB distance matrix. The procedure applied here is the one proposed by Berendsen and co-worker in 1995 [7] and recently described by Palma and Pierdominici-Sottile [8], also known as "Combined Essential Dynamics".

A total trajectory is created by concatenating *n = 9* individual simulations of distance matrix network: 3 runs for the *wild type* + 3 runs for the single mutant + 3 runs for the triple mutant, for a total of 270,000 points and 820 observables (pairwise distances between backbone beads, BB). The covariance matrix of the concatenated trajectory is given by the average of $n = 9$ individual covariance matrices plus the covariance matrix of the individual average structure, as follows:

$$\boldsymbol{C}^{(cn)} = \frac{1}{9}\sum_{k=1}^{9} \boldsymbol{C}^{(k)} + \boldsymbol{S}^{(cn)}$$

Where:

$$\boldsymbol{S}_{ij}^{(c9)} = \frac{1}{9}\sum_{k=1}^{9} \left(\langle x\rangle_i^{(k)} - \langle x\rangle_i^{(c9)}\right)\left(\langle x\rangle_j^{(k)} - \langle x\rangle_j^{(c9)}\right)$$

Here x_i is the i^{th} distance between a couple of BB beads.
The total covariance matrix is then diagonalized in order to get:

$$\boldsymbol{C}^{(cn)}\boldsymbol{v}_i = \lambda_i \boldsymbol{v}_i$$

for i = 1,820, where $\boldsymbol{v}_i$ is the i^{th} eigenvector and λ_i is the i^{th} eigenvalue.
The projections along the first three eigenvectors are calculated as follows:

$$c_i(t) = x_i(t) \times \boldsymbol{v}_i, i = 1{,}3$$

The first three projections account for more of the 60% of the total variance.
The time-lagged system variance can be calculated as:

$$variance(\tau) = \langle |c_i(t+\tau) - c_i(t)| \rangle$$

Contact matrix frequency. The side-chains distance matrix is defined as $\boldsymbol{D} = [d_{ij}]$, where ij are the element of the matrix is the distance d_{id} between the centers of the side-chain beads of residues i and j.
Contact matrix $\boldsymbol{C} = [c_{ij}]$, with elements c_{ij} defined as:

$c_{ij} = 1$ if $d_{ij} \leq d_{cut-off}$
$c_{ij} = 0$ if $d_{ij} > d_{cut-off}$

Here $d_{cut-off}$ is the cut-off distance defining residue being in contact. Here $d_{cut-off}$ was set equal to 0.6 nm, representing the distance between side-chains center of mass.

Water analysis. For the analysis for the putative water insertion in the ND6 TMH3 π-bulge region a tool based on the python package MDAnalysis [9] was used. The analysis is based on approximating the space between the ND6 TMH3 and the adjacent helices in the ND3 and ND4L subunits with two cylinders of fixed diameter (0.8 and 1.0 nm, respectively). The procedure consists of four steps that are applied to each frame: *i*) the beads defining the channel and the principal axis of the channel are found; *ii*) the simulation box is rotated to align the principal axis of the channel with the z-axis of the reference system; *iii*) the "Center of Geometry" (COG) of the regions that are approximated by the two cylinders are found. Only backbone beads are included in the definition of the COG. Finally, *iv*) the water molecules are searched in the channel region, which is defined by two cylinders built using the *cyzone* function included in MDAnalysis. The first two steps are necessary because the *cyzone* function selects a cylindrical region with the axis parallel to the z-axis of the reference system. The result of this analysis is the number of water molecules in the channel at each frame and in all the studied systems only few water molecules stick to the external side of the cylinders, while no water molecules enter the channel.

Coarse-grained modelling of the mutated residues. To illustrate what is shown by the bar diagrams in Figs. 5 and 6, it is necessary to consider the structural differences between the *wild type* and mutated residues in the CG model [10, 11]. Mutate a methionine into a valine does not change the number and type of beads used to represent these residues. In fact, each residue is represented by a bead for the backbone and an apolar (C) bead for the side chain (Martini's bead type C5 and C2 for methionine and valine, respectively. The number highlights the polar affinity, specifically the C5 bead has a larger polar affinity than C2). C5 and C2 beads feature identical Lennard-Jones parameters but different inter-beads interaction parameters. In most of the cases, the C2 bead can form slightly less attractive inter-molecular interactions than C5. The only exception are the interactions with other C2 beads, for which C2 beads are more attractive than C5. Moreover, the distance between the BB and the side chain bead is different between the two residues (0.31 and 0.20 nm for methionine and valine, respectively). In contrast, concerning the p.A71T/ND4L mutation, the mutation of the alanine (represented by a backbone bead alone) with a threonine implies in the addition of a second polar-type bead to simulate the side chain.

Phosphopantetheine (ZMP) CG mapping. The ZMP molecule (S-[2-({N-[(2S)-2-hydroxy-3,3-dimethyl-4-(phosphonooxy)butanoyl]-beta-alanyl}amino)ethyl] tetradecanethioate) was parameterized according to Martini 2.2 procedure based on similarities with phosphatidylserine. First, the atomistic representation of ZMP was mapped into an 8-bead coarse-grained model to split the molecule into reasonable existing building blocks (Figure S55). Then, the Martini bead types were assigned based on the chemical building block they are taken to represent.

Figure S55. CG mappings of phosphopantetheine (ZMP).
CG spheres are shown over the atomistic structures of ZMP. The Martini beads are shown in different colors and type names are also given. The 'Nd' gray bead corresponds to the backbone bead of S44 of the acyl carrier subunit.

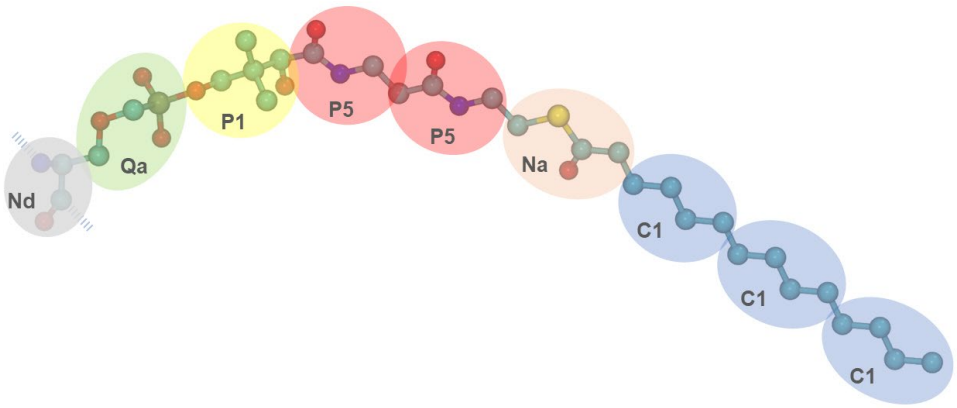

Table S7. Martini CG Parameters used for the phosphopantetheine prostetic group.

Bead type	Charge
Nd	0
Qa	-1
P1	0
P5	0
Na	0
C1	0

The equilibrium bond length (d) were all set to d = 0.47 nm, while the force constants (K_d) were set to K_d = 1250 kJ nm^{-2} mol^{-1}. Equilibrium angles (θ_{SSS}) and force constants (K_θ) were all set equal to θ_{SSS} = 180 degrees and K_θ = 25 kJ mol^{-1}, respectively.

Systems minimization and equilibration. The two energy minimization stages consisted of 5,000 steps of steepest descent without position restraints. The number of steps, the time steps and the force constants of the positional restraints used in the equilibration stages are resumed in Table S7. In all the equilibration stages the leap-frog algorithm was used. In the energy minimization and equilibration stages, periodic boundaries were applied to the systems and the electrostatic interactions were calculated through the Particles Mesh Ewald method [12]. The cut-off values for the real part of the electrostatic interactions and for the van der Waals interactions were set to 1.1 nm. The temperature and the pressure were regulated with the velocity-rescale thermostat [13] and the Berendsen barostat [14]. CG models yield a speed-up of 2-3 orders of magnitude relative to all-atom MD [15], which opens to the exploration of big size scales to microsecond time lengths. This is probably caused by the larger particle sizes, which generates a smoother energy landscape. The effective time sampled with MARTINI models is averagely 4-fold larger than the all-atoms models. Consequently, MARTINI simulated times are usually multiplied by the standard conversion factor of 4 [10] and all the analysis reported here have been already scaled.

Table S8. Parameters used in the five equilibration stages on each system.

Stage	Steps	Time step (fs)	Restraints force constants (J mol^{-1} nm^{-2}) on protein beads / on lipid heads
1	1,000,000	2	1000 / 200
2	500,000	5	500 / 100
3	250,000	10	250 / 50
4	125,000	20	100 / 50
5	125,000	20	20 / 10

Estimation of performance improvement with respect to other CI all-atom simulations. It is difficult to provide precise numerical indicators of the benefits of simulating CI at the CG level, because the authors of the all-atom MD simulations did not provide a performance metric. Röpke *et al.* [16] performed a total of 15 μs all-atom MD simulations on a system of 991,000 atoms, plus additional QM and QM/MM simulations on smaller CI portions using PRACE resources. Pereira *et al.* [17] performed a total of 360 ns of all-atom MD simulations on a system of about 862,000 atoms using the SDumont cluster at the LNCC (MCTI). In our simulations we used a relatively small number of computational resources provided by an ISCRA C grant for a total of 63,680 CPU hours. The performance of our CG MD simulations on the Marconi100 supercomputer was equivalent to 1.1 μs/day per replica. From these data, we can roughly estimate a performance improvement of about two orders of magnitude over similar all-atoms MD simulations.

SI References

[1] R.A. Laskowski, M.W. MacArthur, D.S. Moss, J.M. Thornton, PROCHECK: a program to check the stereochemical quality of protein structures, J. Appl. Cryst. 26(2) (1993) 283-291.
[2] M. Wiederstein, M.J. Sippl, ProSA-web: interactive web service for the recognition of errors in three-dimensional structures of proteins, Nucleic Acids Res 35(Web Server issue) (2007) W407-10.
[3] M.J. Sippl, Recognition of errors in three-dimensional structures of proteins, Proteins 17(4) (1993) 355-62.
[4] B. Webb, A. Sali, Comparative Protein Structure Modeling Using MODELLER, Curr Protoc Bioinformatics 54 (2016) 5.6.1-5.6.37.
[5] D. Kampjut, L.A. Sazanov, The coupling mechanism of mammalian respiratory complex I, Science 370(6516) (2020).
[6] M.Y. Shen, A. Sali, Statistical potential for assessment and prediction of protein structures, Protein Sci 15(11) (2006) 2507-24.
[7] D.M. van Aalten, A. Amadei, A.B. Linssen, V.G. Eijsink, G. Vriend, H.J. Berendsen, The essential dynamics of thermolysin: confirmation of the hinge-bending motion and comparison of simulations in vacuum and water, Proteins 22(1) (1995) 45-54.
[8] J. Palma, G. Pierdominici-Sottile, On the Uses of PCA to Characterise Molecular Dynamics Simulations of Biological Macromolecules: Basics and Tips for an Effective Use, Chemphyschem 24(2) (2023) e202200491.
[9] N. Michaud-Agrawal, E.J. Denning, T.B. Woolf, O. Beckstein, MDAnalysis: a toolkit for the analysis of molecular dynamics simulations, J Comput Chem 32(10) (2011) 2319-27.
[10] S.J. Marrink, H.J. Risselada, S. Yefimov, D.P. Tieleman, A.H. de Vries, The MARTINI force field: coarse grained model for biomolecular simulations, J Phys Chem B 111(27) (2007) 7812-24.
[11] D.H. de Jong, G. Singh, W.F. Bennett, C. Arnarez, T.A. Wassenaar, L.V. Schafer, X. Periole, D.P. Tieleman, S.J. Marrink, Improved Parameters for the Martini Coarse-Grained Protein Force Field, J Chem Theory Comput 9(1) (2013) 687-97.
[12] U. Essmann, L. Perera, M.L. Berkowitz, T. Darden, H. Lee, L.G. Pedersen, A smooth particle mesh Ewald method, J. Chem. Phys. 103(19) (1995) 8577-8593.
[13] G. Bussi, D. Donadio, M. Parrinello, Canonical sampling through velocity rescaling, J Chem Phys 126(1) (2007) 014101.
[14] H.J.C. Berendsen, J.P.M. Postma, W.F.v. Gunsteren, A. DiNola, J.R. Haak, Molecular dynamics with coupling to an external bath, J. Chem. Phys. 81(8) (1984) 3684-3690.
[15] B. Fabian, S. Thallmair, G. Hummer, Small ionic radii limit time step in Martini 3 molecular dynamics simulations, J Chem Phys 157(3) (2022) 034101.
[16] M. Ropke, D. Riepl, P. Saura, A. Di Luca, M.E. Muhlbauer, A. Jussupow, A.P. Gamiz-Hernandez, V.R.I. Kaila, Deactivation blocks proton pathways in the mitochondrial complex I, Proc Natl Acad Sci U S A 118(29) (2021).
[17] C.S. Pereira, M.H. Teixeira, D.A. Russell, J. Hirst, G.M. Arantes, Mechanism of rotenone binding to respiratory complex I depends on ligand flexibility, Sci Rep 13(1) (2023) 6738.